

On the Topology and Control of Six-Phase
Current-Source Inverter (CSI) for the
Powertrain of Heavy-Duty EVs

ON THE TOPOLOGY AND CONTROL OF SIX-PHASE CURRENT-SOURCE
INVERTER (CSI) FOR THE POWERTRAIN OF HEAVY-DUTY EVs

BY

Ahmed Salem, M.Sc.

A THESIS

SUBMITTED TO THE DEPARTMENT OF ELECTRICAL & COMPUTER ENGINEERING

AND THE SCHOOL OF GRADUATE STUDIES

OF MCMASTER UNIVERSITY

IN PARTIAL FULFILMENT OF THE REQUIREMENTS

FOR THE DEGREE OF

DOCTOR OF PHILOSOPHY

© Copyright by Ahmed Salem, May 2022

All Rights Reserved

To my beloved family.

Abstract

The electrification of transportation is increasingly of interest to governments around the world as a means of contributing to the achievement of climate change goals. Transportation is a significant source of greenhouse gas emissions, but it is also the backbone of the global economy and local mobility. Electrification is widely seen as a promising pathway to reducing greenhouse gas emissions from transportation while continuing to support economic growth.

Multiphase machines have distinctive features that draw attention in the transportation electrification domain due to their features. Recently, powertrains based on the current-source inverter (CSI) are getting more attention to be a more reliable structure for Electric Vehicles (EVs) by replacing the dc-link capacitor with a choke inductor. This thesis combines these two technologies to develop a more reliable, compact powertrain for heavy-duty electric vehicles.

First, a survey covers the recent advances in several aspects such as topology, control, and performance to evaluate the possibility and the future of exploiting them more in EV applications. The six-phase drives are extensively covered here because of their inherent structure as a dual three-phase system which eases the production process. The survey presents the different topologies used in dual three-phase drives, the modulation techniques used to operate them, the status of using multiphase drives in traction applications industrially, and the upcoming trends toward promoting this technology.

New powertrain configurations for heavy-duty electric vehicles (HDEV) are proposed based on current-source inverters (CSI) and asymmetrical six-phase electric machines. Since the six-phase CSI comprises two three-phase CSIs, multiple configurations can arise based on the connection between the two CSIs. In this context, the proposed powertrain configurations are based on parallel, cascaded, and standalone six-phase CSIs. The standalone topology is based on separating the two three-phase converters by supplying each converter with a dedicated dc-dc converter.

A new and straightforward method is proposed to extend the six-phase standalone CSI. The proposed technique employs the vector space decomposition (VSD) to mitigate the inverter current harmonics and extend the linear modulation region by about 8%. For motor drive applications, increasing the fundamental output component can reflect higher torque production capability for the same drive size, given that thermal limits are not exceeded.

Moreover, to increase the drive's reliability, space vector modulation (SVM) techniques are developed to operate the six-phase CSI while reducing the common-mode voltage (CMV) content associated with the switching of semiconductors. The SVM techniques select the switching states associated with the minimum CMV value offline to eliminate the need for measurements.

Experimental validation of the proposed algorithms is presented to operate a scaled-down six-phase PMSM fed by the proposed powertrain configuration. These proposed techniques make the CSI- based powertrain a promising solution for future HDEVs in terms of cost, performance, and reliability.

Acknowledgments

First and foremost, I would like to express my sincere gratitude to my supervisor, Dr. Mehdi Narimani, for his generous support during my whole Ph.D. career. I learned and still learning many skills from him as he mentored me through the whole journey of the program.

I would like to thank Dr. Jenifer Bauman, Dr. Berker Belgin and Dr. Ali Emadi for their guidance and comments in the supervisory committee meetings. I would also like to thank Dr. Saeed Habibi and Mr. Cam Fisher from CMHT lab, support, and accommodation for conducting experiments. Their discussions motivate me to widen my knowledge to deal with real-world challenges.

Great thanks go to my parents: Mr. Salah Salem and Mrs. Aida El Rahmany. I am eternally in their debt for their unconditional support and encouragement. I would like to extend my thanks to my brother and sister and my lovely fiancée.

Contents

- Chapter 1 1
- Introduction 1
 - 1.1. Motivation 1
 - 1.2. Research Objectives and Contributions 7
 - 1.3. Contributions and Publications 8
 - 1.4. Thesis Outlines 10
- Chapter 2 13
- Features and Modeling of Multiphase Drives 13
 - 2.1. Introduction 13
 - 2.2. Multiphase Drives (MPDs) Features 14
 - 2.2.1. Lower Power/Current Rating per Phase 14
 - 2.2.2. Fault-tolerant Operation 16

2.2.3.	Torque Density Improvement.....	20
2.2.4.	Lower Dc-link Current Ripples	22
2.3.	Modeling of Multi-phase Machines	24
2.3.1.	Double-DQ Model	24
2.3.2.	Vector Space Decomposition (VSD).....	25
2.4.	Summary	27
Chapter 3	28
Topologies and Recent Advances in Multiphase Drives for EV Applications		28
3.1.	Introduction.....	28
3.2.	Six-Phase Power Electronics Converters and Modulation Techniques	29
3.2.1.	Two-level Conventional Six-phase Inverters	30
3.2.2.	Reduced Switch-count Inverters for MPDs.....	39
3.2.3.	Dual Supply Inverters for Open-End Winding Machines	41
3.2.4.	Multilevel Inverters for MPDs.....	42
3.3.	Control Methods.....	46
3.3.1.	Harmonic currents mitigation Methods	46
3.3.2.	Field-Oriented Control (FOC)	47
3.3.3.	Model Predictive Control (MPC)	47
3.4.	Research Trends and Challenges in the Use of MPDs in Traction Applications	50

3.4.1. Topological Advances	50
3.4.2. Control Methods	54
3.4.3. The use of Wide Band Gap Devices in MPDs.....	54
3.5. Summary	55
Chapter 4	57
New Standalone Current-Source Inverter (CSI)-Based Six-Phase Powertrain.....	57
4.1. Introduction	57
4.2. Overview of Three-Phase CSI-Based Powertrains	58
4.2.1. Structure.....	58
4.2.2. Modulation.....	59
4.3. New CSI-Based Powertrain Configurations	62
4.3.1. Proposed Parallel CSI-Based Powertrain (P-CSI) (Configuration 1).....	62
4.3.2. Proposed Cascaded-CSI Based Powertrain (C-CSI) (Configuration 2)	67
4.3.3. Proposed Standalone-CSI Based Powertrain (S-CSI) (Configuration 3)	72
4.4. Case Study.....	74
4.5. Experimental Results.....	78
4.5.1. Experimental Setup.....	78
4.5.2. Experimental results	80
4.6. Summary	85

Chapter 5	86
A New Space Vector Modulation technique for Six-Phase Standalone-CSI (S-CSI) with Extended Linear Modulation Range.....	86
5.1. Introduction	86
5.2. Modeling of a Six-Phase S-CSI	88
5.2.1. Operation of a Six-Phase S-CSI	88
5.2.2. Vector Space Decomposition (VSD).....	90
5.2.3. Mapping of the Current Components	91
5.3. The Proposed Modulation Technique	93
5.3.1. Proposed VSD-based SVM technique for S-CSI	93
5.3.2. Regions of Operation	95
5.3.3. Effect of Filtering Capacitors	102
5.4. Simulation Studies.....	105
5.4.1. Simulation Model	105
5.5. Experimental Results.....	110
5.5.1. Experimental Setup.....	110
5.5.2. Experimental Results	112
5.6. Summary	117
Chapter 6	119

Proposed Modulation for Common-Mode-Voltage (CMV) Reduction of Standalone-CSI (S-CSI).....	119
6.1. Introduction	119
6.2. Analysis of CMV Associated with the S-CSI Switching States	121
6.3. Proposed SVM Schemes for Common-Mode Reduction (CMR).....	126
6.3.1. VSD-Based SVM.....	126
6.3.2. Proposed and Adopted CMR-SVM Methods	128
6.3.3. Optimum Switching Patterns	131
6.4. Evaluation of the Proposed SVM Schemes	135
6.4.1. Maximum Modulation Index	136
6.4.2. Estimated CMV RMS versus Modulation Index m and Load Power Factor.....	137
6.5. Experimental Results.....	139
6.5.1. Experimental Setup.....	139
6.5.2. Experimental Results	141
6.6. Summary	150
Chapter 7	152
Conclusions and Future Work.....	152
7.1. Summary	152
7.1.1. Powertrain configuration	152

7.1.2. Extension of DC-Link current utilization	153
7.1.3. CMV reduction	154
7.2. Future Work	155
References	157

List of Figures

Figure 1.1 SUMO ^{TM4} MD six-phase drive [11].	3
Figure 1.2 Torque-speed characteristics of different models of SUMO ^{TM4} MD series [11].	4
Figure 1.3 A 4160 V drive with PWM GCT rectifier and inverter. Courtesy of	6
Figure 1.4 Six-phase CSI-based powertrains.	7
Figure 2.1 Tesla Model S inverter components 1) Control board, 2) Aluminum shield, 3) Phase current sensor ferrite ring, 4) Gate driver board, 5) Phase busbars, 6) Heat sinks, 7) TO-247 package IGBTs, 8) IGBT clips, 9) DC-link capacitors [50].	15
Figure 2.2 Phase currents in p.u. for different multiphase drives (MPDs) [3].	16
Figure 2.3 (a) Single-neutral connection, (b) two-neutral connections.	18
Figure 2.4 Different faulty cases of asymmetrical six-phase machines.	19
Figure 2.5 Maximum postfault torque range in p.u. values under different faulty cases for symmetrical and asymmetrical six-phase machines [5].	19
Figure 2.6 Required DC-link capacitance for different MPDs [56].	23
Figure 3.1 Topologies of power electronics converters for MPDs	30

Figure 3.2 Two-level inverter-fed six-phase machine.	31
Figure 3.3 All possible switching states projected to three subplanes.....	34
Figure 3.4 Comparison between different switching patterns on the THD of the line voltage at 3150 Hz switching frequency.	37
Figure 3.5 Vector Classification technique realized by (a) two separate references (b) single reference [75].	38
Figure 3.6 Nine-Switch Inverter topology	40
Figure 3.7 Five-leg inverter topology.	40
Figure 3.8 Dual supply inverter fed open-end winding six-phase machine (topology I).	41
Figure 3.9 Dual supply inverter fed open-end winding six-phase machine based on three-phase inverters (topology III).	42
Figure 3.10 NPC-fed Six-phase machine [99].	43
Figure 3.11 Block diagram of applying MPC to six-phase drives.....	48
Figure 3.12 Highly integrated nine-phase drivetrain for EV applications (1) motor housing (2) stator (3) ferrite motor (4) bearing shield – inverter base plate (5) The inverter [125].	51
Figure 3.13 Fast on-board battery charger using six-phase drive [129].	53
Figure 3.14 Single-phase on-board battery charger using six-phase drive [130].	53
Figure 4.1 Common CSI-based three-phase powertrain structure.....	58
Figure 4.2 Possible switching states for three-phase CSI.	60
Figure 4.3 Possible switching states for dc-dc converter.....	61

Figure 4.4 New powertrain configuration based on six-phase parallel CSI (Configuration 1). ...	62
Figure 4.5 P-CSI operating in the switching state I2 {S1+S6} for CSI1 as an example to show the voltage and current stresses.	65
Figure 4.6 New powertrain configuration based on six-phase cascaded CSI (Configuration 2)..	68
Figure 4.7 Time diagram to show the key difference between the modulation of P-CSI and C-CSI.	69
Figure 4.8 C-CSI operating in the switching state I2 {S1+S6} for CSI1 and I6 {S5+S4} for CSI2 as an example to show the voltage and current stresses.	70
Figure 4.9 Phasor diagram of the summations of line voltages V_{A1B1} and V_{A2B2} , V_{B2C2} , V_{C2A2}	71
Figure 4.10 New powertrain configuration based on six-phase standalone CSI (Configuration 3).	72
Figure 4.11 The experimental setup to test the proposed scheme.	78
Figure 4.12 Experimental results of the C-CSI configuration at motor speed = 350 rpm at load torque = 31.6N.m.	82
Figure 4.13 Experimental results of the P-CSI configuration at motor speed = 350 rpm at load torque = 31.6N.m.	83
Figure 4.14 Experimental results of the S-CSI configuration at motor speed = 350 rpm at load torque = 31.6N.m.	85
Figure 5.1 The standalone six-phase CSI (S-CSI) topology for $2N$ configuration.	89
Figure 5.2 Projection of possible output states of the S-CSI structure using the VSD method....	92
Figure 5.3 The selected vectors for sector I.	94

Figure 5.4 Null time at the maximum modulation index.....	97
Figure 5.5 The flowchart of the optimization process to select the amplitudes and angles of the injected xy harmonics.....	99
Figure 5.6 The results of the optimization process with unlimited injection.....	100
Figure 5.7 Linear modulation regions.....	101
Figure 5.8 Dwell times as ratios of the sampling time over section II based on the optimized coefficients for the injected harmonics.	102
Figure 5.9 Per-phase equivalent circuit of the load and filtering stages.	103
Figure 5.10 Bode plot of the magnitude of the transfer function G	105
Figure 5.11 The angle of the transfer function G	105
Figure 5.12 Control block diagram of the motor drive simulation to test the proposed scheme.	108
Figure 5.13 The results of the IPMSM simulation model under the proposed scheme and controlled by FOC. The motor runs at reference speed $N_r = 1200$ rpm and 244 N.m. loading torque. A step load of 22 N.m. is applied to run the S-CSI in Region II of the modulation.	109
Figure 5.14 The experimental setup to test the proposed scheme.	111
Figure 5.15 Experimental results of running the setup at $m = 1$ at $\omega = 350$ rpm, $T = 31.6$ N. m.	114
Figure 5.16 Experimental results of running the setup at $m = 1.0773$ at $\omega = 350$ rpm, $T = 34.6$ N. m.	116
Figure 6.1 S-CSI configuration of asymmetrical six-phase motors.....	122

Figure 6.2 Phasor diagram showing the possible outcomes of the resultant CMV of the selected group of switching states in the example.....	124
Figure 6.3 The selected vectors for CMR-SVM 1.....	129
Figure 6.4 The selected vectors for CMR-SVM 2.....	130
Figure 6.5 The selected vectors for CMR-SVM 3.....	131
Figure 6.6 Flowchart of the optimum sequence selection algorithm.....	132
Figure 6.7 Optimum sequence for the switching states of the proposed schemes in sector I.....	135
Figure 6.8 The normalized CMV_{RMS} vs. the modulation index and the load power factor using different modulation schemes for S-CSI.....	139
Figure 6.9 The experimental setup to test the proposed scheme.	140
Figure 6.10 Motor speed and torque for the VCT and the proposed CMR-SVM schemes under the same point of operation.....	144
Figure 6.11 Motor phase currents for the VCT and the proposed CMR-SVM schemes under the same point of operation.....	145
Figure 6.12 Harmonic spectrum of the motor phase currents for the VCT and the proposed CMR-SVM schemes under the same point of operation.	146
Figure 6.13 Motor phase voltages for the VCT and the proposed CMR-SVM schemes under the same point of operation.....	147
Figure 6.14 Harmonic spectrum of the motor phase voltages for the VCT and the proposed CMR-SVM schemes under the same point of operation.	148

Figure 6.15 CMV of the VCT and the proposed CMR-SVM schemes under the same point of operation. 149

Figure 6.16 Harmonic spectrum of the CMV of the VCT and the proposed CMR-SVM schemes under the same point of operation..... 150

List of Tables

Table 1.1 DOE Targets for Electric Traction Motors [1]	2
Table 2.1 : Comparison between Different Harmonic Injection Methods to Increase Torque Density of Asymmetrical Six-Phase Machines.....	22
Table 2.2 Comparison between The Decoupling Theories of a Six-Phase System.....	26
Table 3.1 Voltage Vectors Categories.....	34
Table 3.2 Possible Switching Patterns of SVPWM Technique for Asymmetrical Six-Phase Based on VSD Theory	36
Table 3.3 Modulation Schemes of Six-Phase Two-Level Inverters	39
Table 3.4 Comparison between Different Converter Topologies for Six-Phase Drives.....	45
Table 3.5 Comparison between Different Control Methods for Six-Phase Drives	49
Table 4.1 Comparison between three-phase CSI, P-CSI, C-CSI and S-CSI	75
Table 4.2 PARAMETERS OF THE MOTOR LOAD UNDER THE SIMULATION STUDY	79
Table 5.1 CATEGORIES OF CURRENT VECTORS	92

Table 5.2 parameters of the resistive-inductive load for filter selection study	104
Table 5.3 parameters of the motor load under the simulation study	108
Table 5.4 Parameters of the motor load under the simulation study	111
Table 5.5 THD Comparison between Region I and II	117
Table 6.1 Classification of the states of S-CSI based on the resultant magnitude of CMV	125
Table 6.2 The Sequence of Switching States of The CMR-SVM 1 Scheme.....	133
Table 6.3 The Sequence of Switching States of the CMR-SVM 2 Scheme	134
Table 6.4 The Sequence of Switching States of the CMR-SVM 3 Scheme	134
Table 6.5 Summary of the calculations of the maximum modulation index associated with the proposed SVM schemes.....	137
Table 6.6 Parameters of the motor load under the simulation study	141
Table 6.7 Voltage THD evaluation of the SVM schemes	142
Table 6.8 CMV Evaluation of The SVM Schemes.....	143

Chapter 1

Introduction

1.1. Motivation

Climate change is an irrefutable fact that acquires global attention to save the future. Transportation electrification, such as electric and hybrid-electric vehicles, more-electric aircraft, and marine propulsion systems, is one of many initiatives pursued to reduce carbon emissions. Many challenges face electric vehicles in the competition with internal combustion engines, including the energy storage limit coupled with the car mileage, the cost of manufacture and retail, and rare earth metals required for electronics and motors [1]. Hence, the research and development trends focus on developing less expensive vehicles with higher efficiency, reliability, and energy density. The reliability addressed in this context is mainly the lifetime of the components since the performance degrades with aging. According to [1], The U.S Department of Energy (DOE) targets to reduce the cost of producing electric traction motors by 30% and increase the power density by 80% by the year 2025 compared to the targets of the year 2020 as in Table 1.1.

Table 1.1 DOE Targets for Electric Traction Motors [1]

Year	2020	2025
Cost (\$/kW)	4.7	3.3
Power density (kW/L)	5.7	50

One of the research trends to close the gap in achieving these targets is multiphase drives (MPDs). Multiphase systems are gaining more popularity nowadays, not only in academic circles but also in industrial applications. For example, several multiphase drives are currently manufactured for electric vehicle (EV) applications by Dana TM4 [2]. One of the main merits of multiphase drives is splitting the drive's full power into a higher number of phases compared to their three-phase counterparts [3]. This feature enables the selection of semiconductors with lower ratings without parallel devices to achieve high current ratings, as in the traction inverter of the Tesla Model S [4], which is based on the three-phase topology. The increased number of phases reflects an increased number of degrees of freedom. This feature can be utilized in the fault-tolerant operation of such drives with higher torque than the three-phase counterparts [5, 6]. Furthermore, a high torque density can be achieved by harmonic injection to either produce more torque or allow higher torque production by the fundamental flux component [7, 8].

In addition, one of the most used multiphase drives is the six-phase one because of its multiple three-phase structures [9]. The symmetrical and asymmetrical configurations are two famous arrangements of the six-phase motor windings. The symmetrical structure has an electrical

displacement angle of 60° in space between the two sets of three-phase windings. In contrast, the asymmetrical ones, also referred to as semi-twelve-phase, have an angle of 30° . The asymmetrical six-phase motors have an advantage in eliminating the fifth and seven space harmonics in the airgap magnetomotive force [10].

Recently, TM4© launched a manufacturing line of MPDs using three-, six- and nine-phase machines. Figure 1.1 shows one of the products in the line called TM4 SUMO^{TM4} MD. The product has several models with a peak power range between 162 to 265 kW and maximum torque ranges from 1600 to 3255 Nm. The product series is suited for medium to heavy-duty vehicles such as buses and delivery trucks. One electric vehicle manufacturer that uses the TM4 products is EMOSS company in their EMS truck series with a six-phase model up to 200 kW/2950 Nm. A nine-phase model up to 250kW/3400N.m. The torque-speed characteristics of different series models are shown in Figure 1.2, and the six-phase models have higher curves than the three-phase ones.

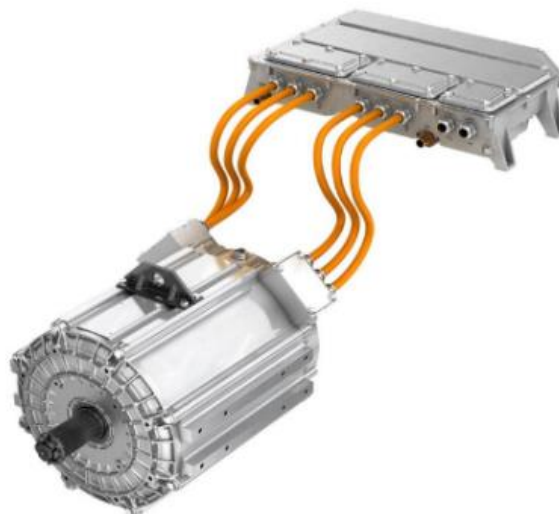


Figure 1.1 SUMO^{TM4} MD six-phase drive [11].

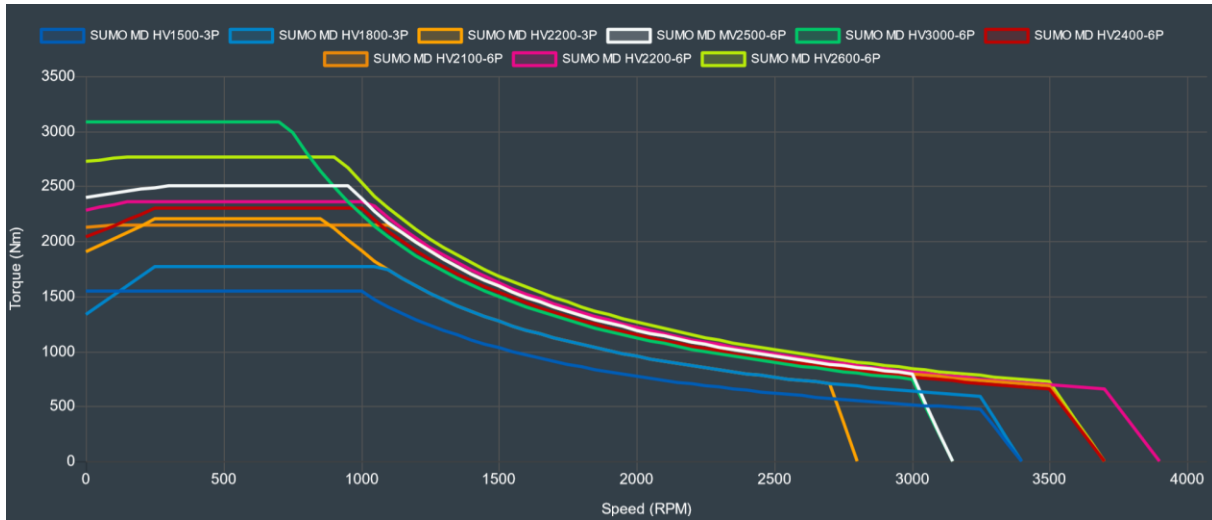


Figure 1.2 Torque-speed characteristics of different models of SUMO^{TM4} MD series [11].

TM4 also provides another series called SUMO^{TM4} HD series dedicated to heavy-duty applications. This series uses nine-phase machines with their high voltage inverter. This series of models provide high characteristics such as peak power up to 350 kW, peak torque up to 3500, and max operating speed up to 3400 RPM. This series is integrated with Dana's products for heavy-duty applications like buses and trucks.

One of the main challenges that face a new technology such as MPD is the availability of well-established three-phase drives. The cost of producing new technologies is high initially because the traditional drives are off the shelf, and differences are not high enough as a breakthrough technology to force the manufacturers to produce more MPDs. The advances in industrial power electronics and the fact that transportation applications depend on DC-AC converters make MPDs more likely to be used in the future as the difference would be inverting from dc to any number of phases as long as the drive would be more efficient on the overall performance basis.

Another example of empowering multiphase machines in the industry is studied in [12]. The proposal is to study using a nine-phase traction motor in an ultra-high-speed elevator as an alternative to traditional three-phase PMSM. The application requires a high-power motor to achieve speeds such as 1000 m/min and carry a weight of 1600 Kg, equivalent to 24 passengers to travel 540 m. The estimated power of the motor is 1 MW, and the nine-phase alternative provides the opportunity to divide this high-power demand across a higher number of phases. The experimental tests were carried out in one of the world's tallest test towers, as the paper claims, and the results show that the proposed system is reliable and can operate to achieve the required standards. Due to the superior features of MPDs in terms of power density, performance, and fault-tolerant capability, it is expected to see more manufacturers will produce MPDs for EV, ship applications, and electric aircraft applications.

On the other hand, current-source inverters (CSI) are prominent in medium to high power converters applications such as offshore wind farms [13] and general motor drives applications [14]. Although voltage source inverter (VSI) systems have off-shelf availability, a powertrain topology based on three-phase CSI has received attention recently for electric vehicle applications. The attraction towards the CSI-based powertrains is due to several merits [15, 16]. The paradigm of this shift is the lifetime enhancement prospect by replacing the limited lifetime bank of capacitors in the VSI powertrain with a choke dc-inductor in CSI powertrains [17]. Other merits of the CSI system can be summarized as short-circuit fault capability [18], elimination of dv/dt problems [19], motor friendly output waveforms [20], embedded voltage boosting capability [16].

One of the industrial medium-voltage drives is the PowerFlex 7000 AC drive, shown in Figure 1.3. The drive power ranges from 1.5 to 25.4 MW and supplies 2400 to 6600V AC voltage.

The drive controls induction machines and PMSMs by sensorless control, direct vector control, or full vector control. Marine applications, electrically submersible pumps, down-hole pump applications, conveyers, and refiners are examples of industrial use of such drive.



Figure 1.3 A 4160 V drive with PWM GCT rectifier and inverter. Courtesy of Rockwell Automation Canada [21].

CSI-based multiphase drives have been investigated lately, including the five-phase and six-phase ones. For example, space vector modulation (SVM) techniques are introduced to operate the motor with controlled harmonics as in [22] and minimized common-mode voltage (CMV) as in [17]. The six-phase drives are studied in [13] for the offshore wind farm applications and to address the mitigation of the dc-link choke ripple currents and fault-tolerant operation under open-circuit phase faults. The configuration in the five-phase case is discussed in [17, 22] as the legs are connected in parallel to the supply. Meanwhile, in the six-phase CSI case [13], the two three-phase CSIs are connected in the cascaded configuration.

The merits of multiphase systems and CSI inspire the development of a powertrain for EVs with high power demand, as shown in Figure 1.4. Heavy-duty EVs such as electric buses and trucks are good candidates for the new powertrain configuration.

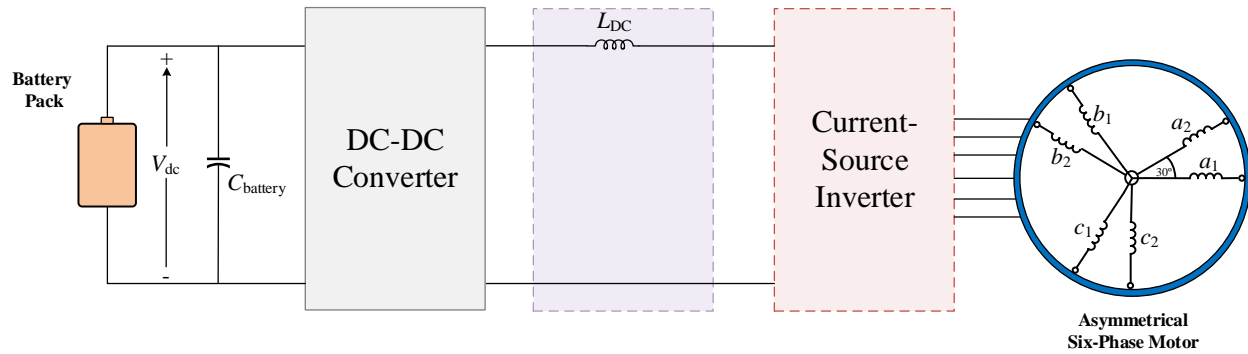


Figure 1.4 Six-phase CSI-based powertrains.

1.2. Research Objectives and Contributions

While combining both multiphase and CSI technologies is promising for heavy-duty electric vehicles, there are several emerging challenges required to be tackled:

1. In powertrains of electric vehicles based on VSIs, dc-link capacitor banks are bulky and have a limited lifetime that affects the total lifetime of the drive. CSI-based powertrains can be a prominent substitute for the VSI-based drive since a more reliable dc-choke is used as the conditioner stage between dc-dc and dc-ac conversion stages.
2. Since one of the challenges of the EV industry is to increase the power and energy densities of power converters and motor drives, the multiphase features can be utilized to increase the torque capability of the drive without increasing its mass or volume. The six-phase VSI-based drives have been tested for this feature. However, the potential of utilizing such a feature in six-phase CSI-based drives is yet to be explored in this work.

3. One of the reliability issues is common-mode voltage (CMV) resulting from the switching nature of power converters. CMV is one issue that shortens the lifetime of several parts of the drive. The six-phase CSIs have the potential to reduce the peak-to-peak and rms values of CMV.

1.3. Contributions and Publications

This thesis researches a powertrain development based on six-phase current-source fed drives. The author contributes to several original developments, which are presented in the dissertation and briefly summarized as follows:

1. Different CSI-based powertrain configurations have been proposed and developed. Since a six-phase inverter comprises two sets of three-phase inverters, three configurations: parallel, cascaded, and standalone CSI, are developed from battery to motor with case studies to compare the proposals. A selection of the best-suited configuration is also presented and built on throughout the rest of the work.
2. A new space vector modulation technique is also developed to operate the selected topology based on vector space decomposition. The extra degrees of freedom in six-phase systems prolong the dc-link current utilization with minimum harmonic injection. The method is based on optimizing the injected harmonics within the inverter constraints. This feature considers the processing speeds limit of current microcontrollers by easing the computational burden on the microcontroller. The implementation is based on look-up tables that store the values of the optimized harmonics versus the modulation index range, which simplifies the process.

3. In addition, a common-mode voltage study is conducted to relate the resulting voltage with the applied switching states of the inverter. Then, a novel offline selection method of the null-vector and active switching states is presented to reduce the resulted CMV of the inverter. Three proposed SVM schemes are developed based on the selection method. The schemes are investigated against load power factor variations and maximum dc-link current utilization.
4. An experimental setup is developed to validate the feasibility of the proposed algorithms.

During the time spent working on the thesis, I was also involved in other research projects. Below is a list of all the journal papers and conferences resulting from my work during the Ph. D.:

Journal Papers:

- [J1] A. Salem and M. Narimani, "A Review on Multiphase Drives for Automotive Traction Applications," in IEEE Transactions on Transportation Electrification, vol. 5, no. 4, pp. 1329-1348, Dec. 2019, doi: 10.1109/TTE.2019.2956355.
- [J2] A. Salem and M. Narimani, "New Powertrain Configurations Based on Six-Phase Current-Source Inverters for Heavy-Duty Electric Vehicles" submitted to IEEE Access..
- [J3] A. Salem and M. Narimani, "Modulation Range Extension of Six-Phase Cascaded-CSI Using Optimal Harmonics Injection" submitted to IEEE Open Journal of the Industrial Electronics Society.

- [J4] A. Salem and M. Narimani, "Offline-Based SVM Techniques to Reduce Common-Mode Voltage of Six-Phase Cascaded-CSI" in IEEE Open Journal of Power Electronics, 2022, doi: 10.1109/OJPEL.2022.3193058.

Conference Papers:

- [C1] A. Salem and M. Narimani, "Fault-Tolerant Operation of Asymmetrical Six-Phase Motor Drives in EV Applications," 2020 IEEE Transportation Electrification Conference & Expo (ITEC), 2020, pp. 210-215, doi: 10.1109/ITEC48692.2020.9161760.
- [C2] A. Salem and M. Narimani, "Nine-Switch Current-Source Inverter-Fed Asymmetrical Six-Phase Machines Based on Vector Space Decomposition," 2020 IEEE Energy Conversion Congress and Exposition (ECCE), 2020, pp. 1951-1956, doi: 10.1109/ECCE44975.2020.9235771.

1.4. Thesis Outlines

A brief description of each chapter is given as follows:

Chapter 1 provides the motivation and challenges regarding multiphase drives and current-source inverters and the potential of the combination in powertrains for heavy-duty EVs.

Chapter 2 reviews the multiphase drives in EV applications from features and modeling methods of multiphase machines and converters. Meanwhile, Chapter 3 revolves around the converter topologies used in this domain with their modulation techniques. The research trends and challenges in topological advances, control methods, and wideband gap devices are discussed in a dedicated section.

In Chapter 4, an overview of the three-phase CSI-based powertrains and three new powertrain configurations are proposed and studied: parallel, cascaded, and standalone configurations, including their structure, modulation, and sizing of components. Then, a comparative analysis is performed in a case study. The simulation and experimental results are shown.

Chapter 5 discusses the system model, and the inverter outputs are mapped into the equivalent subspaces using the vector space decomposition (VSD) method. The details of the proposed SVM technique are illustrated, and the optimization problem is to minimize the harmonics content while realizing the maximum linear modulation index. The effects of the filtering capacitors are also discussed in this section. Simulation studies to verify the proposed method are carried out, and the experimental results with discussions are presented.

In Chapter 6, the analysis of the standalone-CSI topology is introduced, which focuses on the topology structure and analysis of all the possible switching states, and the CMV analysis is based on the inverter states. The CMV analysis comprises a calculation method for the total CMV of the stand-alone CSI (S-CSI) and classification of the allowable states of the S-CSI based on the resultant CMV. Incorporating the CMV analysis is a step toward developing the proposed schemes. A general dwell time calculation method is developed, and each proposed SVM scheme details. Optimum switching patterns are generated to minimize the total number of transitions per sampling time. Also, a quantitative evaluation is carried out to compare the proposed methods based on the dc-link utilization and RMS value of CMV. The experimental validation is discussed, including the laboratory prototype description and the system operating results under the proposed schemes.

In Chapter 7, the contents of the thesis are summarized with the work's conclusions. The main contributions of the thesis are illustrated. The chapter also concludes by suggesting potential future research that can be done based on the thesis work.

Chapter 2

Features and Modeling of Multiphase Drives

2.1. Introduction

The first multiphase drive (MPD) was introduced in [23], discussing how the torque fluctuations in five-phase drives are lower than the traditional three-phase ones by approximately 67%. The six-phase case is investigated in [24] as another milestone in developing industrial MPDs considering a six-step modulation. The rapid development of industrial power electronics and modulation techniques of converters encouraged more research in MPDs. The features of the MPDs attracted researchers to utilize them in traction applications such as electric vehicles [25-28] and electric ship propulsion [29, 30].

Multiphase drives (MPDs) have splendid features compared with their three-phase counterparts [31-35]. One feature is splitting the power across a higher number of phases; hence the power rating per phase is lower. Another feature is the improved magneto-motive force distribution in the machine's air gap, which reflects lower torque ripples. Furthermore, the degrees

of freedom are increased based on the number of independent phase variables of the drive, which provides vital features such as fault-tolerant operation [5, 36-40] and torque density improvement using harmonic current injection [7, 41-46].

Another aspect of studying MPDs is modeling, which is one of the attractive topics to many researchers. The main theories of modeling the dual three-phase machines are the vector space decomposition (VSD) [47, 48] and the double dq model theory [49]. The different theories of decoupling the variables of the drive system are a mandatory step in developing proper modulation techniques for the MPDs.

2.2. Multiphase Drives (MPDs) Features

MPDs have unique features compared to traditional three-phase drives. This section covers the recent research contributions to highlight them:

2.2.1. Lower Power/Current Rating per Phase

The existing electric motor drive units in the commercial electric vehicles are designed such that modules or discrete IGBTs are connected in parallel, as shown in Figure 2.1, to deliver the load current. Figure 2.1 shows the assembly of the Tesla Model S inverter components. This connection results in different problems like the differences in turning on/off timing due to manufacturing differences between the paralleled transistors and different characteristics of the gate driver modules. Another major problem is the different load sharing between the paralleled transistors. Finally, the heat dissipation of all the transistors should be managed so that no transistor exceeds the allowable thermal limit. In MPDs, the power is divided across many phases, and each phase is supplied from a converter leg using a single component instead of parallel components.

Using MPDs solves the problem of paralleled devices at the expense of adding more complexity to the assembly of the drive as the number of wires increases.

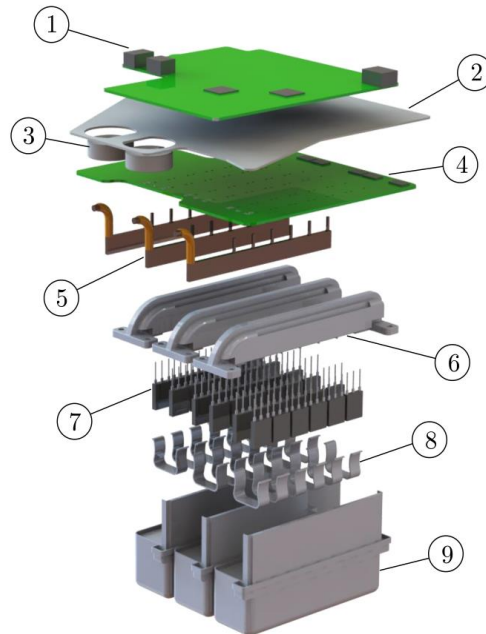


Figure 2.1 Tesla Model S inverter components 1) Control board, 2) Aluminum shield, 3) Phase current sensor ferrite ring, 4) Gate driver board, 5) Phase busbars, 6) Heat sinks, 7) TO-247 package IGBTs, 8) IGBT clips, 9) DC-link capacitors [50].

Figure 2.2 shows the reduction in phase current of several multiphase machines, namely, five-, six-, seven-, nine-, eleven- and twelve-phase machines [3]. All the phase currents are in per unit (p.u.) values, with the base value considered as the phase current of the three-phase case. The relation between the number of phases and the per-phase current is inversely proportional. The five-, six-, and seven-phase cases significantly reduce per-phase currents compared to the three-phase case. The reduction in per-phase current gets smaller as the number of phases gets higher such as going from the eleven-phase to the twelve-phase case. The phase currents for six-phase

machines are half the currents of three-phase machines which can be interpreted as choosing the same modules used for existing three-phase drives, and instead of paralleling them to control the same phase, they can be controlled separately to control different phases.

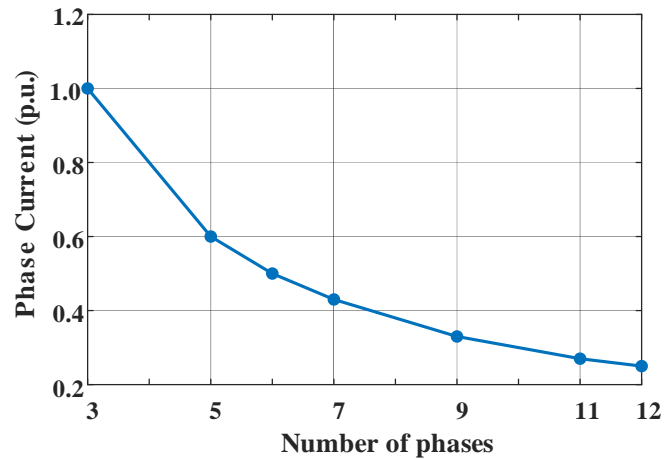


Figure 2.2 Phase currents in p.u. for different multiphase drives (MPDs) [3].

2.2.2. Fault-tolerant Operation

One of the inherent features of MPDs is the fault-tolerant operation. The increased number of phases provides more degrees of freedom in faulty conditions. In faulty cases, MPDs are better than their traditional three-phase counterparts. The drive's performance is enhanced based on the optimization criteria discussed in the literature.

The faulty conditions are the machine windings faults resulting in the loss of one or more phases considered open-circuit faults. The fault tolerance capability of the six-phase drives has attracted many researchers recently; however, it is limited to component-level only. The detection of the fault occurrence is discussed in [51]. Six-phase machines have different winding configurations depending on the space angle between the two three-phase windings. The machines with the 60° are named the symmetrical six-phase machines, whereas the asymmetrical ones are the machines with a 30° of space angle difference. The asymmetrical six-phase machine, also

referred to as the dual three-phase machine, has advantages in terms of the space harmonics of the fifth and seventh harmonic in the air gap flux of the machine compared to their symmetric counterparts [10]. The issue of operation under fault without any hardware reconfiguration for different MPDs has been investigated for the first time in [40] using current-source inverters. The criterion for optimization was only creating a rotating magnetic field with the remaining phases.

In reference [38], the problem has been investigated for a single open-circuit fault using a voltage-source inverter introducing two different optimization criteria: minimum stator winding losses and maximum torque. A unified analysis using the same strategies but with more than single-phase winding loss is discussed in [5]. An improved approach is introduced in [52] that suggests widening the optimization criterion to achieve minimum losses in the full torque operation range in the case of a single open-circuit fault. The study has been extended to be applied to double open circuit faults with different possible combinations of the faulty phases. Reference [53] investigates the converter losses in the faulty cases after applying the different optimization criteria introduced in the literature.

The asymmetrical six-phase machines have two possible connections of the stator phase windings depending on the connection of the neutral point. Figure 2.3 shows the possible configurations: two isolated neutral points and a single isolated neutral point. The single-neutral point connection proves worthy in the fault-tolerant operation. In contrast, the two isolated neutral points connection has better dc-link utilization and simpler current controllers because no zero-sequence currents can physically flow using this connection [5]. The following discussion concerns the faulty cases for asymmetrical and symmetrical six-phase machines.

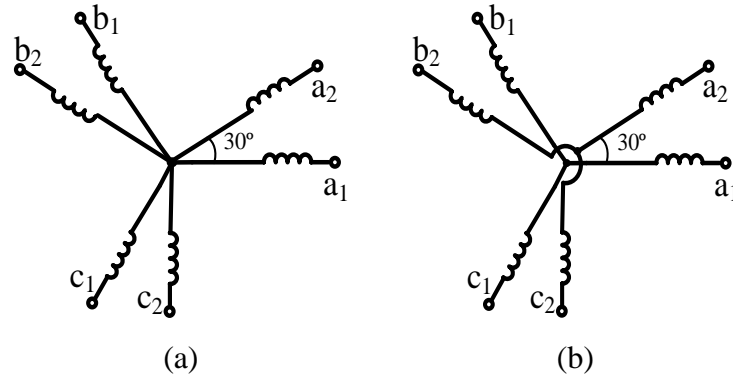


Figure 2.3 (a) Single-neutral connection, (b) two-neutral connections.

Fault-tolerant capability is one of the key features of MPDs to exploit this technology in traction industries. The different faulty cases that the asymmetrical six-phase machine with a single-neutral connection can operate under with optimal current control are mentioned in Figure 2.4. The faulty phases which are open circuited after fault occurrence are colored in red in Figure 2.4. Each case is assigned a notation nX composed of a number n represents the number of faulty phases, where $n \in \{1,2,3\}$ and a letter X represents different combinations of the possible faults, where $X \in \{A, B, C, D\}$. For example, two open-circuit faults could be either from the same set (2A) or one from each set, as in case (2B). Figure 2.4 shows all the possible non-repeated combinations of the one, two, or three faulty phases. The other possible combinations are not shown here because they have the same characteristics. Figure 2.5 shows the maximum post-fault torque range in p.u. values under faulty conditions for asymmetrical machines in (a) and symmetrical ones in (b) [5].

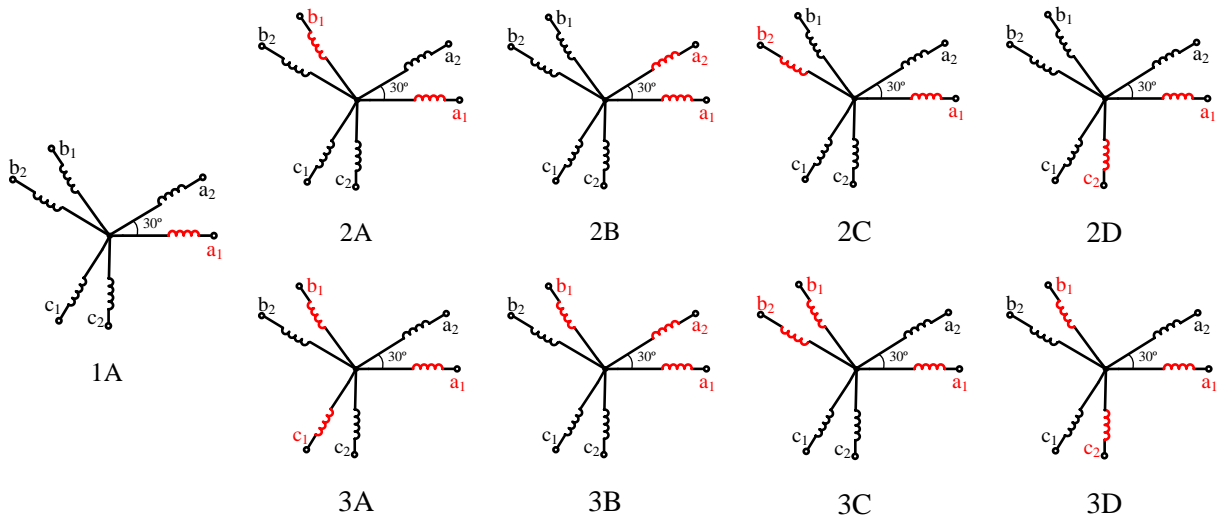


Figure 2.4 Different faulty cases of asymmetrical six-phase machines.

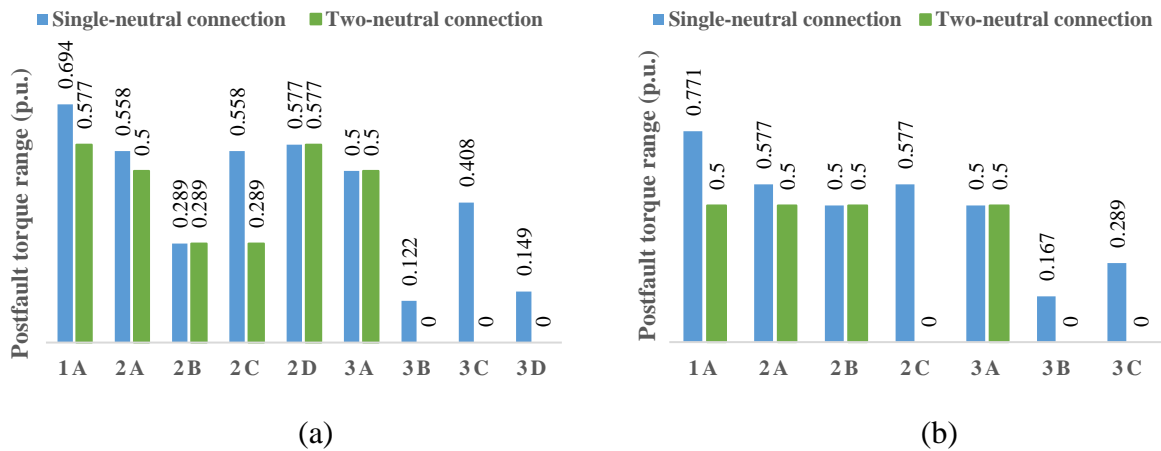


Figure 2.5 Maximum postfault torque range in p.u. values under different faulty cases for symmetrical and asymmetrical six-phase machines [5].

As shown in Figure 2.5, the connection of the neutral points of the machine winding has a significant effect on the post-fault torque range. It can be seen that the single-neutral connection results in higher torque ranges compared to the two-neutral connection. In some cases, the two-

neutral connection can not support optimal current control, such as three-phase faults for asymmetrical machines and the cases (2C, 3B, and 3C) for symmetrical ones.

It can also be noticed from the figures that the symmetrical machines are superior compared to the asymmetrical ones regarding the torque range under faulty conditions. However, the authors recommend the asymmetrical six-phase machines for EV applications for their merits in healthy case conditions, and the difference between torque ranges under faulty conditions is not high enough to choose symmetrical six-phase machines instead. However, a hybrid connection of the neutrals is introduced in [6] to achieve better torque-speed exploitation by combining the two torque-speed curves with the single and two isolated neutrals connections.

2.2.3. Torque Density Improvement

Torque density improvement is another exciting feature of MPDs that could provide a high-power density motor drive for EV applications. Decomposed subplanes can model the variables of multiphase machines, as will be discussed in detail in the next section. One of the subplanes is considered the torque-producing plane, and the others as losses. In reference [41], it is proven that with a specific winding layout, the zero-sequence subplane can contribute to the torque production of the machine. The concept is that a rotating magnetic field can be produced by injecting two 90° out of phase sets of zero-sequence currents into the two three-phase sets with a unique winding layout.

The harmonic injection method could increase the torque density of multiphase motor drives; however, two problems are associated with the third harmonic injection in six-phase drives. One problem is providing a neutral path for the currents to flow through. This problem is addressed in [41] by connecting the neutral of machine winding to the midpoint of the dc-link. Reference [44]

also addressed the problem of balancing the voltage of the midpoint to prevent it from drifting during loading using an additional proportional controller. The other problem is optimizing the flux pattern in the machine air gap. During loading of the machine, the angle of the third harmonic currents varies, leading to uneven hills of the resultant total air gap MMF. Several publications targeted this issue to analyze the problem and prevent it [54, 55]. The solutions proposed are based on artificial intelligence techniques like genetic algorithms in [54] and neural networks in [55].

Reference [42] also studies the optimal third harmonic amplitude injected into the current in a dual three-phase machine. It is dependent on the ratio of the third-harmonic back EMF to the fundamental back EMF. The optimal third harmonic into the current in the dual three-phase machine without third-harmonic back EMF is one-sixth of the fundamental harmonic. For the dual three-phase PM machines with the third-harmonic back EMF and two sets of windings shifted 30 electrical degrees, the optimal third harmonic into the current is dependent on the ratio of the third-harmonic back EMF to the fundamental back EMF.

Another proposal of current injection is investigated in [43] that focuses on injecting harmonic currents of fifth and seventh order to produce a flatter top current waveform to increase the torque per fundamental current amperes. The only problem is that these harmonic currents are considered circulating currents that do not contribute to the torque production. The injected currents' optimization and efficiency analysis have been done in [7]. These techniques can help increase the torque per fundamental current amperes, provide a sound reduction in the overall size and weight of the motor drives, and lead the way to solve one of the main challenges in the research field of electrified transportation.

Table 2.1 summarizes the possible methods to increase the torque density of asymmetrical six-phase machines via harmonic injection. The tooth and core flux density constraints limit the

increase of the produced torque in induction motors as in [41], which considers machines with a concentrated winding. The PMSMs are investigated in [7, 42, 43] with a possibility to increase the torque density beyond the values in Table 2.1. The interaction between the injected harmonic currents and the same components of back EMF results in additional torque production. This feature can be enabled in PMSM by changing the stator winding layout, resulting in the desired harmonic components of back EMF. However, the additional torque improvement comes at the cost of an inevitable increase in torque ripples.

Table 2.1 : Comparison between Different Harmonic Injection Methods to Increase Torque Density of Asymmetrical Six-Phase Machines

Machine Type	Harmonic order to be injected	Constraints	Minimum average torque enhancement	Possible further improvement
Induction	3rd harmonic [41]	Peak flux density allowing teeth saturation	40%	-
	3rd harmonic [41]	Both tooth and core flux density are within rated values	21%	
PMSM	3rd harmonic [42]	Both tooth and core flux density are within rated values	15%	It depends on the winding layout and the components of the Back EMF
	5th + 7th harmonics [7, 43]	Both tooth and core flux density are within rated values	7.7%	

2.2.4. Lower Dc-link Current Ripples

The dc-link bank of capacitors is one of the essential components in the electric vehicle's powertrain and the power electronic converter. The capacitor bank size is about two-thirds of the overall converter size. One of the reliability concerns in EVs is the dc-link capacitor bank because of drastic performance degradation while aging. The study [56] focuses on the different types of capacitors deployed in EV applications. The study also includes the required dc-link capacitance

for different MPDs using the coulomb counting technique to estimate the count of charges based on capacitor currents which can be calculated from the switching function of the inverter. Figure 2.6 shows a comparison between the required capacitance in p.u. for different MPDs considering the base value of the dc-link capacitance as the one required for the three-phase case. This figure shows that the required capacitance decreases with the increased number of phases of the system up to the twelve-phase one [52].

There is a high decrease in the dc-link capacitance compared between three-phase and five-phase cases. The curve decreases considering the cases of six-, seven- and nine-phase drives. However, the capacitance required for the cases nine-, eleven- and twelve-phase machines appears to be the same. As shown in Figure 2.6, the dc-link capacitor values are almost reduced to half when a six-phase drive is considered, which could help the converter become more power-dense than a conventional three-phase system.

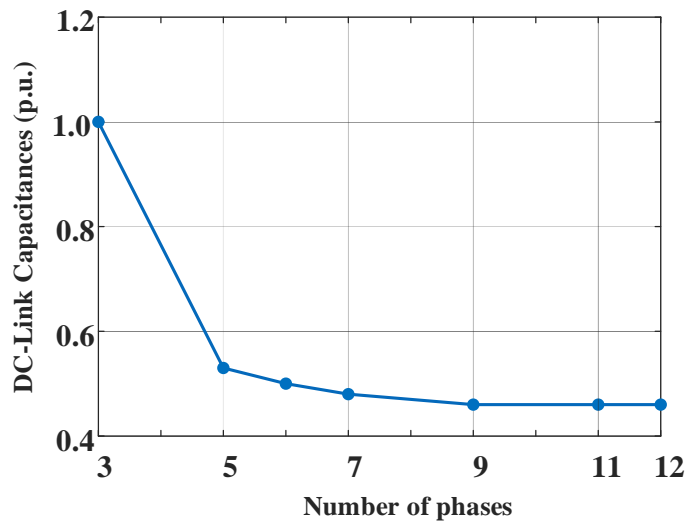


Figure 2.6 Required DC-link capacitance for different MPDs [56].

2.3. Modeling of Multi-phase Machines

Modeling multiphase machines is required to provide a high-performance modulation and control technique for MPDs. In this section, different modeling techniques, especially for six-phase machines, are reviewed. Six-phase machines have different winding configurations depending on the space angle between the two three-phase windings. The machines with the 60° are named the symmetrical six-phase machines, whereas the asymmetrical ones are the machines with 30° of space angle difference. The asymmetrical six-phase machine also referred to in the literature as the dual three-phase machine, has advantages in terms of the space harmonics of the fifth and seventh harmonic in the airgap flux of the machine compared to their symmetric counterparts [10].

2.3.1. Double-DQ Model

Based on the double-DQ model, the two three-phase windings in a six-phase machine are treated separately, and two three-phase different (Clarke) transformations are applied to the phase variables for each three-phase winding [49]. The α -axis of the stationary reference frame is aligned with phase- a_1 of the stator winding. The transformation decomposes the six-phase variables into two sets of stationary reference frame variables, denoted as $\alpha_1 - \beta_1$ and $\alpha_2 - \beta_2$ components, for windings sets abc_1 and abc_2 , respectively:

$$[f_{\alpha_j} \ f_{\beta_j}]^t = [T_j] \cdot [f_{a_j} \ f_{b_j} \ f_{c_j}]^t \quad (2.1)$$

where f is a general symbol for all the machine variables (voltage, current, or flux) and k is the subscript of values 1 or 2 to differentiate between the variables of the two three-phase windings.

The decoupling transformation accounts for the spatial 30° displacement between the two windings. For an asymmetrical six-phase machine, the invariant power transformation for windings sets abc_1 and abc_2 , respectively, is given by:

$$\begin{aligned}
 [T_1] &= \sqrt{\frac{2}{3}} \begin{bmatrix} 1 & -\frac{1}{2} & -\frac{1}{2} \\ 0 & \frac{\sqrt{3}}{2} & -\frac{\sqrt{3}}{2} \end{bmatrix} \\
 [T_2] &= \sqrt{\frac{2}{3}} \begin{bmatrix} \frac{\sqrt{3}}{2} & -\frac{\sqrt{3}}{2} & 0 \\ -1 & \frac{1}{2} & \frac{1}{2} \end{bmatrix}
 \end{aligned} \tag{2.2}$$

2.3.2. Vector Space Decomposition (VSD)

VSD has been widely used to model multiphase AC machines [57-59]. The primary purpose is to decompose the machine voltages and currents from the original six-dimensional space into new independent subspaces. This transformation fully represents the machine dynamics and helps design a controller with the same structure in healthy and faulty cases.

Based on the decomposition theory, all the machine variables in the original six-dimensional space are transformed into three time-orthogonal subspaces. The harmonics of the original vectors are mapped into three groups named $\alpha\beta$, xy , 0_+0_- Subspaces. The first group represents the fundamental harmonic components and the harmonics of order $k = 12h \pm 1$ as ($h = 1, 2, 3, \dots$). The $\alpha\beta$ currents are the torque-producing components since they represent the fundamental harmonic.

The other four vectors should be based on their orthogonality on the aforementioned $\alpha\beta$ subspace [47]. It is found that the harmonics of $k = 6h \pm 1$ as ($h = 1, 3, 5, \dots$) spin in the same surface and their subspace is denoted by the xy subplane. The xy current components do not contribute to the torque production process; hence they are considered as extra losses in healthy case conditions and as extra degrees of freedom in faulty cases. The last group is the triplen

harmonics group that is defined by $k = 3h$ as ($h = 1, 2, 3, \dots$) and mapped to the 0_+0_- subspace. The current components of the 0_+0_- subspace do not exist unless there is a physical path for neutral currents. Equation (2.3) shows the VSD transformation matrix for asymmetrical six-phase machines.

$$[T] = \frac{1}{\sqrt{3}} \begin{bmatrix} 1 & -\frac{1}{2} & -\frac{1}{2} & \frac{\sqrt{3}}{2} & -\frac{\sqrt{3}}{2} & 0 \\ 0 & \frac{\sqrt{3}}{2} & -\frac{\sqrt{3}}{2} & \frac{1}{2} & \frac{1}{2} & -1 \\ 1 & -\frac{1}{2} & -\frac{1}{2} & -\frac{\sqrt{3}}{2} & \frac{\sqrt{3}}{2} & 0 \\ 0 & -\frac{\sqrt{3}}{2} & \frac{\sqrt{3}}{2} & \frac{1}{2} & \frac{1}{2} & -1 \\ 1 & 1 & 1 & 0 & 0 & 0 \\ 0 & 0 & 0 & 1 & 1 & 1 \end{bmatrix} \quad (2.3)$$

By applying a transformation matrix, the variables are transformed into ($\alpha\beta xy0^+0^-$) reference frame [47]. A summary comparison between double-DQ and VSD methods is shown in Table 2.2.

Table 2.2 Comparison between The Decoupling Theories of a Six-Phase System

Modeling Method	Double-DQ	VSD
Approach	The machine is considered as a double three-phase machine.	The six-phase machine is considered as one system.
Capturing the power-sharing of each three-phase set	Yes	No
Featuring the asymmetries between the two sets	No	Yes
Complexity and implementation	Simple concept and easy to implement.	More complex.

2.4. Summary

This chapter presented a survey of the features and modeling of multiphase drives. The focus is the six-phase drives since they are the most applicable to the EV applications for the thesis's subject. The features mentioned in this chapter include the power splitting across a higher number of phases. Comparing existing technologies and multiphase ones supports the better utilization of converter components, cable connections, and motor features in multiphase systems. The fault-tolerant operation feature is also discussed, showing that six-phase drives have an extended torque production capability under faulty conditions with optimized copper losses.

Moreover, the torque density improvement via harmonic currents injection are summarized in terms of which harmonics to be injected and the different methods employed in induction motors and PMSMs. The last feature discussed is reducing dc-link ripples, hence, lower dc-link capacitance requirements in multiphase systems. The six-phase case is highlighted as the breaking point in the domain of increasing the number of drive phases versus the capacitance requirement.

The modeling methods of multiphase machines are covered in the survey to build upon in the next chapter to understand modulation and control strategies better. The two leading theories are the double- dq model and the vector space decomposition (VSD). A comparison is presented to show the advantages and weaknesses of both methods. The VSD method is adopted in all the thesis's contributions since it has a better overall system representation.

Chapter 3

Topologies and Recent Advances in Multiphase Drives for EV Applications

3.1. Introduction

MPDs comprise power conversion stages that are implemented using power electronics converters. One of the power conversion processes is AC-DC-AC in industrial applications fed from the traditional three-phase mains using the pulse-width modulation-based converters. The literature presents the AC-AC conversions as one solution using the matrix converters. Another power conversion, DC-AC conversion, is applicable in EV applications where the electrical power source is the batteries. This chapter covers the recent advances from the topological point of view of the converters used in MPDs for EV applications.

One of the classical control techniques used to obtain the optimal performance of MPDs is field-oriented control (FOC). Recently, model-based control schemes such as model predictive control (MPC) were introduced as a simple control scheme. All these schemes and their features are discussed in the control section providing a trade-off in the conclusion section. A dedicated section in this chapter is provided to present an overview of the FOC and MPC techniques used with MPDs. Furthermore, the current status and examples of industrial manufacturing of MPDs for EV applications are revised. Lastly, the last section encounters the trends and challenges in research to improve and incorporate the MPDs in the EV industry.

3.2. Six-Phase Power Electronics Converters and Modulation Techniques

Electrical drives have been supplied and controlled recently using a power electronic converter, enabling the drive to operate in all possible regions and reach the desired speed and torque. Figure 3.1 demonstrates the different topologies used for MPDs that can be exploited in industrial motor applications. The topologies mentioned in this context are the DC-AC converters since the energy storage is mostly battery packs in traction applications. The topologies are classified into three categories based on the structure and number of levels of their respective output voltage.

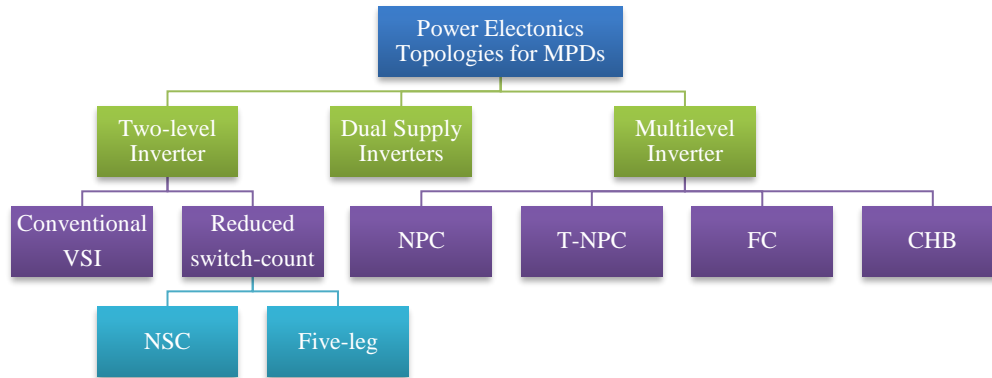


Figure 3.1 Topologies of power electronics converters for MPDs

The (2L-VSI) topologies are discussed in the first subsection, including the modulation techniques. Since the conventional (2L-VSI) topology is the one used in industry, the chapter focuses more on the modulation techniques and possible switching patterns. The possibility of reducing the number of switches is also covered in the same subsection featuring the nine-switch converter (NSC) and five-leg six-phase inverter. Another subsection is dedicated to the dual supply inverters used for open-end winding configuration, which produce more than two-level output voltages based on the same basic (2L-VSI) topology supplying each machining phase from both ends. The final subsection discusses the efforts in the multilevel inverter topologies, which are promising to be used in the traction application since it is expected that future cars will have higher dc-link voltage levels (800V) [60].

3.2.1. Two-level Conventional Six-phase Inverters

The two-level six-phase is the most investigated topology in all the literature on dual three-phase drives due to its simple structure, availability of industrial packs provided by manufacturers as two three-phase bridges, and the simple controllers needed to drive such converter compared to

other complex topologies like matrix, multilevel and open-end converters. The structure of the topology is shown in Figure 3.2.

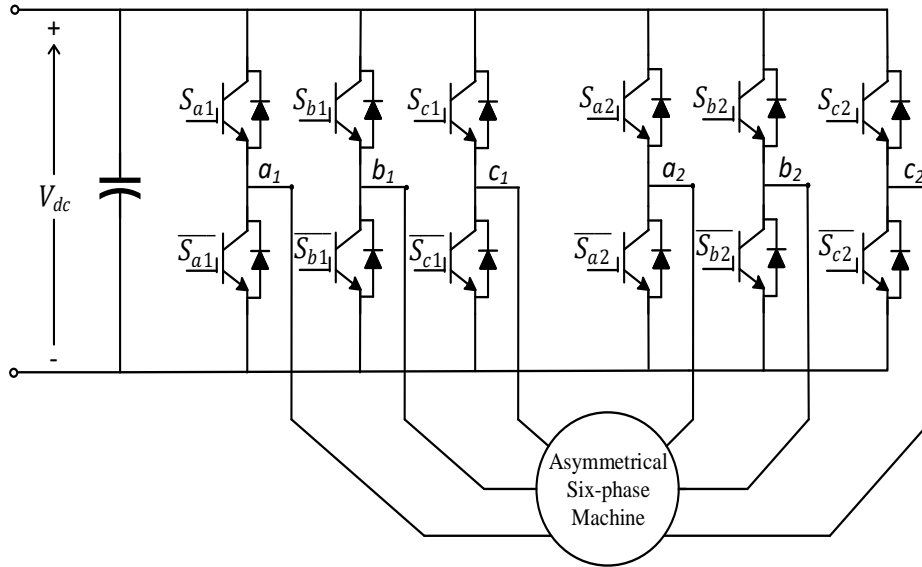


Figure 3.2 Two-level inverter-fed six-phase machine.

A. Carrier-based PWM (CPWM)

Like the traditional two-level three-phase inverter, the most popular carrier-based modulation technique of PWM (CPWM) can be exploited to operate the six-inverter. The CPWM technique is implemented using the reference signals generated from the control scheme and represents two sets of three-phase outputs shifted by 30° . The reference waveforms are compared to a carrier signal, and the output signals are used to fire the switches of the converter. The operation of the converter is investigated in [61] and for the high-frequency machines in [62]. CPWM is the most straightforward modulation technique to operate the multiphase converter. This simplicity and reliability are the significant advantages that make this technique suitable for EV applications. One of the disadvantages of CPWM is the lack of control degrees to achieve better performance of the converter, such as lowering the total harmonic distortion (THD) of the output

waveforms. Another disadvantage is the lower dc-link utilization compared to space vector techniques that can be compensated with the zero-sequence injection discussed in the next section.

B. Double Zero-Sequence Injection (DZSI)

The concept is based on the infamous zero-sequence harmonic injection technique exploited with three-phase inverters to lower the THD of the output and extend the linear control region of the inverter. It can be implemented by adding the zero-sequence component of each three-phase set to their respective reference voltages. Several publications have investigated the method, such as developing the technique in [88], which shows that it is like the vector classification technique, only simpler to implement since it is carrier-based. The improvement of the harmonics' profile is analyzed in [63], and a general comparison between the techniques was discussed in [64, 65]. A method of designing a proportional-resonant integrator to control the drive and using the injection technique has been introduced in [66].

C. Space-Vector PWM (SVPWM) based on VSD Theory

Several SVPWM techniques have been presented in the literature to minimize the circulating currents, which are considered only to contribute to the ohmic losses of the drive. The first SVPWM based on the theory of VSD theory was introduced in [47], which presented the decoupling of the machine variables discussed in the previous section. Using such transformation enables the control of the six-phase converter as a single unit. There are 64 different possible switching states referred to in this work by ($V_0: V_{63}$). The switching states are sorted in the same way introduced in the literature to avoid ambiguity. The states are numbered from 0 to 63 in a binary manner by considering each upper switch is a digit in a binary number by this order ($S_{c2}, S_{b2}, S_{a2}, S_{c1}, S_{b1}, S_{a1}$) which makes the 1st switching state is (000000) and the 64th is (111111).





The output phase voltage can be calculated based on the switching states from (3.1) for the two isolated neutrals connection and from (3.2) for the single isolated one.

$$\begin{bmatrix} V_{a1} \\ V_{b1} \\ V_{c1} \\ V_{a2} \\ V_{b2} \\ V_{c2} \end{bmatrix} = \frac{V_{dc}}{3} \begin{bmatrix} 2 & -1 & -1 & 0 & 0 & 0 \\ -1 & 2 & -1 & 0 & 0 & 0 \\ -1 & -1 & 2 & 0 & 0 & 0 \\ 0 & 0 & 0 & 2 & -1 & -1 \\ 0 & 0 & 0 & -1 & 2 & -1 \\ 0 & 0 & 0 & -1 & -1 & 2 \end{bmatrix} \begin{bmatrix} S_{a1} \\ S_{b1} \\ S_{c1} \\ S_{a2} \\ S_{b2} \\ S_{c2} \end{bmatrix} \quad (3.1)$$

$$\begin{bmatrix} V_{a1} \\ V_{b1} \\ V_{c1} \\ V_{a2} \\ V_{b2} \\ V_{c2} \end{bmatrix} = \frac{V_{dc}}{6} \begin{bmatrix} 5 & -1 & -1 & -1 & -1 & -1 \\ -1 & 5 & -1 & -1 & -1 & -1 \\ -1 & -1 & 5 & -1 & -1 & -1 \\ -1 & -1 & -1 & 5 & -1 & -1 \\ -1 & -1 & -1 & -1 & 5 & -1 \\ -1 & -1 & -1 & -1 & -1 & 5 \end{bmatrix} \begin{bmatrix} S_{a1} \\ S_{b1} \\ S_{c1} \\ S_{a2} \\ S_{b2} \\ S_{c2} \end{bmatrix} \quad (3.2)$$

Applying the transformation matrix (3) to the resulted output voltages to transfer them to the decoupled subplanes ($V_\alpha - V_\beta$), ($V_x - V_y$) and ($V_{0+} - V_{0-}$). Figure 3.3 shows the projection of all the possible switching states in the three orthogonal subplanes. Regarding the 0_+ , 0_- components, all the vectors are mapped to the origin point in the case of the two isolated neutrals; however, in the single isolated neutral point connection, the vectors are mapped as presented in Figure 3.3(c). The vectors in the $\alpha\beta$ subplane are classified into four categories based on their magnitude. Table 3.1 shows the four categories' respective colors plotted in Figure 3.3.

Table 3.1 Voltage Vectors Categories

Magnitude	Colour
$V_1 = 1.115V_{dc}$	
$V_2 = 0.816V_{dc}$	
$V_3 = 0.577V_{dc}$	
$V_4 = 0.299V_{dc}$	

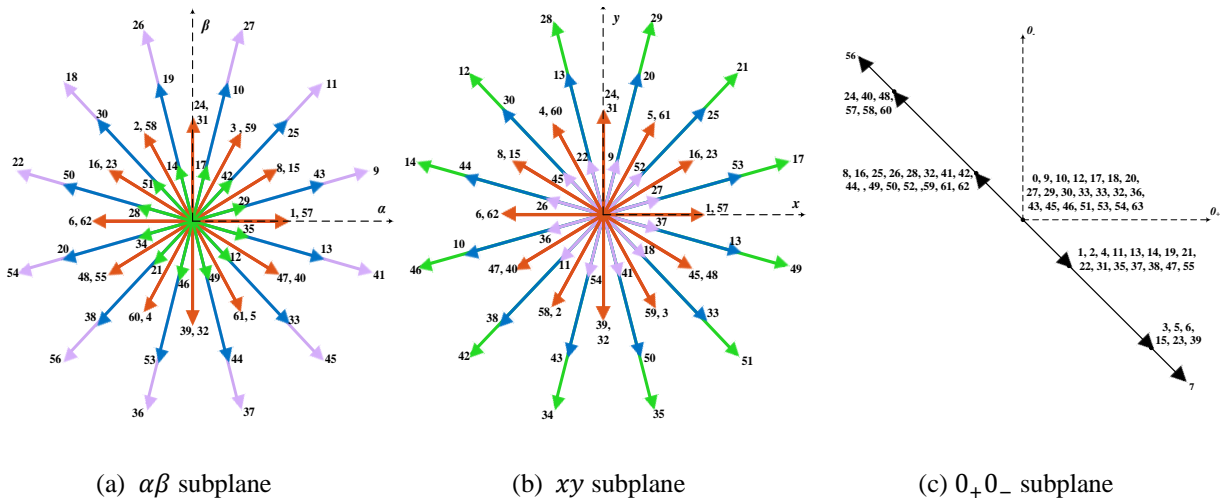


Figure 3.3 All possible switching states projected to three subplanes.

The SVPWM is exploited by realizing the rotating reference determined by the controller. The reference components are inserted into (3.3) to calculate the dwell times of the possible applied vectors.

$$\begin{bmatrix} T_1 \\ T_2 \\ T_3 \\ T_4 \\ T_0 \end{bmatrix} = \begin{bmatrix} V_\alpha^1 & V_\alpha^2 & V_\alpha^3 & V_\alpha^4 & V_\alpha^5 \\ V_\beta^1 & V_\beta^2 & V_\beta^3 & V_\beta^4 & V_\beta^5 \\ V_x^1 & V_x^2 & V_x^3 & V_x^4 & V_x^5 \\ V_y^1 & V_y^2 & V_y^3 & V_y^4 & V_y^5 \\ 1 & 1 & 1 & 1 & 1 \end{bmatrix}^{-1} \begin{bmatrix} V_\alpha^* \cdot T_s \\ V_\beta^* \cdot T_s \\ V_x^* \cdot T_s \\ V_y^* \cdot T_s \\ T_s \end{bmatrix} \quad (3.3)$$

where V_γ^k the superscript $k \in \{1,2,3,4,5\}$ is the sequence of the applied voltage vector and subscript $\gamma \in \{\alpha, \beta, x, y\}$ denotes the axis to which the voltage vector is synthesized.

Since there are four degrees of freedom in the two separated neutrals connection, four system equations are adopted to calculate the dwell times. For the single-neutral connection, it is proven in the literature that the zero-sequence voltage components are nullified without any further calculations based on the nature of the voltage vectors mapped to this subplane, as shown in Figure 3.3(c). However, choosing the vectors that cancel the components of xy subplane is more challenging. References stated several switching patterns based on the number of sectors of the modulation technique. The two distinctive strategies are 12-sector SVPWM and the 24-sector SVPWM [63]-[65]. In each sector, four different vectors with magnitude V_1 are chosen to synthesize the reference output by volt second concept (6). The chosen vectors have a magnitude of V_1 in the $\alpha\beta$ subplane. On the other hand, the 24-sector SVPWM is implemented by choosing three vectors of magnitude V_1 and one vector of magnitude V_3 . The method of inserting the zero-vectors determines the continuous and discontinuous modulation scheme [67-70]. As stated in the literature 24-sector SVPWM method is easier to implement using DSP microcontrollers and results in less THD in the output waveforms of the converter.

Table 3.2 compares the reported switching patterns based on the 12- and 24-sector switching patterns for continuous and discontinuous modulations. The name of each switching pattern starts

with the letter C for continuous modulation and D for discontinuous one. The patterns that start and end with a zero-vector are denoted with the letter A, whereas notation B1 and B2 to the patterns that only start or end with the zero-vector, respectively. The 24-sector patterns have the advantages of fewer transitions per one period of sampling time and more straightforward implementation since each switch is turned on or off one time per period compared to the 12-sector patterns with more than one transition per period.

Table 3.2 Possible Switching Patterns of SVPWM Technique for Asymmetrical Six-Phase Based on VSD Theory

Method	Patterns	Number of transitions (rising/falling) per period	$\frac{f_{sw}}{f_{swbase}}^{(*)}$	DSP implementation complexity
12-sector	C_A	12	1	Complex
	D_A	8	$\frac{2}{3}$	
	D_B1	6	$\frac{1}{2}$	
	D_B2	6	$\frac{1}{2}$	
24-sector	C	6	1	Simple
	D_B1	5	$\frac{5}{6}$	
	D_B2	4	$\frac{2}{3}$	

(*) f_{sw} is the average switching frequency and f_{swbase} is the baseline switching frequency, which is the C_A pattern for the 12-sector switching patterns and the C pattern for the 24-sector ones.

Implementing the 12-sector patterns on the DSP microcontroller is challenging since each switch might have more than one transition per period. However, implementing the 24-sector ones is simpler because there is a maximum of one transition per period. Figure 3.4 shows the THD of the output line voltage of a six-phase inverter using the different switching patterns at the same switching frequency at different modulation indexes. The differences are not very high. However,

the 24-sector continuous modulation switching pattern shows the lowest profile of THD. Based on the comparisons, the patterns based on 24-sector modulation prove the best options for modulating six-phase inverters in traction applications. The switching losses will be lower, resulting in lower cooling requirements and higher efficiency operation to achieve extended-range vehicles.

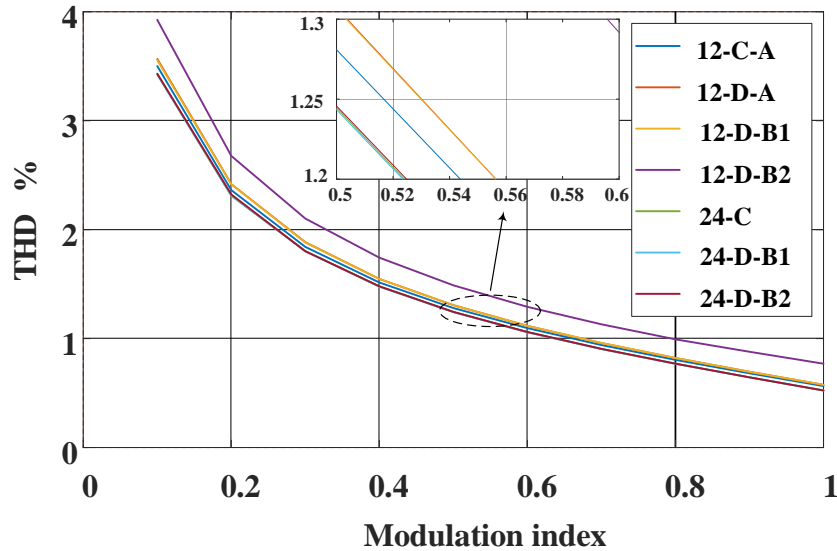


Figure 3.4 Comparison between different switching patterns on the THD of the line voltage at 3150 Hz switching frequency.

D. Vector Classification Technique (VCT)

This technique is mainly based on the double- DQ theory of modeling the six-phase system. VCT was proposed in [71] and followed by further enhancements in choosing the vectors [72] using a modified neural network and getting better utilization of the dc-link voltage, such as in [73]. Two different approaches have approached the realization of this technique, as in Figure 3.5. The first way is implemented by using two references rotating in the familiar hexagon representing all the possible switching vectors of the three-phase inverter, as shown in Figure 3.5(a). The second way is by rotating one of the hexagons by 30° and using a single reference, such as in Figure 3.5(b).

A study proposed in [74] compares the classification technique and the 12-sector switching patterns. The study shows that the classification technique is simpler to implement and gives higher utilization of the dc-link voltage, but the SVPWM techniques based on VSD theory achieve better harmonic minimization.

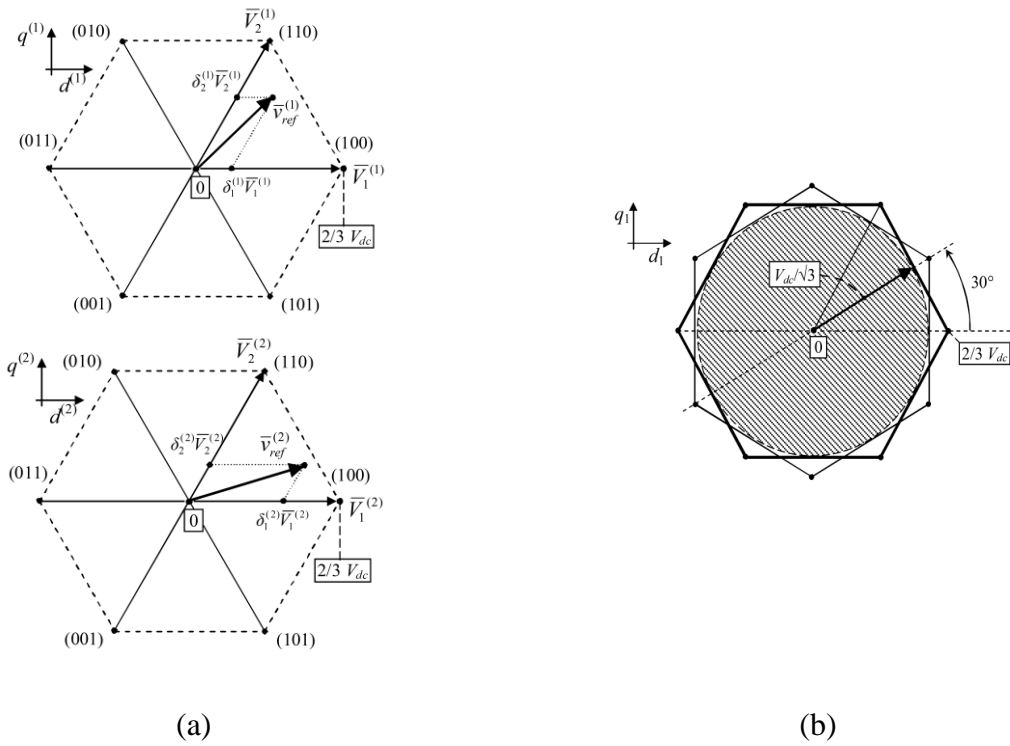


Figure 3.5 Vector Classification technique realized by (a) two separate references (b) single reference [75].

A comparison between the modulation techniques of six-phase inverters is shown in Table 3.3. The carrier-based modulation techniques are simple to implement and can get to high modulation indexes in the linear modulation region by injecting zero-sequence harmonics to the references. However, the SVPWM methods are superior in terms of enhancing the quality of the

output waveform using the redundant switching states. The SVPWM based on the VSD method is more complex to implement but using the switching patterns mentioned in the previous subsections can significantly reduce the xy currents.

Table 3.3 Modulation Schemes of Six-Phase Two-Level Inverters

	CBPWM		SVPWM	
	SPWM	DZSI	VSD	VCT
Max. modulation index	1	1.154	1.154	1.154
Redundant switching states	No	No	Yes	Yes
Quality of output waveform	Low	Medium	High	High
Reduction of xy currents	No	No	Yes	No
Complexity and implementation	Simple	Simple	Complex	Medium

3.2.2. Reduced Switch-count Inverters for MPDs

Increasing the power density of power electronics converters is one of the trends in EV applications [76]. One of the solutions to reduce the size of the converter is using reduced switch-count topologies. Nine-Switch Inverter (NSI) is one of the topologies that has been investigated in the literature as a six-phase inverter for multiphase machines [26, 77, 78]. Figure 3.6 shows the configuration of the inverter. The modulation techniques are discussed in [79-86], which shows that the maximum modulation index for supplying an asymmetrical six-phase machine is around 81% as one of the disadvantages of this converter topology.

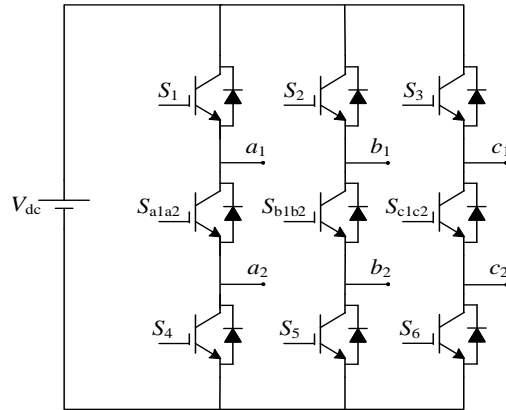


Figure 3.6 Nine-Switch Inverter topology

The switching frequency of the middle switches is double the switching of the other switches, i.e., the switching losses are the same as the conventional twelve-switch topology. Several control techniques can be used with the topology [77, 87-89]. The Z-source NSI topology is comprised of Hybrid Electric Vehicle (HEV) applications [90, 91].

Five-leg inverter is another topology with a smaller number of switches introduced as an alternative to the conventional inverter for six-phase drives [92], shown in Figure 3.7. The topology is based on connecting one machine phase to the midpoint of the dc-link as a reference to the other phases. The main challenge of using such a topology is balancing the midpoint voltage [93].

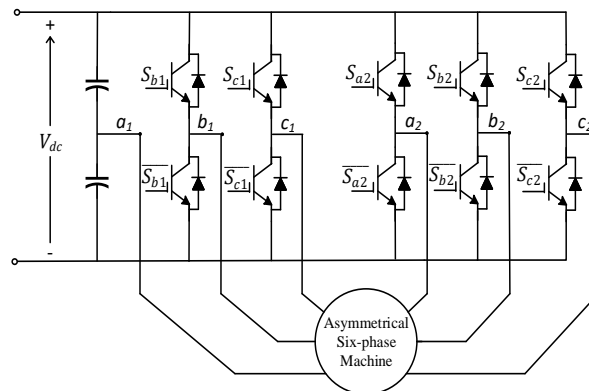


Figure 3.7 Five-leg inverter topology.

3.2.3. Dual Supply Inverters for Open-End Winding Machines

A dual supply inverter topology is a converter topology used to supply machines with an open-end winding configuration. This topology is supplied from isolated dc sources, so it does not require a capacitor voltage balancing technique, unlike most multilevel inverter topologies. The cascaded H-Bridge multilevel topology is also supplied from isolated dc sources typically provided by custom-designed phase-shifting transformers. In EV applications, the dc source is typically a pack of batteries that can be rearranged and configured to supply such topologies. Lower dc-link voltages are one of the merits of using such a converter with an increased number of components.

Several topologies were introduced in the literature based on the supplies used and how to connect them. One of them is the topology with two-sided supplies to supply two six-phase inverters, and each phase winding is connected to a converter output from both phase terminals, and it will be referred to in this work dual-supply topology I as in Figure 3.8. Another topology uses only one supply (dual supply topology II) to supply the two inverters in a five-phase drive to eliminate common-mode voltage employing SVPWM [94].

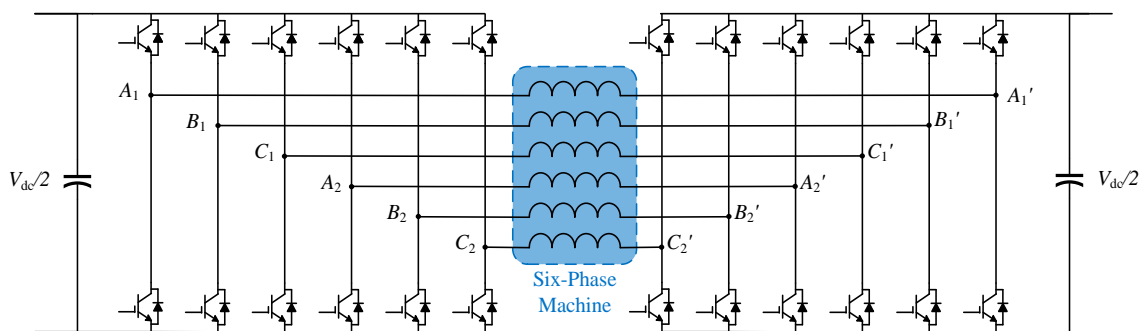


Figure 3.8 Dual supply inverter fed open-end winding six-phase machine (topology I).

Reference [95] discusses a different topology with four three-phase inverters and two supplies connected from both sides with a capacitor commonly shared by the middle inverters (dual supply topology III), as shown in Figure 3.9.

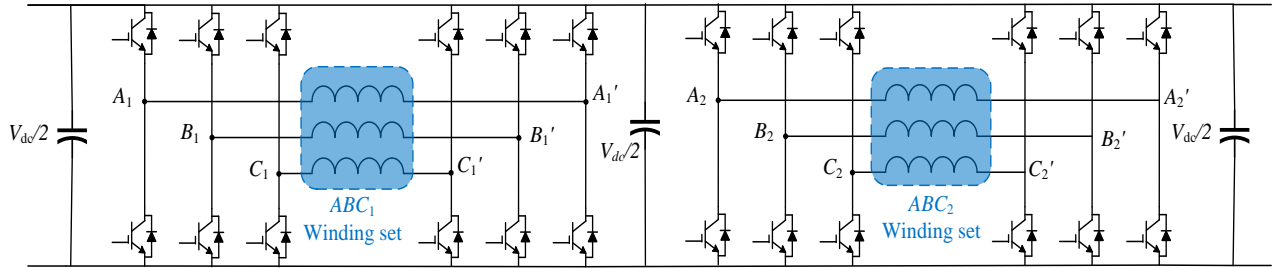


Figure 3.9 Dual supply inverter fed open-end winding six-phase machine based on three-phase inverters (topology III).

This topology is used to suppress the fifth and seventh harmonics from the output voltage to add one more capacitor bank. The assessment of the converter performance is discussed in [96-98]. Reference [96] analyzes the current ripples and proposes methods to minimize them to achieve better drive performance. The converter can generate a three-level output better than the conventional two-level one in terms of the resulting ripples in the output currents.

A comparison between the performance of symmetrical and asymmetrical six-phase drives with open-end configuration is discussed in [98] using different modulation techniques. The comparison shows that the symmetrical six-phase drives have the same results as the three- and five-phase drives, while the asymmetrical behave differently according to the different techniques applied.

3.2.4. Multilevel Inverters for MPDs

Multilevel inverters are a famous solution for high-voltage, high-power motor drives. Several topologies are discussed in the literature with pros and cons based on cost, size,

performance, and complexity. The complexity of multiphase multilevel drives increases due to the increased number of switches and switching states. However, since there is a push to increase the dc-link voltage ($>800\text{V}$) in the next generation of EVs [60], multilevel topologies will be a good candidate to improve the output power quality while improving the overall efficiency with the low voltage power semiconductors.

One well-known multilevel topology is the neutral-point clamped inverter (NPC). The research is focused up until this work on the three-level NPC inverter to supply multiphase machines due to the system's complexity. Figure 3.10 shows a three-level NPC-fed six-phase machine.

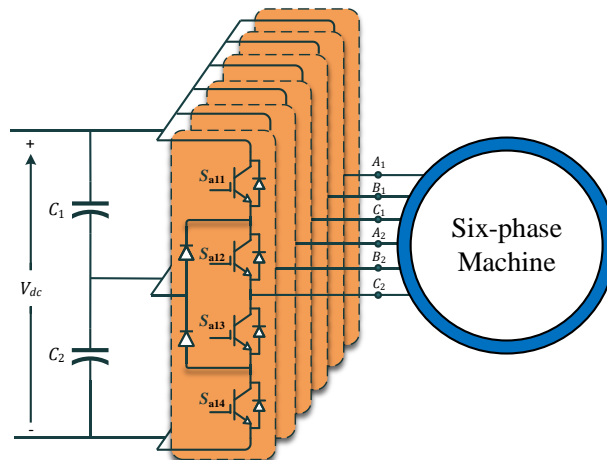


Figure 3.10 NPC-fed Six-phase machine [99].

Like the two-level topology, the SVPWM techniques used for multilevel multiphase drives are classification-based and VSD-based. The vector classification technique alongside the drive's modeling is investigated in [100]. VSD-based models are also discussed in [58, 101]. The latter publication adds a decoupling especially to develop a switching pattern based on VSD. The number of switching states to supply a dual three-phase machine is 729 with 665 distinctive voltage

vectors. It is quite the task to choose the optimum switching vector to ensure balancing the midpoint of the dc-link and minimal output circulating currents. Reference [101] demonstrates a switching pattern to operate the converter taking into account the elimination of the x-y voltage components. An improved approach is introduced in [58] that proposes a decoupled modulation technique to address the harmonic components from the back EMF generated because of unbalanced parameters of the machine and to eliminate the zero-sequence components. The improved technique has a significant drawback in the complexity and higher switching frequency.

A T-NPC topology for MPDs has also been discussed in the literature, and the modulation technique of the topology is investigated in [102], exploiting the voltage classification technique. The Direct Torque Control (DTC) control method is applied in [103] to control the drive based on the double SVPWM. A topology based on CHB structure to supply an asymmetrical six-phase machine is discussed in [104] as a medium-voltage drive. As an extension to dual-supply inverters topology, replacing the two-level three-phase topology with the three-level three-phase NPC is discussed in [105]. [106] proposes a hybrid inverter to supply one three-phase set from a conventional inverter and the other from an NPC inverter. Some advanced multilevel topologies based on FC, CHB, and active neutral-point clamped inverter (ANPC) to provide a high number of output levels up to 49 are introduced in [107-109]. Almost all the multilevel topologies for MPDs have been developed for medium-voltage industrial motor drives, and to the best of the author's knowledge, no such multilevel topologies have been used for EV applications so far. A summary comparison between the previously mentioned converter topologies is illustrated in Table 3.4.

Table 3.4 Comparison between Different Converter Topologies for Six-Phase Drives

	2-Level			NPC	Dual-Supply
	Conventional	NSC	5-Leg		
Number of switches	12	9	10	24	24
Number of clamping diodes	-	-	-	12	-
Number of DC sources and capacitor banks	Single source	Single source	Single source + two capacitor banks	Single source + two capacitor banks	Topology I: Two source Topology II: Single sources Topology III: Two Sources + extra capacitor bank
Access to the dc-link midpoint requirement	No	No	Required	Required	No
Voltage balancing requirements	No	No	Required	Required	Topology I: No Topology II: No Topology III: Required
Voltage stress on each switch	V_{dc}	V_{dc}	V_{dc}	$V_{dc}/2$	$V_{dc}/2$
Number of wires	6	6	6	6	12
Reliability	Medium	Low	Low	Low-Medium	High
Complexity	Simple	Moderate	Moderate	Complex	Complex
Power density	Baseline	Higher	Higher	Lower	Lower
Technology status for EV applications	Well established and already manufactured (e.g., TM4 [11])		Research only		

3.3. Control Methods

The control techniques used to obtain the optimal performance of MPDs are the current control method, classical field-oriented control (FOC), and the recent model-based schemes such that model predictive control (MPC). All these schemes and their applications are discussed in this section:

3.3.1. Harmonic currents mitigation Methods

As discussed earlier, the currents in the xy subspace produce losses and have no contribution to the torque production process. These currents are produced because of the voltage harmonics resulting from the modulation technique or deadtime. The resulting current harmonics have a measurable amplitude even if the voltage harmonics are minimal due to the small equivalent impedance of the x - y subspace. The solutions proposed in the literature are using controllers to nullify these currents by applying a reference of zero-value, and the mission of the controllers is to track the reference. The application of PI controllers in the synchronous frame for several multiphase induction machines was investigated in [110].

The case of asymmetrical six-phase induction motors was addressed in [49] by applying dual PI controllers in the synchronous and anti-synchronous frames was proposed to mitigate the unwanted harmonics in the x - y subspace and applying resonant controllers to compensate for the inserted deadtime. The application of resonant controllers in the x - y subspace for the same machine was addressed in [111]. Applying multi-resonant control in the synchronous frames has been proposed in [112] to compensate for current harmonics in symmetrical multiphase machines. The asymmetrical six-phase PMSMs were investigated in [113] to compensate for harmonics using a disturbance observer based on the double dq machine model. The compensation is based on the

multi-resonant controllers and the VSD machine model [114]. The efficiency of many MPDs, including inverter losses for light load operating conditions, has been studied in [115]. The complexity and increased number of controllers lead to a stability issue for industrial applications such as EVs.

3.3.2. Field-Oriented Control (FOC)

FOC is one of the famous vector control schemes used in electric drives to achieve desired torque-speed characteristics with good transient performance. The primary key to applying FOC is applying the rotor angle to decompose the current components into the torque and flux controlling components. The rotor flux angle is estimated in the induction machine using observers and estimators to account for the slip between the rotor and flux speeds. For PMSM, there is no slip calculation, and the measured rotor angle can be applied directly to find the dq axes' current components and control them to the desired characteristics. The difference between applying FOC in three-phase drives and six-phase drives is that multiphase machines have extra subspaces representing losses as the x - y subspace. The control scheme should have current controllers to eliminate these currents. Sensorless control of five-phase machines is also discussed in [116], and a comparison between using PI controllers and fuzzy logic controllers is investigated in [117].

3.3.3. Model Predictive Control (MPC)

MPC control method was introduced in [118] to control power converters, generally providing a fast dynamic response. Applying such a method to control asymmetrical six-phase drives is discussed in [119]. The concept is that the switching pattern for each sampling period is determined based on optimizing a cost function that uses the model of the drive system in the discrete-time domain, shown in Figure 3.11.

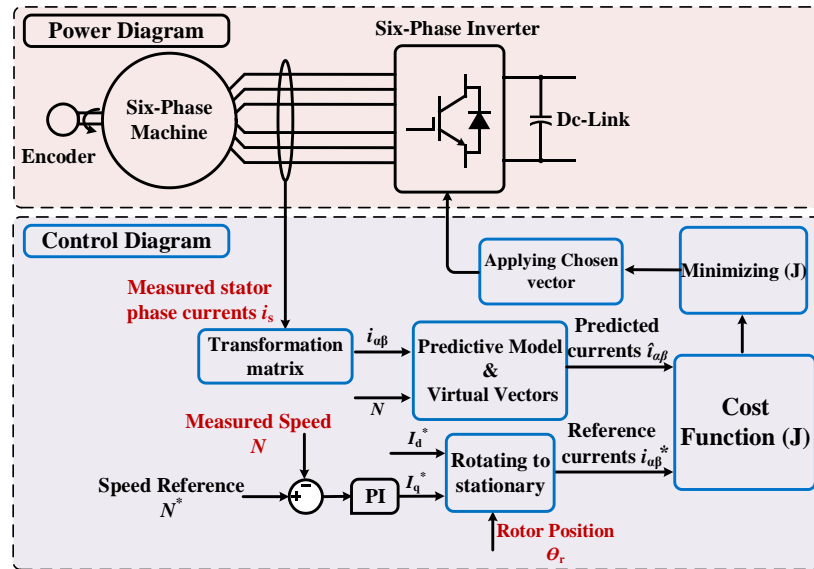


Figure 3.11 Block diagram of applying MPC to six-phase drives

All possible switching patterns are applied to the cost function to determine which one is the best candidate to be applied. The cost function can be used to satisfy the requirements of the drive, such that meeting a certain THD of the output waveform, eliminating circulating currents of the x-y subplane, providing fault-tolerance control [120-122], control of machine torque, and even mixing some criteria in one cost function but with different weights according to their priority level.

An exciting addition to the control method is that instead of applying one voltage vector in each sampling period, one can apply two of them with different weights to achieve the desired output in the fundamental plane and a zero-average voltage in the x-y plane well. This method is called the MPC, using virtual voltage vectors that have been introduced in [123]. The only disadvantage to applying this method compared to the former finite-control set method is the decreased utilization of the dc-link voltage by 7.2%. The main problems regarding applying MPC are the need to precisely determine the parameters of the drive and the increased time of the sampling period due to the large number of computations needed. A simplified MPC method is

developed in [124] to reduce the computational time in the microprocessor to make the method more feasible and practical. Table 3.5 compares FOC and MPC methods to control a six-phase drive.

Table 3.5 Comparison between Different Control Methods for Six-Phase Drives

	FOC	MPC
Use of PI or PR controllers	Speed controllers: yes Current controllers: yes	Speed controllers: yes Current controllers: No
Elimination of xy subspace currents	Yes, Using extra controllers for xy currents	Yes, Using the VV method
Transient response	slow	Fast
Modulation technique	CBPWM or SVPWM	Switching signals are generated from the controller directly
Implementation and complexity	Complex	Simple
Sensitivity to systems parameters	sensitive	Very sensitive
Stability study	Required	No

FOC method has been used for decades in industrial motor drives. However, the MPC method is promising compared to FOC since it is simple to implement, the modulation scheme is already included in the control method, no need to tune the parameters of the controllers, and the transient response is fast compared to FOC. The MPC method trends in the control area and its challenges are covered in section VI.

3.4. Research Trends and Challenges in the Use of MPDs in Traction

Applications

3.4.1. Topological Advances

3.4.1.1. New topologies

The established inverter topologies for MPDs require an additional number of switches compared to the conventional three-phase inverters to control the inverter properly and provide the given features discussed in this paper. This will be more complex and expensive where the dc-link voltage is higher than 800V, and multilevel topologies will be very attractive to improve the torque and THD performance while using the low voltage power semiconductor devices. Multilevel topologies with reduced switch count are an exciting area of research to employ MPDs in the next generation of high-voltage dc-link EVs and take the benefits of high torque density and fault-tolerant operation.

3.4.1.2. EVs with a highly integrated modular drivetrain

Integrating an inverter with the machine inside the drivetrain is to minimize the connections from the inverter to the machine phases to overcome the disadvantage of the increased number of phases and thus the connecting wires.

An asymmetrical nine-phase machine with a 20° phase shift between the three groups of three-phase windings with a highly integrated nine-phase drivetrain is shown in Figure 3.12. The drivetrain developed in [125] is a 60 kW with a 35 kW/L power density of the electronics part as a powerful solution to sizing the drive inside the vehicle. The maximum drive speed is 11500 rpm with a peak torque of 170 Nm. The benefits reported in [125] are the easy integration of the drive,

saving space in a limited environment such as EVs, and lower currents; since the drive is a nine-phase one, the converter can be designed using lower class modules have lower prices and lower size.

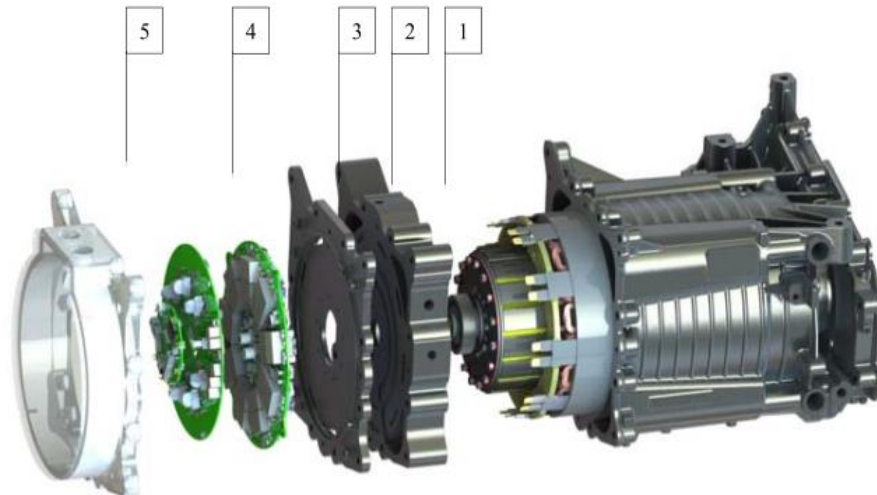


Figure 3.12 Highly integrated nine-phase drivetrain for EV applications (1) motor housing (2) stator (3) ferrite motor (4) bearing shield - inverter base plate (5) The inverter [125].

The challenges to such a topology can be in the ventilation, thermal management, and cooling from a mechanical point of view. From an electrical point of view, the high Electromagnetic Interference (EMI) and its associated problems must be studied thoroughly since the inverter and its driving circuits are very close to the motor in this design.

Using the interleaving strategy in [126] could reduce the dc-link current ripples and the size of the dc-link capacitors. A case study presented in [126] considers a fifteen-phase integrated modular drive, and the reduction in the capacitor sizing is up to half of its original size. In [127], a general solution to the design of dc-link capacitors of integrated modular drives is introduced based on a multi-criteria, multi-degrees of freedom optimization problem.

3.4.1.3. Integrated On-Board Battery Chargers

An emerging research topic in EV applications is using the onboard motor and power electronics converters as chargers to the batteries of the vehicle to avoid the installation of additional converters in the off-board chargers and use just the terminals provided by the grid. The options are to connect a single phase for slow charging to the vehicle or the three phases for fast charging. The challenge is only to use the available gear to accomplish the charging process and, at the same time, prevent the machine from revolving. The movement can be stopped by either mechanical locks or special connections in the electrical power circuit. Mechanical locks are an issue because of the size, weight, and extra electrical losses in the machine windings. However, the goal is to generate a pulsating field in fast charging mode to achieve the charging without any movement.

For asymmetrical six-phase drives, fast charging is implemented in two configurations. One of the configurations was introduced in [128], which uses a transformer with two secondary sets to provide a six-phase supply and a phase transposition. The drawbacks of the configuration are that the custom-made transformer is costly and adds to the overall size.

A study in [129] discusses the other configuration in which the three-phase grid terminals are connected to the six-phase inverter as each grid phase is connected to two phases of the inverter. Figure 3.13 shows the connection and current flow in the different phases. It is essential to mention that the connections of the phase windings are altered by employing contactors to change from propulsion mode (two separate neutrals connection) to charging mode (special connection to the three-phase grid). For single-phase grid connection, the problem of rotation disappears because the field in the machine is pulsating because the two neutral points are connected to grid terminals,

as shown in Figure 3.14. The charging current is the zero-sequence component [130] and nullifies the other subplanes to stop revolving while minimizing the losses.

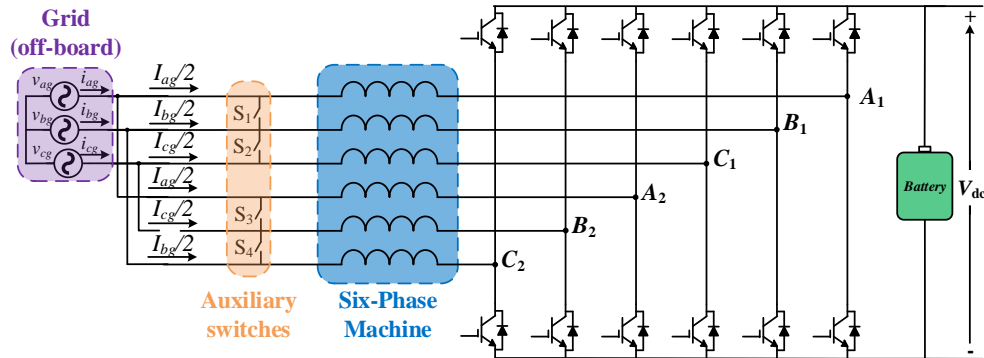


Figure 3.13 Fast on-board battery charger using six-phase drive [129].

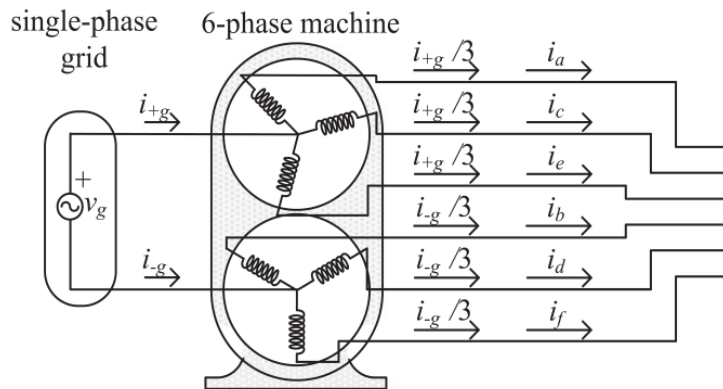


Figure 3.14 Single-phase on-board battery charger using six-phase drive [130].

The control of former topologies depends on the mode of operation. The control technique is well established in propulsion mode, and no modification is required. The charging mode aims to control the currents in the machine windings to charge the battery and produce a zero-average torque. For fast charging, the connection of the phases to the grid terminals ensures the production of a pulsating field, so the system is equivalent to a three-phase rectifier connected to a grid. A voltage-oriented control is adopted with a minor modification of adding extra controllers in the anti-synchronous frame to eliminate the asymmetries in the phase currents resulting from different

equivalent impedances of the machine. The vehicle to grid mode is the same as the charging mode with the opposite power flow direction.

Although the integrated onboard battery charger idea has been developed for a six-phase drive, there are still some challenges that require more attention by researchers, such as lowering the THD of the grid currents to meet the standards, substituting the auxiliary contactors to change the connection of the windings, and integrating the PWM rectifier and the dc-dc converter.

3.4.2. Control Methods

The model-based control techniques such as MPC methods have shown better performance at the expense of the complexity and many computations. These issues worsen when the number of phases increases. The challenge facing the development of these control techniques for MPDs is the feasibility of implementing these controllers in the current DSP microcontrollers matching the speed and memory limits. Therefore, further reduction in computation while keeping the best performance of MPDs in EVs is a big challenge.

These advanced control techniques need to be developed to reduce the dc-link ripple currents and thus reduce the dc-link capacitor values, which further improves power density.

3.4.3. The use of Wide Band Gap Devices in MPDs

The technology of Wide Bandgap devices is the next generation in the power electronics industry that will enable the manufacturing of high-power electric drives with fast switching frequencies. Silicon Carbide (SiC) and Gallium Nitride (GaN) are the most used materials for WBG devices. The WBG modules are better than conventional Silicon (Si) modules in losses, weight breakdown voltage, switching frequency, and higher junction temperatures [131]. A case study is investigated in [132] to design a 1200-V, 100-A VSC with SiC-based modules. The study

compares SiC modules and Si modules at different operating switching frequencies in terms of the estimated losses. The comparison shows the prevalence of SiC modules at all frequencies and shows that the SiC can operate even at 50 kHz, which Si modules cannot. In [133-135], the focus is on the application of WBG devices in EV applications. The dv/dt issue is addressed in [136], and a proposed solution is included using a multistage drive circuit.

The lower losses associated with using WBG devices increase the switching frequency to obtain better output waveforms, especially in low-inductance drive applications. The challenge of high dv/dt arises with the application of WBG devices accompanied by high switching frequency at high voltages. Another challenge faces by the spread of industrial manufacturing of WBG devices is the cost. The cost is expected to decline if the manufacturing technologies advance and the market demands change.

3.5. Summary

This chapter surveys the multiphase inverter topologies, emphasizing the ones that are used or good candidates in EV applications. The topologies covered are the two-level six-phase inverters, reduced switch-count inverters, dual supply inverters, and multilevel topologies. Furthermore, the most employed control schemes in multiphase drives are discussed separately. One of the covered control issues is the mitigation of harmonic currents in the xy subspace that result from the motor-converter asymmetries. The control strategies for multiphase motors such as FOC and MPC are also covered in dedicated subsections. The chapter extends the study to cover the recent research trends and challenges of employing multiphase technology in EVs. The covered trends are the topological advances such as multilevel topologies for high voltage dc-link drives ($V_{dc} \geq 800$). The MPC method is continuously enhanced, and research attention is focused on

developing more robust, faster, and simpler techniques in multiphase drives. The status of the use of WBG devices is mentioned, and the challenges that need to be addressed to avoid the problems associated with them while benefiting from their better thermal performance.

Chapter 4

New Standalone Current-Source Inverter (CSI)-Based Six-Phase Powertrain

4.1. Introduction

Since both multiphase drives and CSI are suitable for medium power applications, the asymmetrical six-phase drives fed from a CSI focus on developing the powertrain of HDEV in this context. Three configurations are developed and proposed in this chapter to struct the powertrain. The idea behind the powertrain variations is based on the different possibilities of connecting the two three-phase CSIs and the dc-dc converter to be adequately sized to perform optimally. The proposed configurations connect the two three-phase CSIs in parallel or cascade with one dc-dc converter to provide a steady, controlled current. The authors also propose a different configuration called the standalone configuration. The standalone arrangement is based on separating the two three-phase CSIs so that each one of them is supplied from a different dc-dc converter. To the

authors' best knowledge, the different configurations (parallel, cascaded, and standalone) CSI have not been appropriately studied for the EV applications yet. This chapter has studied the selection of the most appropriate configuration that comprises both conversion stages (dc-dc converter and six-phase CSI). The objectives and research contributions are summarized in the following points:

- A Proposal for studying three different configurations of six-phase CSI-based powertrains is made in dedicated subsections, including all the stages of the powertrain from the battery to the motor.
- A detailed case study with comparison is presented and followed by a discussion about which configuration is the most suitable for the application of HDEV.

4.2. Overview of Three-Phase CSI-Based Powertrains

4.2.1. Structure

This subsection is dedicated to studying the three-phase CSI-based powertrains, starting with their structure, as shown in Figure 4.1.

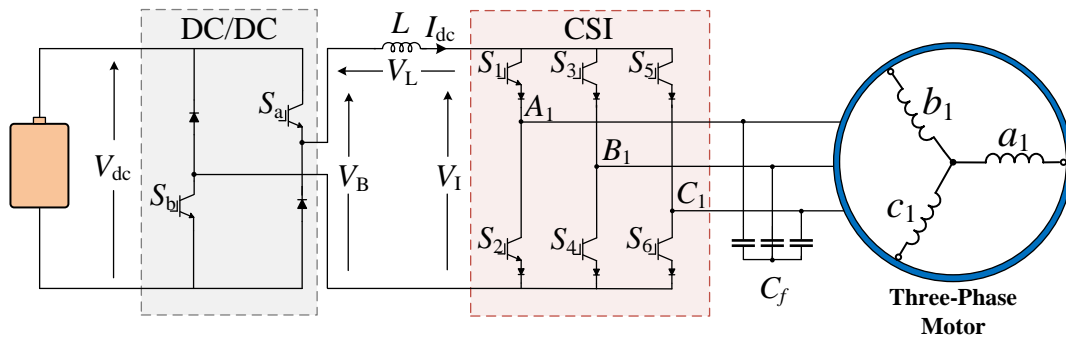


Figure 4.1 Common CSI-based three-phase powertrain structure.

The three-phase CSI consists of six unidirectional power semiconductors are called switches in this context. Every two switches are connected in series to form a converter leg. The switches can be reverse blocking IGBTs, IGCTs, or even IGBTs with one forward series diode to block reverse voltages and conduct in one direction only. A filtering stage consisting of ac capacitors is entailed in such topology for proper operation.

In CSI-based powertrains, the constant dc voltage supplied by the battery pack is converted to a controllable dc current via a dc-dc converter coupled with a choke inductor. Several previous works [4, 19] reported that the simplest topology is a bidirectional chopper converter topology. The converter consists of two half bridges that combine only one switch and one diode in each leg. The dc-dc converter connects the battery terminals to the output terminals in either positive or negative polarity or even disconnects the battery. The goal is to either charge, discharge, or freewheel the dc-link current depending on the dc-link controller's effort to regulate the current. The switching states and the required design of the battery voltage level should be considered to achieve the required dc-link current levels flowing in the dc-choke. Afterward, the power is delivered to the motor by dc/ac converter, the CSI with the filtering capacitors at the output.

4.2.2. Modulation

The modulation of three-phase CSI is covered as a step before extending it into the details of the six-phase topologies.

4.2.2.1. Three-phase CSI

SVM modulation of three-phase CSI has been established previously, as in [137, 138]. The main rules that must be fulfilled while operating CSIs are listed here as:

- The output currents of the inverter must be defined regardless of the nature of the connection of the load.
- The dc-link current cannot be interrupted due to switching actions.

Based on these rules, only two semiconductor switches out of the total number of switches connected to the same dc-bus can be turned on per switching cycle. Hence, the allowable switching states are nine (6 active + 3 null). As shown in Figure 4.2, a three-phase CSI is implemented by six switches (S1 to S6). The mapping of the output currents produced by the possible nine combinations using the famous Park transformation from the original three-phase frame to an equivalent two-axis frame is shown in Figure 4.2 [137]. The calculations of the dwelling times can be done using [138].

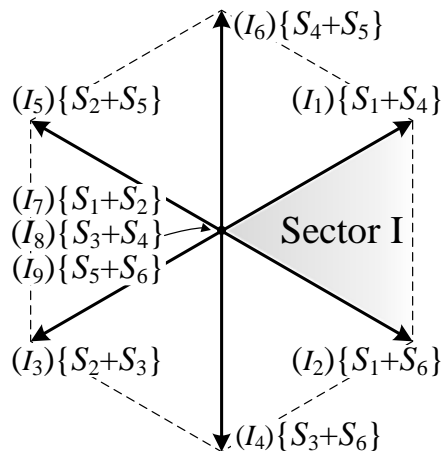


Figure 4.2 Possible switching states for three-phase CSI.

4.2.2.2. Dc-Dc converter Operation

Based on the structure of the dc-dc converter, four switching states can be applied. The four states are shown in Figure 4.3, with the path of the current colored in red. The first possible state

is achieved by turning on S_a , and S_b switches simultaneously, as shown in Figure 4.3 (a). In this state, the chopper voltage V_B that appears at the terminals of the converter equals the battery voltage V_{dc} . This mode is often called the motoring mode. The power flows from the supply to the inverter side in this mode. Another state can be activated by turning off both switches, forcing the two diodes to conduct and returning the dc-link current back to the battery, as shown in Figure 4.3 (b), which is called the regenerative mode. The power flows from the inverter side to the battery to cause a charging action in this mode. Figure 4.3 (c), (d) represents a freewheeling state. The battery is disconnected in this mode, and the dc-link current freewheels on the side of the inverter. The chopper converter output voltage is described in (4.1) as a function of the switching states of the two switches, S_a , and S_b .

$$V_B = (S_a + S_b - 1)V_{dc} \tag{4.1}$$

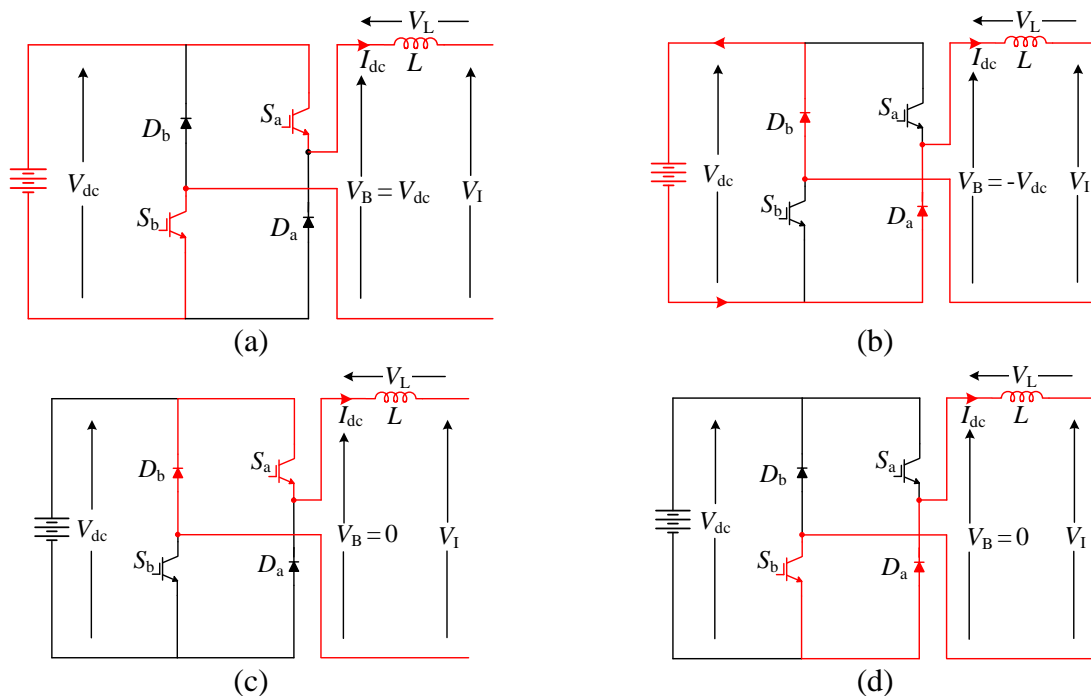


Figure 4.3 Possible switching states for dc-dc converter.

4.3. New CSI-Based Powertrain Configurations

The three new proposed configurations are introduced in this section. The structure, modulation, stresses, and sizing of the semiconductors are aspects of the study of each configuration. The considerations regarding the dc-link inductor and simplified selection criteria are developed in the subsection of stresses and sizing Parallel-CSI configuration and then followed to deduce the stresses for the other configurations in their dedicated sections.

4.3.1. Proposed Parallel CSI-Based Powertrain (P-CSI) (Configuration 1)

4.3.1.1. Structure

The two-three phase inverters CSI_1 and CSI_2 are connected in parallel in this configuration, as shown in Figure 4.4.

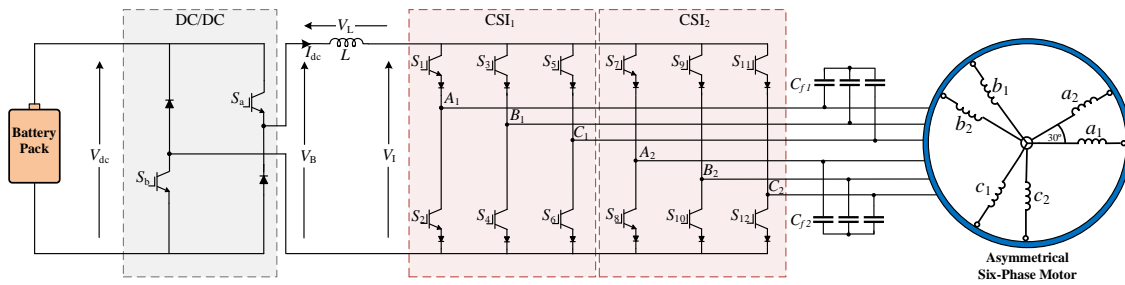


Figure 4.4 New powertrain configuration based on six-phase parallel CSI (Configuration 1).

The six legs of the inverter are all connected to the same dc-link terminals in this topology, which means that one dc-dc converter is needed to provide the dc current source. In this topology, the six phases of the motor can be connected in two arrangements: either the two isolated neutral points or the single isolated neutral point. However, the modulation scheme should control the zero-sequence currents in the single neutral point arrangement.

4.3.1.2. Modulation

Two approaches can be used to apply SVM to six-phase inverters, namely, the vector space decomposition (VSD) [47] method and the vector classification technique (VCT) [72]. The VCT method is adopted in this context for its simplicity in implementation. Following the abovementioned rules, just two out of the twelve switches in the six-phase inverter can be turned on per switching cycle. Consequently, there are only $2^6 = 36$ available combinations for this type of six-phase topology. Out of the 36 possibilities, 18 states (12 active + 6 null) represent a separate operation of the two CSIs by turning on two switches from the same three-phase CSI wholly and only turning off the other CSI.

These 18 states have an advantage over the other remaining available ones because selecting between these states prevents the problem of compensating for zero sequence components. The problem originates from the fact that while operating two phases from two different CSIs, only one phase is activated during the switching cycle in each three-phase group leading to possible zero sequence components. For this reason, these 18 states are selected, which in principle represent duplicating the available states in the three-phase case.

4.3.1.3. Stresses and sizing

In this subsection, the stresses of the inverter semiconductors are analyzed first, followed by the dc-link inductor and chopper converter discussion. An assumption is implemented here that either the phase current or voltage ratings are halved in six-phase systems compared to three-phase counterparts while both systems have the same power rating.

The stresses of the semiconductor switches of the inverter in P-CSI can be deduced from its operation. The switch on-state current stress is the same as the dc-link current since no current split

occurs in CSI at any switching state. Since only one CSI can be turned on at a time during each modulation cycle, the utilization of the dc-link current in the P-CSI is halved compared to the three-phase CSI. This point is crucial regarding the sizing of the whole powertrain components that employ the P-CSI. For the six-phase systems running at half the current rating of their equivalent three-phase counterparts, the dc-link current required in P-CSI is equal to the same as the one needed in the three-phase case.

The blocked voltage stress is considered the voltage that appears between the terminals of the turned-off semiconductors during the states of operation. For the turned-off switches of the legs that have other turned-on switches, The appearing voltage is the load line-to-line voltage (V_m) which is the difference between the phase voltage associated with that leg and the phase voltage associated with the other active leg. Meanwhile, the switches in the legs that do not have any active switches share the line-to-line load voltage. For example, the switching state I_2 is applied to CSI₁ as shown in Figure 4.5 to show the voltage and current stresses.

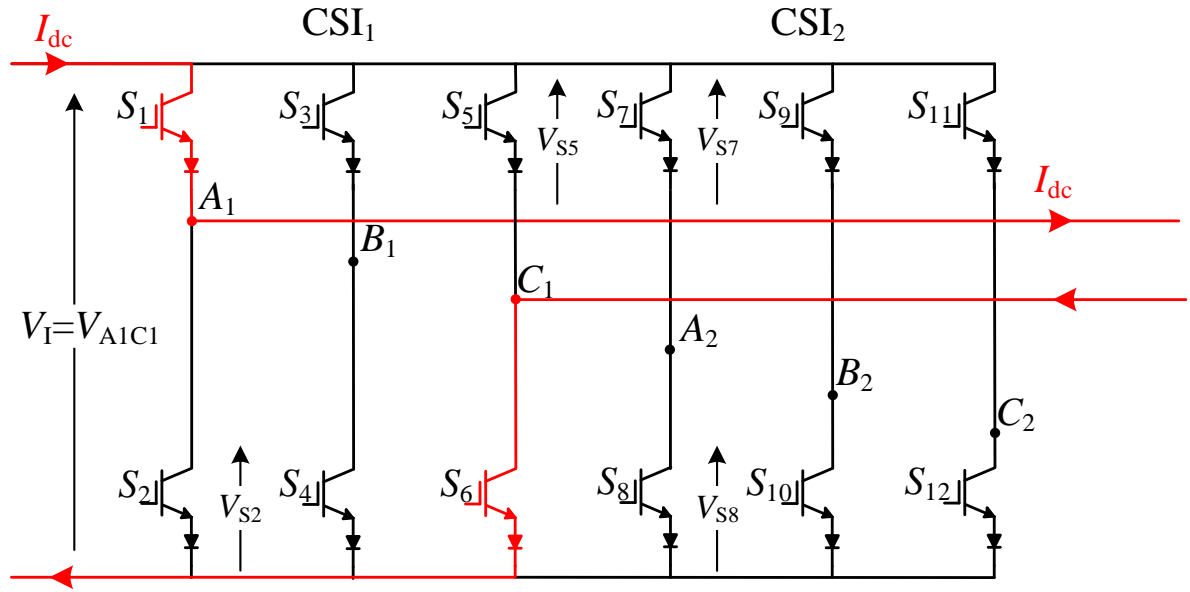


Figure 4.5 P-CSI operating in the switching state I2 {S1+S6} for CSI1 as an example to show the voltage and current stresses.

According to Kirchhoff's Voltage Law (KVL), The Stresses on switches S_2 and S_5 , the off switches in the active legs, equal the dc-bus voltage. Meanwhile, the stresses on switches S_7 and S_8 , switches of an inactive leg, share the dc-link voltage as $V_{S_7} + V_{S_8} = V_I$. It can be easily deduced also that the dc-link voltage is equal to the line-to-line voltage as $V_I = V_{A_1C_1}$. Based on the analysis, the highest possible blocked voltage that can appear across any switch is the maximum value of the line-to-line load voltage.

The chopper converter operates to compensate for the switching nature of V_I (is the voltage that appears across the input of the CSI). The blocked voltage stress for all the semiconductors of the chopper converter is the battery voltage. At any switching state, the two devices conducting are connecting the battery to the output terminals. Meanwhile, the current stress is still the dc-link current.

The inductor coil must withstand the dc-link current and the maximum expected ripple current regarding the dc choke. In addition, the inductance of the choke and the controllers tuning determine the current ripples in the dc-link current. Furthermore, the average inductor current should follow a dc reference with minimal current ripples at a certain steady-state operating point, assuming properly tuned controllers and ideal conditions. Hence, it is vital to choose a minimized inductance value so that the ripples are within an acceptable range and the cross-sectional area of the wiring of the choke coil and the overall size of the choke is also acceptable. To develop a simplified selection method, the voltage equation of the inductor is shown in terms of the CSI's input and chopper converter's output voltages as in (4.2).

$$V_L = V_B - V_I = L \frac{dI_{dc}}{dt} \quad (4.2)$$

Since the voltage V_I varies over time due to the switching actions nature of the CSI. Compensation is applied from the chopper converter at the other side of the dc choke voltage so that a zero-average voltage of V_L can be achieved each sampling period. Hence, the excitation part, the left side of Eq (4.2), can be minimized, and the change in the dc-link current is minimized. This rule maintains the current level of the dc-link. Hence, the choke's inductance should have a high enough inductance to suppress the current ripples accompanying the dc-link current. The ripples are generated because the voltages V_B and V_I are not equal instantaneously. They are equal over a sampling period T_s as the controller attempts to make the average appearing voltage V_B is equal to V_I each sample. The criteria chosen in this context is a simplified approach to picking an appropriate value of the choke's inductance. The discretized version of (4.2) is shown in (4.3) and rearranged to get the expression for calculating the inductance.

$$V_L(k) = V_B(k) - V_I(k) = L \frac{\Delta I_{dc}(k)}{T_s}$$

And after rearranging: (4.3)

$$L = \frac{V_B(k) - V_I(k)}{\Delta I_{dc}(k) \cdot f_s}$$

In the next section, the case study of the proposed powertrains, some assumptions are made, and Eq. (4.3) is employed after modifications to estimate the inductance required for proper operation. An important note is that the battery voltage should be at least high enough as the highest possible voltage that can appear as V_I . From the analysis of the P-CSI stresses earlier, the voltage V_I is equal to the line-to-line voltage, which depends on the switching state of the P-CSI. Hence the battery voltage must be equal to or greater than the maximum of the line-to-line voltage of the motor without applying boosting capability [16]. The blocked voltage stress for all the semiconductors of the chopper converter is the battery voltage. At any switching state, the two devices conducting are connecting the battery to the output terminals. Meanwhile, the current stress is still the dc-link current.

4.3.2. Proposed Cascaded-CSI Based Powertrain (C-CSI) (Configuration 2)

4.3.2.1. Structure

In the C-CSI topology, the two three-phase inverters are connected in cascade as shown in Figure 4.6 and fed from a single dc-dc converter.

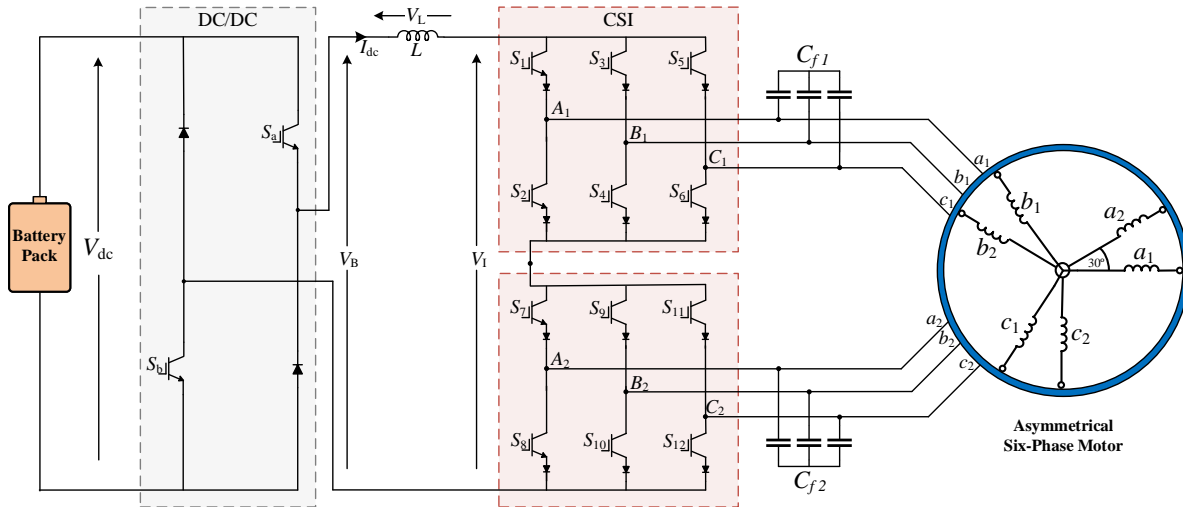


Figure 4.6 New powertrain configuration based on six-phase cascaded CSI (Configuration 2).

The dc-current flows from CSI₁ and the load group abc_1 , then to CSI₂ and group abc_2 , then back to the supply. By connecting the two CSIs in this configuration, higher dc-link voltages can be maintained, which has proven beneficial in the case of HVDC farms. Unlike P-CSI, the six-phase load cannot be connected in a single neutral configuration for proper operation reasons, explained later in the modulation section.

4.3.2.2. Modulation

In the C-CSI topology, the two CSIs are connected in a cascade, allowing the current to flow from one group (CSI and load) to the other, resulting in more than two legs operating simultaneously. The upper CSI does not disrupt the operation of the lower CSI and vice versa if the dc-link current is not interrupted at the coupling point P, as shown in Figure 4.6. All the possible nine states of three-phase CSI can be applied to both inverters CSI₁ and CSI₂, enabling the opportunity to maximize the utilization of the dc-link current.

Figure 4.7 illustrates the difference in the modulation strategies between P-CSI and C-CSI for better understanding. A modulation method adopted from the VCT of VSI is presented and discussed in [13], where the two inverters are operated based on the realizing two references displaced by 30° . The SVM switching patterns are optimized to minimize the dc-link current ripples between the ac rectifier and motor side inverter.

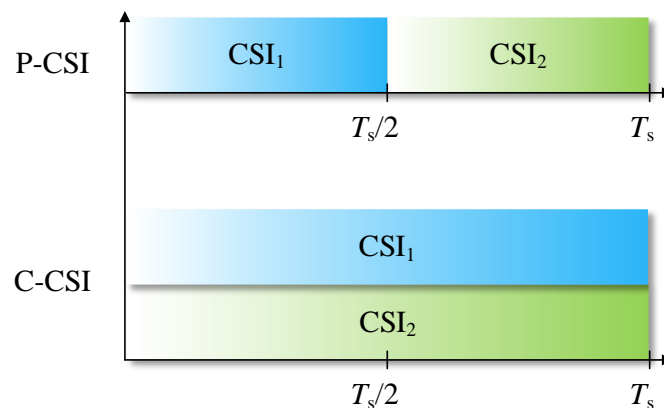


Figure 4.7 Time diagram to show the key difference between the modulation of P-CSI and C-CSI.

4.3.2.3. Stresses and sizing

The current stress is similar across all the switches in all the CSI topologies, which are equal to the dc-link current. However, two essential points must be highlighted here. First, the dc-link current required in the C-CSI topology is half the value of the one in the P-CSI case. Secondly, the conduction time of each semiconductor is increased compared to the P-CSI case since both CSIs have switches turned on all the time. Consequently, the reduced current stress and increased conduction instants affect the conduction loss, resulting in approximately the same power loss as

P-CSI. Regarding the blocked voltage on the inverter switches, like the P-CSI, the turned-off switches of the C-CSI must withstand the line-to-line voltage of the active phases in each CSI. For example, as shown in Figure 4.8, if switching state I_2 is applied to CSI₁ and I_6 to CSI₂, V_{s2} becomes equal to $V_{A_1C_1}$, and V_{s2} equals $V_{C_2B_2}$.

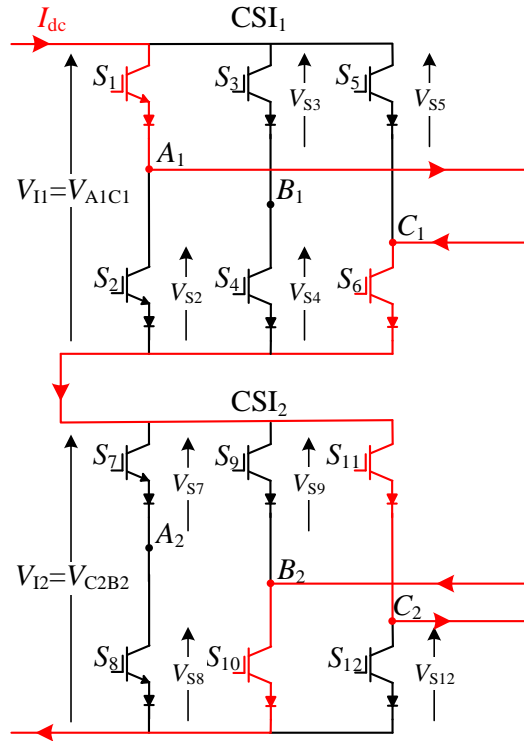


Figure 4.8 C-CSI operating in the switching state I_2 { S_1+S_6 } for CSI₁ and I_6 { S_5+S_4 } for CSI₂ as an example to show the voltage and current stresses.

Regarding the dc-dc converter, the switches must withstand the dc-link current, which is reduced to half compared to the P-CSI case. The blocked voltage is the same as the battery voltage V_B , which is different in the case of C-CSI. Following the evaluation done in the P-CSI section, the battery voltage must be at least equal to the highest instantaneous value of V_I . The voltage V_I is the summation of the two voltages resulting in the input of both CSI₁ and CSI₂, V_{I1} and V_{I2} , respectively. Both V_{I1} and V_{I2} are equal to the line-to-line voltage of their corresponding CSI.

The highest possible VI can be calculated by summing one phase from group 1 with the three possible voltages from group 2 individually since the other combinations will give similar results, just different in phase shift. For example, considering line voltage $V_{A_1B_1}$ from the first group, the three possible combinations are shown in Figure 4.9 with the aid of phasor diagrams.

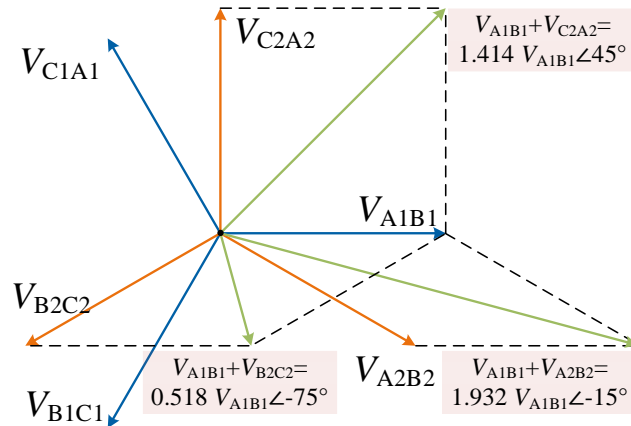


Figure 4.9 Phasor diagram of the summations of line voltages $V_{A_1B_1}$ and $V_{A_2B_2}$, $V_{B_2C_2}$, $V_{C_2A_2}$.

The phasors are drawn assuming that the line voltage $V_{A_1B_1}$ is the reference and the other voltages are at the same magnitude and shifted in time by the correct phase shift in asymmetrical six-phase systems. Apparently, the highest combination in magnitude is the one between voltages $V_{A_1B_1}$ and $V_{A_2B_2}$.

It is worth mentioning that this deduction is subject to the power factor angle and the switching instants. From a design perspective, the worst-case scenario must be taken into consideration. The occurrence of the maximum value $1.932|V_{A_1B_1}|$ is dependent on the coincidence between two events. One event is that the voltage V_i is at its peak value. The other is when the same active switching states are applied to both CSIs. Consequently, the battery voltage

and the semiconductor devices must be designed to be at around double the level employed in P-CSI. The choke inductor design is also affected by this change.

4.3.3. Proposed Standalone-CSI Based Powertrain (S-CSI) (Configuration 3)

4.3.3.1. Structure

Unlike in P-CSI and C-CSI, the two three-phase CSIs are fed from one dc-dc converter, and they are supplied separately from a dedicated dc-dc converter as in Figure 4.10.

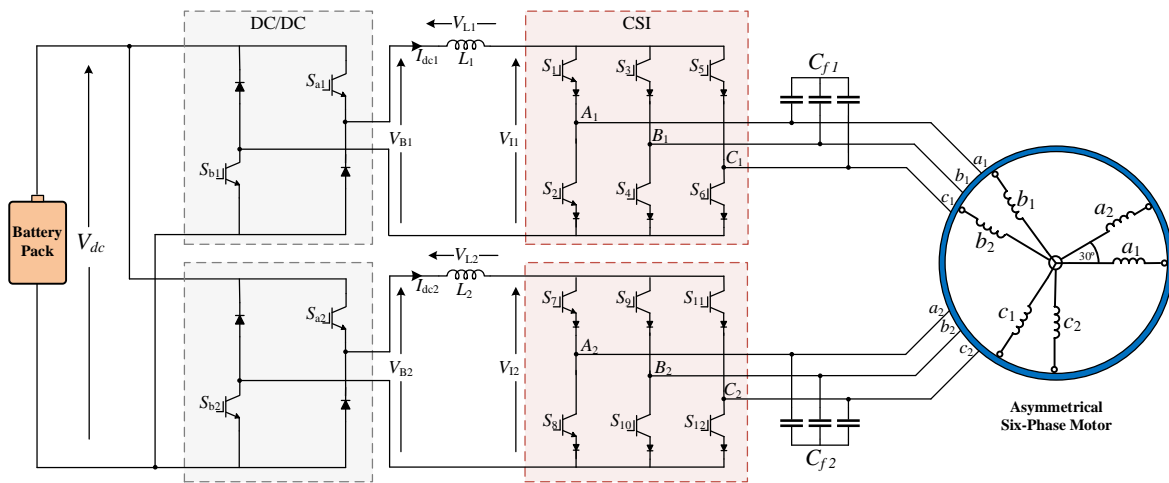


Figure 4.10 New powertrain configuration based on six-phase standalone CSI (Configuration 3).

The benefits of this variation are getting a similar dc-link current utilization as the C-CSI while eliminating the requirement almost to double the system's battery voltage to ensure proper operation of the dc-dc converter. The separation of the two inverters makes the only possible configuration of the load connections is the two isolated neutral points as in the C-CSI. In this topology, the two dc-dc converters can be connected to a separate dedicated battery pack or both converters to one main battery pack. However, this point is not covered in this context.

4.3.3.2. Modulation

The modulation of the S-CSI is dependent on the dc-link currents to be adequately controlled. Assuming the two currents are held at the same level as in the C-CSI case, the exact strategy applied to the C-CSI topology can be used in the S-CSI. The current level needed for both converters would be equal to the one in the C-CSI, which is half the three-phase case. The controllers of the dc-dc converters work separately based on the measurements of the two dc links currents. The possibility to operate at different levels of dc-link currents is not covered in this context.

4.3.3.3. Stresses and sizing

The current stress in the two CSIs is the same as in the C-CSI case, as the same dc-link currents are assumed to be achieved for a proper operation. The blocked voltages are again the same as the C-CSI since, in any active case, the maximum blocked voltage is the line-to-line voltage which is the difference between the phase voltage of the two active phases. As for the dc-dc converters, the current stresses are the same as in the case of the C-CSI powertrain. However, the blocked voltages are different since, in this case, the two CSIs are separated. The separation results in lower values of the voltages V_{I1} and V_{I2} compared to the C-CSI case. Each input voltage to the two CSIs, V_{I1} and V_{I2} , is equal to the line voltage correspondent to the applied active switching states. Unlike the C-CSI configuration, these two voltages are not summed up. The two dc-dc converters compensate them for maintaining the currents I_{dc1} and I_{dc2} with minimum ripple currents. Consequently, the required level of the battery voltage is the same as in the three-phase and P-CSI cases.

This configuration has mixed merits from the P-CSI and C-CSI simultaneously. Still, the increased number of components might come across as a concern regarding the power density of the powertrain. However, a critical remark that must be highlighted while comparing all the

configurations is the sizing aspect. Since the stresses on the semiconductors are the lowest overall compared to P-CSI and C-CSI configurations, the need to connect switches in parallel or series to withstand specific stresses is eliminated. Instead, the same number of semiconductors can be used and controlled separately. This approach is better from a control and operation perspective because turning on and off switches in series or parallel has many problems. These problems arise from the difference in the characteristics due to the manufacturing processes and the gate drivers. These differences result in non-concurrent timings of turning on/off actions and the load sharing difference between the connected devices resulting in a challenging thermal management design to account for these problems.

4.4. Case Study

This study compares the proposed configurations with the three-phase one, considered the benchmark. An eight-pole PMSM rated at 150 kW peak power is used as the traction motor. The motor is rated at 250 V line voltage (V_m), 175 A phase currents (I_m) to develop 240 N.m torque at 1200 RPM base speed. The assumptions made to size all the components in the powertrain are enlisted as follows:

- The sizing in all the configurations should accommodate the power levels required by both supply and load sides so that every stage can work properly.
- Every component is selected to withstand 150% to 200% (or the following rating of commercially available modules) of the voltage and current stresses.
- Maximum dc-link ripple currents are at 10% of the average dc current ($I_{dc,av}$).

- The switching frequency for the chopper $f_{s,Chopper}$ and CSIs $f_{s,CSI}$ in all configurations are fixed to 50 kHz and 10 kHz, respectively.
- The maximum inductor voltage is selected based on the maximum value of the inverter input voltage ($V_{I,max}$) that can occur while applying $V_B = 0$.
- The filtering capacitors are the same in all the configurations since the selection is based on fixed features such as motor characteristics and the switching frequency of inverters.

The sizing methodology starts by assessing the motor needs and accommodating them from the CSI side. Then, the dc-link requirements and finally the dc-dc converter side. The dc-link current and the battery voltage must be appropriately selected to deliver power to the motor at the rated values. Starting with the dc-link current, the utilization limits that have been discussed earlier are employed in this section. For P-CSI, the dc-link current must be at least double the value of the maximum rated motor current ($2\sqrt{2}I_{ph} = 500$ A). However, for C-CSI and S-CSI, the required dc-link value must be at least ($\sqrt{2}I_{ph} = 250$ A).

The battery voltage is discussed in the previous section, and the required voltages are at least ($2\sqrt{2}V_m = 707$ V) for the C-CSI case while ($\sqrt{2}V_m = 353$ V) are sufficient for the P-CSI and S-CSI. Hence, the selected voltages are 800 for the C-CSI and 400 for both the P-CSI and S-CSI. Based on assumptions (1) and (2), the sizing for the IGBTs for the CSI in every configuration is shown in Table 4.1.

Table 4.1 Comparison between three-phase CSI, P-CSI, C-CSI and S-CSI

		Three-phase CSI	P-CSI	C-CSI	S-CSI
Battery	Voltage	400 V (4 IGBTs + 4 diodes)	400 V (4 IGBTs + 4 diodes)	800 V (4 IGBTs + 4 diodes)	400 V (4 IGBTs + 4 Diodes)
Chopper	Components	Each 2 IGBTs/diodes are connected in parallel	Each 2 IGBTs/diodes are connected in parallel	Each 2 IGBTs/diodes are connected in series	Each 2 IGBTs/diodes form a separate chopper
	Ratings	600 V, 400 A	600 V, 400 A	600 V, 400 A	600 V, 400 A
	Current	500 A	500 A	250 A	250 A
DC-link Choke	Inductance	140 μ H	140 μ H	532 μ H	2 \times 280 μ H
	Insulation	1 kV 12 RB-IGBTs	1 kV 24 RB-IGBTs	2 kV	1 kV
Inverter	Components	Each 2 IGBTs/diodes are connected in parallel	Each 2 IGBTs/diodes are connected in parallel	12 RB-IGBTs	12 RB-IGBTs
	Ratings	600 V – 400 A	600 V – 400 A	600 V – 400 A	600 V – 400 A
AC filter	Total Cap.	30 μ F	60 μ F	60 μ F	60 μ F

All the cases use the same ratings for fair comparison based on the required number of switches. As mentioned in Table 4.1, the lowest overall stresses on the inverter switches are associated with the S-CSI configuration. The ratings selected can completely withstand the stresses of the S-CSI, and in all the other cases, the stresses are higher than the selected ratings. Consequently, an increased number of switches is required in all the other configurations. The stresses in the other configurations, such as the three-phase case, are twice the rating of the selected current rating of the switches, so every two switches are connected in parallel. The exact sizing is applied to the P-CSI case since the same current stress is unavoidable.

The voltage ratings of all the switches are based on the maximum line-to-line voltage of the motor. The filtering capacitors are appropriately selected to avoid placing the resonance effect with the motor inductances at the fundamental harmonic. The leakage inductance per phase for the

model is at $10 \mu\text{H}$. The capacitance is selected to place the resonance effect at the 12th harmonic resulting in a $10 \mu\text{F}$ per phase based on (4.4) [139].

$$C_f = \frac{1}{(2\pi f_{res})^2 L} \quad (4.4)$$

Regarding the dc-link inductor sizing, the selection requirements are the minimum inductance to meet the assumptions, withstanding the maximum instantaneous and average dc-link current and insulation level higher than the voltage stress across the inductor. Building on Eq (4.3), the selection of the dc-link inductor is executed based on (4.5) accounts for assumptions (4.3), (4.4), and (4.5).

$$L = \frac{10 V_{I,\max}}{I_{dc,av} f_s} \quad (4.5)$$

The inductance values are stated in Table 4.1, and the lowest values are achieved in the P-CSI and three-phase cases. However, a higher ampacity rating is required for both cases since the dc-link currents must be 500 A. The maximum instantaneous current is around 550 A in the worst-case scenario since 10% ripple currents are assumed to be achieved. As for the C-CSI, higher possible instantaneous dc-link inverter voltage results in a higher inductance value to maintain the same ripple current constraint. The S-CSI has a lower inductance value per dc-link; however, two inductors are required.

The dc-dc converter switches are sized based on the stresses determined by the voltage battery and dc-link current. Both the three-phase CSI and P-CSI cases have the exact sizing. Four switches and four diodes are used to implement one dc-dc converter by paralleling every two semiconductors to withstand the current stress. Meanwhile, the dc-dc converter in the C-CSI case

is comprised of the same number of switches and diodes, but every two are connected in series to withstand the voltage stress. The S-CSI has two dc-dc converters. Each one is implemented by two switches and two diodes with ratings stated in Table 4.1.

4.5. Experimental Results

4.5.1. Experimental Setup

A scaled-down prototype is used for the experimental test as illustrated in Figure 4.11 to verify the feasibility of the proposed modulation scheme.

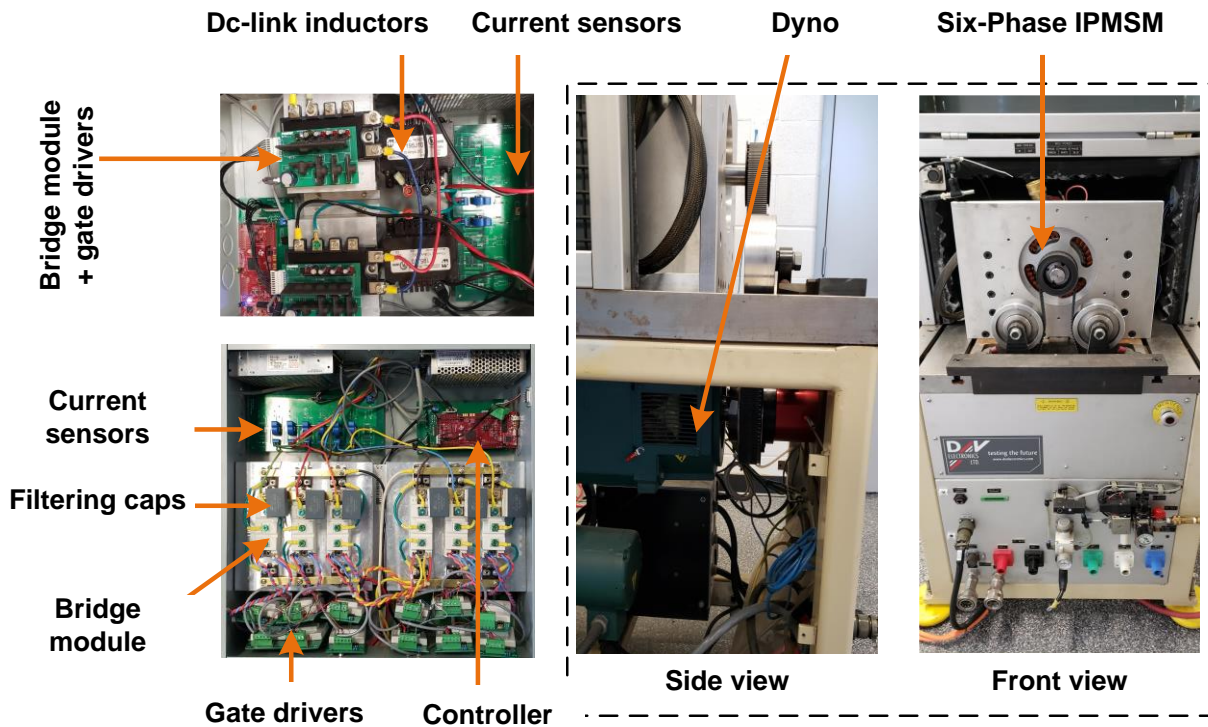


Figure 4.11 The experimental setup to test the proposed scheme.

The dc-dc converter is implemented using the IGB modules PM50RL1A120 from Mitsubishi rated at $V_{ces} = 1200\text{V}$ and $I_c = 50\text{A}$. Two switches and two diodes are utilized to implement the dc-dc converter from each module. A six-phase C-CSI is implemented by six half-bridges SKM50GB12V IGBT modules connected to SKHI 22 A/B H4 gate drivers from Semikron.

The reverse blocking is achieved by connecting each half-bridge to a DSEI2x31-06C diode module one diode to clamp each IGBT to the positive and negative rails. A LAUNCHXL-F28379D digital signal processor generates the firing signals. A six-phase IPMSM is used as the load in the experiment. The parameters of the motor are enlisted in Table 4.2. The motor in the experiments is operated at 350 rpm, which is the same load torque of 31.6 N.m. The dc-link current is set to 8A for the P-CSI case and 4A for C-CSI and S-CSI. The dc voltage is set to 200V for the P-CSI and S-CSI cases and 400V for the C-CSI case. The loading is achieved by coupling the motor mechanically to a belt starter generator (BSG) from D&V Electronics (model: HT-250). The BSG also regulates the dc-supply by providing a battery emulator. The motor is controlled using FOC, and the operational mechanical point is kept the same to validate and compare the proposed configurations. The D&V Pro software sets the dc-supply voltage and the loading torque.

Table 4.2 PARAMETERS OF THE MOTOR LOAD UNDER THE SIMULATION STUDY

Symbol	Parameter	Value
P_n	Rated power	3 kW
T_n	Rated torque	70 N.m.
ω_n	Rated speed	405 rpm
P	Pair of poles	17
R_s	Stator resistance	1.3 Ω
L_d	D-axis inductance	13.576 mH
L_q	Q-axis inductance	13.926 mH
L_{xy}	xy inductance	4.076 mH
ψ_d	PM flux	0.156 Wb
f_s	Switching frequency	10 kHz
C_f	Filtering capacitor	10 μ F

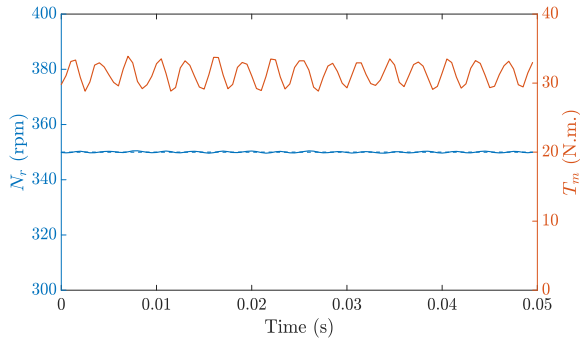
4.5.2. Experimental results

The motor runs at 350 rpm for the three configurations, meeting a load torque requirement at 31.6 N.m. by adjusting the dc voltage and dc-link current values. In the P-CSI topology, the dc-link current is set to 8A since the dc-link utilization is limited to half the full range. The results acquired for the P-CSI configuration are shown in Figure 4.12. The speed and torque of the motor are shown in Figure 4.12(a). The dc-link current I_{dc} and the inverter output i_{A1} are illustrated in Figure 4.12(b), which shows that the dc-link current is regulated at 8A, and the ripples are minimized. The motor phase currents (i_{a1} , i_{b1} , i_{a2} , i_{b2}) and phase voltages (v_{a1} , v_{b1} , v_{a2} , v_{b2}) are presented in Figure 4.12(c) and (d). The currents and voltages are nearly sinusoidal and are at the correct phase shifting in asymmetrical six-phase loads. The speed is settled around the reference point 350 rpm. The buck voltage V_b and the inverter dc-link voltage V_I , i.e., the voltages before and after the dc-link inductor, are presented in Figure 4.12(e). The buck converter attempts to counter the voltage across the inductor so that the dc-link current remains constant. The results emphasize that this operational point could only be achieved by setting the dc-link current and battery voltage to the values mentioned earlier.

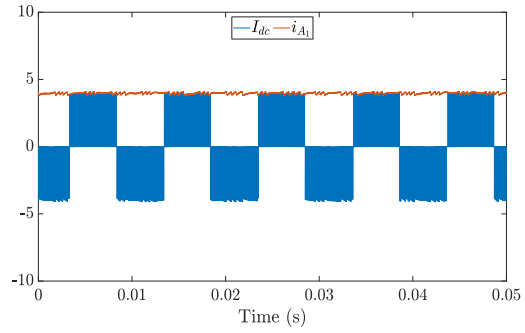
Regarding the C-CSI, the battery voltage is changed to 400V, and the dc-link current is set to 4A. The speed and torque, in this case, are shown in Figure 4.13(a). They are similar to the P-CSI case for a fair comparison. The dc-link current and inverter phase current for phase A1 are shown in Figure 4.13(b), and the difference in the C-CSI case is that the current is fixed at 4A, which can be fully utilized for the motor currents. The motor phase currents and voltages are shown in Figure 4.13(c) and (d), and they are at the same level as the ones from the P-CSI but at half the value required for the dc-link. The second difference is the level of the inverter voltage that appears in this configuration which is higher as analyzed in earlier sections. The voltages before and after

the inductor are shown in Figure 4.13(e), which confirms that a higher battery voltage is necessary to compensate for the inverter dc-link voltage, which can be at almost double the line-to-line voltage.

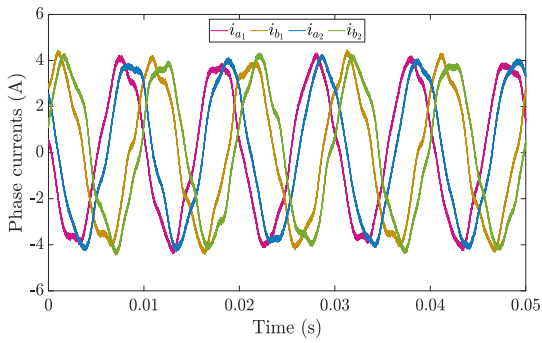
Regarding the S-CSI, the setting is modified to be 200V for the battery and 4A to the dc-link voltage. As shown in Figure 4.14(a), the mechanical conditions are satisfied as in the previous cases. Figure 4.14(b) and (c) show both groups' dc-link currents and inverter currents. At the same time, Figure 4.14(d) and (e) show the motor phase currents and voltages. The figures show that the results are similar to the other configurations. However, the results of the two dc-dc converters are different in this case, as shown in Figure 4.14(f) and (g). The dc-link currents are regulated efficiently by the two dc-dc converters.



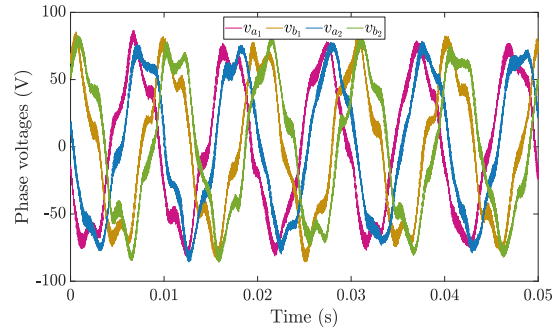
(a) Motor speed and torque.



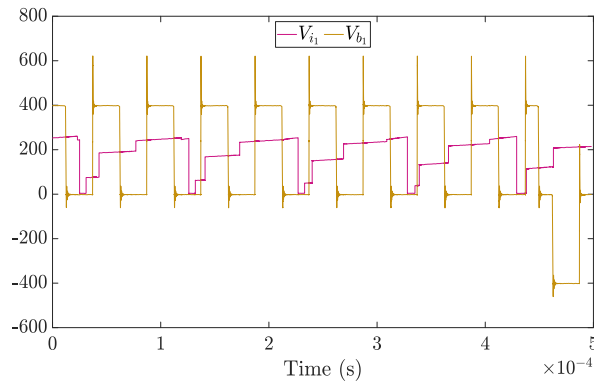
(b) Dc-link and inverter output currents in Amperes.



(c) Motor phase currents.

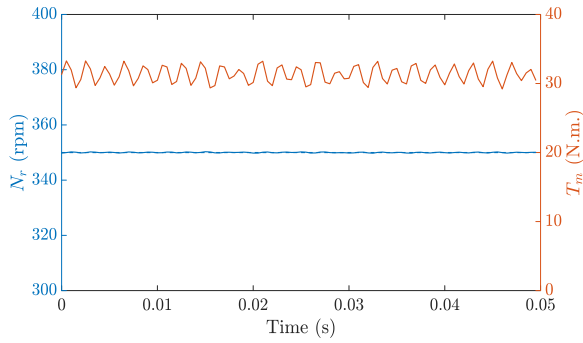


(d) Motor phase voltages.

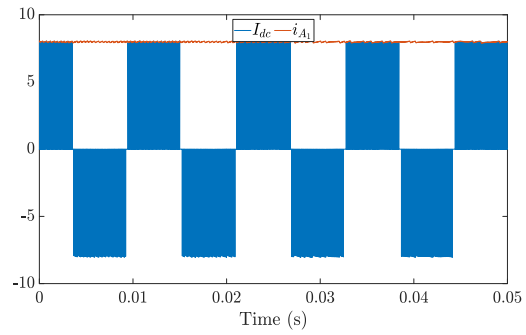


(e) Buck and dc-link inverter voltages in Volts.

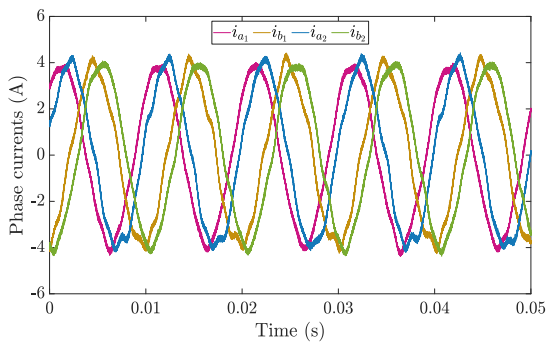
Figure 4.12 Experimental results of the C-CSI configuration at motor speed = 350 rpm at load torque = 31.6N.m.



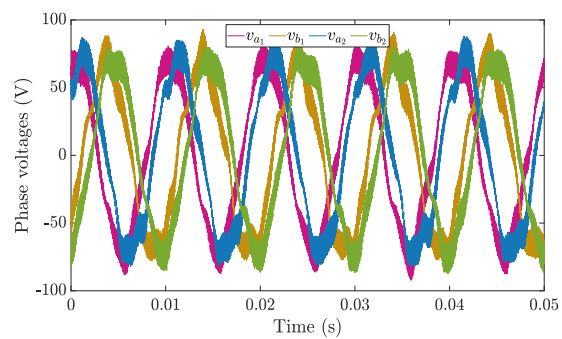
(a) Motor speed and torque.



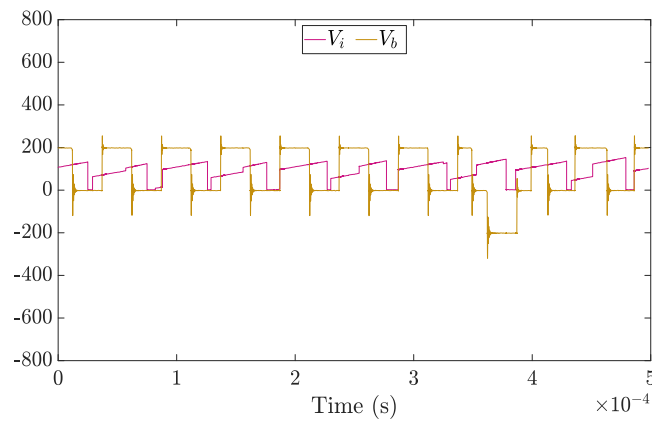
(b) Dc-link and inverter output currents in Amperes.



(c) Motor phase currents.

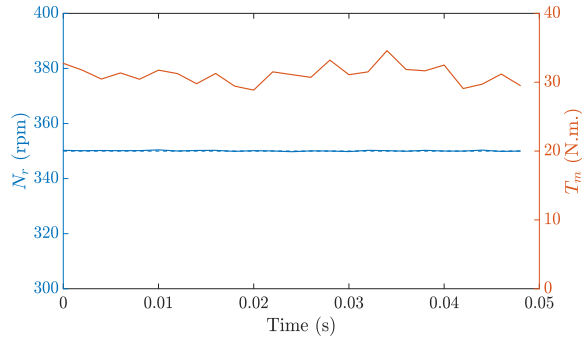


(d) Motor phase voltages.

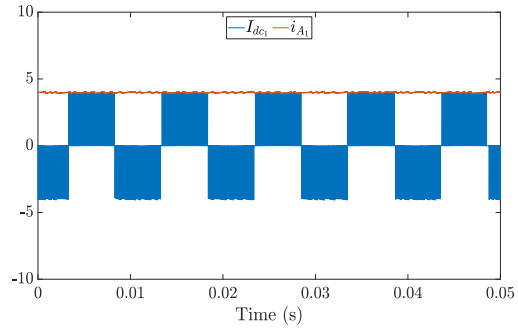


(e) Buck and dc-link inverter voltages in Volts.

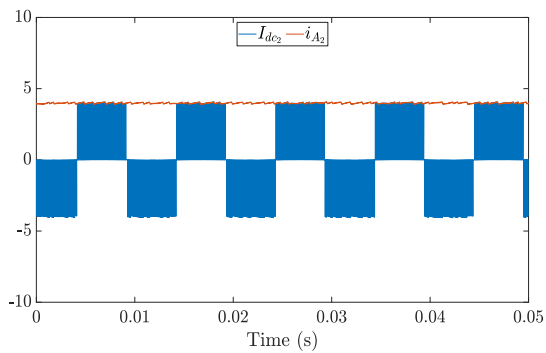
Figure 4.13 Experimental results of the P-CSI configuration at motor speed = 350 rpm at load torque = 31.6N.m.



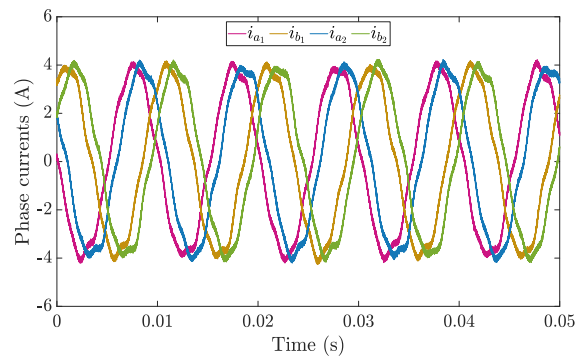
(a) Motor speed and torque.



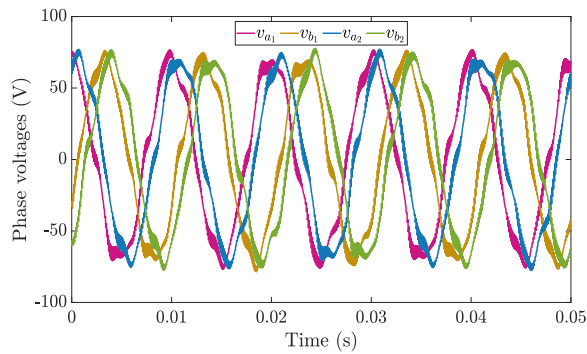
(b) Dc-link and inverter output currents in Amperes for group abc1.



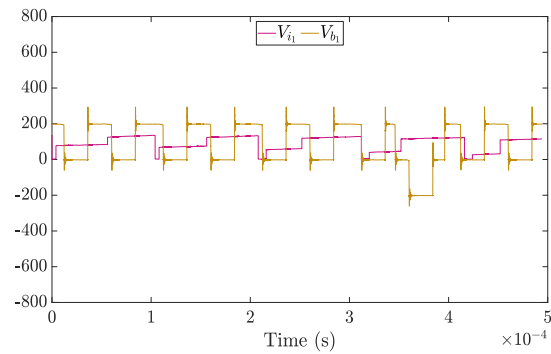
(c) Dc-link and inverter output currents in Amperes for group abc2.



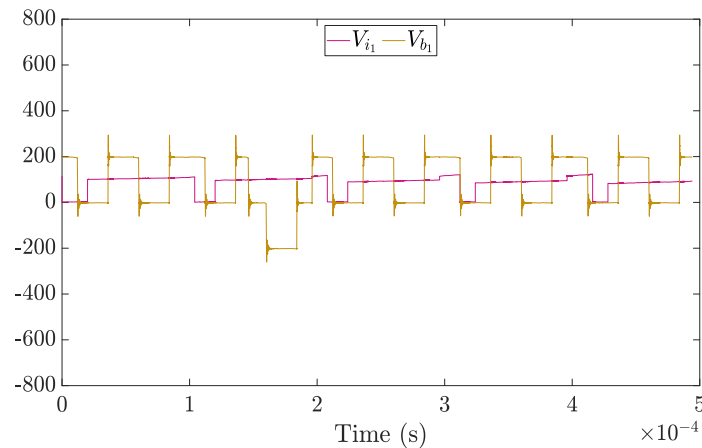
(d) Motor phase currents.



(e) Motor phase voltages.



(f) Buck and dc-link inverter voltages in Volts for group abc1.



(g) Buck and dc-link inverter voltages in Volts for group abc2.

Figure 4.14 Experimental results of the S-CSI configuration at motor speed = 350 rpm at load torque = 31.6N.m.

4.6. Summary

This chapter presents a proposal to build a powertrain for HDEV based on combining six-phase PMSMs and CSI. Three possible configurations are investigated based on the connection between the two three-phase groups, leading to the P-CSI, C-CSI, and S-SCI. The comparison between the three configurations shows that the C-CSI is more suitable for applications with high supply voltages, such as HVDC windfarms. The P-CSI is not a favorable configuration since it requires an increased number of switches to withstand the current stresses.

The S-CSI is the most suitable configuration among the three proposals since it compromises the stress requirements and the number of components while maintaining the desired voltage and current levels in multiphase systems. The experimental results agree with the case study comparison since adjusted dc voltage or dc-link current are applied in the cases of C-CSI and P-CSI, respectively, to achieve the exact operation of S-CSI.

Chapter 5

A New Space Vector Modulation technique for Six-Phase Standalone-CSI (S-CSI) with Extended Linear Modulation Range

5.1. Introduction

The development of space vector modulation (SVM) techniques to utilize the features of such systems is one of the attractive research topics in multiphase inverters. Using VSD modeling, the SVM method can control the harmonics in different subspaces [68, 69, 140]. Ordinarily, the reduction of the harmonics is the main target of most techniques to increase the system's efficiency and maintain thermal limits [70].

Moreover, in two-level VSI multiphase inverters, the modulation range can be extended linearly using the additional degrees of freedom [141, 142]. The penalty of such a feature is the

increased harmonic content in the output voltage waveform, which implicates increased losses and lower efficiency. This topic is exciting since the trade-off can achieve beneficial gains outweighing the drawbacks by optimizing the harmonic content required to achieve the extension. This approach has been investigated for five-phase systems [143] and six-phase ones [144-146]. In these methods, an objective function is defined based on the harmonic content in the extra subspaces, and the optimization process aims to achieve the desired modulation index in the fundamental subplane with the minimum possible harmonic content in the other subplanes.

The SVM based on the VSD method has been discussed for five-phase CSI [17, 22]. In both works, an extension method of the dc-link current utilization is achieved by using the same ratio between the large and medium vectors in [22] or by injecting a third harmonic component in the additional subspace as in [17]. C-CSI modulation has been discussed in [13] based on the *double-dq* method which is manipulated in the previous chapter. However, to the best of the authors' knowledge, a realization of SVM based on VSD for S-CSI and extension of dc-link utilization has not been investigated. The contributions of this chapter are enlisted as the following.

The proposed method adopts the two large and two medium vectors modulation scheme to control the modulation index linearly from zero to the maximum. Minimized harmonic content is achieved using zero-average Ampere-second balance per switching sampling period by utilizing the analogy between VSI and CSI systems.

An extension of the modulation index range by around 8% is targeted with minimum injected harmonics in the xy using a new proposed approach based on stored, operating points in a look-up table (LUT) for fast and easy implementation of the scheme.

The work presented in this chapter is distinguished from the VSD-based for VSIs in devising the modulation in the extension region. In the proposed method, a backward approach is developed. The desired output after harmonic injection is shaped, and the ability of S-CSI is checked to produce such reference. Then, the operating points are stored in a LUT to recall while needed to achieve a desired modulation index in the extension range. On the contrary, in the previous methods for VSI, the possible inverter states are studied in the extension region, and the schemes are based on optimizing all the possible solutions based on the geometry of the selected vectors. The proposed method can also be generalized easily to other multiphase CSIs based on each case's available degrees of freedom. Another advantage of the proposed method is that the dwell time calculation remains the same over the whole modulation range, unlike the previous extension works for VSIs. The proposal mimics the harmonic injection methods used for torque density improvement, such as in [33, 34], only using SVM rather than tuning several proportional-resonant controllers as in VSI-based systems.

5.2. Modeling of a Six-Phase S-CSI

5.2.1. Operation of a Six-Phase S-CSI

The structure of a six-phase cascaded CSI is shown in Figure 5.1. The S-CSI comprises two three-phase CSIs connected in series. The dc-link current I_{dc} passes from one inverter to the other one, as shown in Figure 5.1. This structure allows the modulation of the two inverters separately, which means full utilization of the dc-link current.

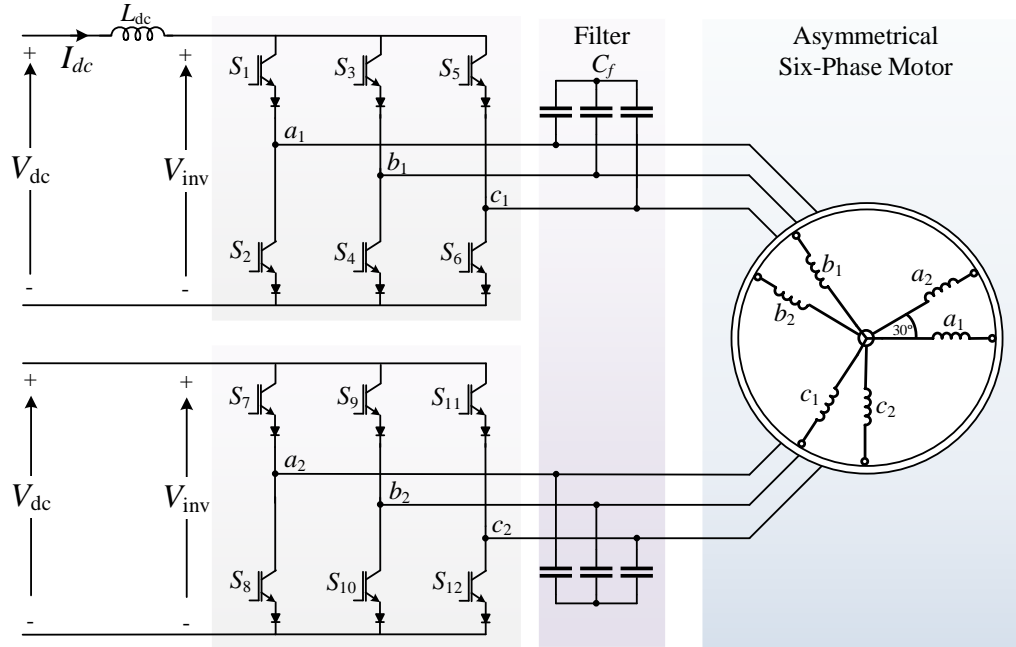


Figure 5.1 The standalone six-phase CSI (S-CSI) topology for $2N$ configuration.

Two conditions of operation must be followed to operate CSIs properly. The first condition is that the I_{dc} must be continuous without any interruption. The second condition is to produce a predefined output current waveform. This condition allows only two out of the six switches to be turned on simultaneously in each three-phase inverter. It should be noted that the only valid neutral point configuration that can be applied here is the $2N$ configuration. There are nine possible switching states for each three-phase CSI [137, 147], and thus in total, there are 81 possible switching states for the six-phase S-CSI. The output currents produced by the possible switching state can be calculated using (5.1):

$$\begin{bmatrix} i_{a1} \\ i_{b1} \\ i_{c1} \\ i_{a2} \\ i_{b2} \\ i_{c2} \end{bmatrix} = \begin{bmatrix} S_1 - S_2 \\ S_3 - S_4 \\ S_5 - S_6 \\ S_7 - S_8 \\ S_9 - S_{10} \\ S_{11} - S_{12} \end{bmatrix} I_{dc} \quad (5.1)$$

where S_j , $j = \{1, 2, \dots, 12\}$ is the state of the inverter switch and i_{a1} to i_{c2} are the phase currents.

5.2.2. Vector Space Decomposition (VSD)

The VSD method decomposes machine variables (voltage, current, and flux) into three two-dimensional subspaces. The three subspaces are orthogonal to each other; hence decoupled variables are mapped to each subspace. The first subspace is called the $\alpha\beta$ subspace. As in the Clarke transformation, the $\alpha\beta$ subspace represents all the harmonics of the order $l = 12h \pm 1$, $h = (1, 2, 3, \dots)$ which impact the electromechanical conversion process (i.e., torque producing harmonics). The second subspace is called xy subspace, and harmonics of the order $l = 6h \pm 1$, $h = (1, 3, 5, \dots)$ are mapped to it and considered as loss components. The final subspace is the representation of the triplen harmonics or the zero-sequence harmonics $l = 3h$, $h = (1, 3, 5, \dots)$ and is referred to as the 0_+0_- subspace. The xy and the 0_+0_- subspaces do not contribute to the torque production process, and they are losses harmonics.

A transformation matrix is deduced mathematically in [47] to transfer six-phase currents into the three subspaces. This transformation is based on the phase shift angle between the two-three phase group sets and the angles between the phases in each group and is given in (5.2):

$$\begin{bmatrix} i_\alpha \\ i_\beta \\ i_x \\ i_y \\ i_{0+} \\ i_{0-} \end{bmatrix} = \frac{1}{\sqrt{3}} \begin{bmatrix} 1 & -\frac{1}{2} & -\frac{1}{2} & \frac{\sqrt{3}}{2} & -\frac{\sqrt{3}}{2} & 0 \\ 0 & \frac{\sqrt{3}}{2} & -\frac{\sqrt{3}}{2} & \frac{1}{2} & \frac{1}{2} & -1 \\ 1 & -\frac{1}{2} & -\frac{1}{2} & -\frac{\sqrt{3}}{2} & \frac{\sqrt{3}}{2} & 0 \\ 0 & -\frac{\sqrt{3}}{2} & \frac{\sqrt{3}}{2} & \frac{1}{2} & \frac{1}{2} & -1 \\ 1 & 1 & 1 & 0 & 0 & 0 \\ 0 & 0 & 0 & 1 & 1 & 1 \end{bmatrix} \begin{bmatrix} i_{a1} \\ i_{b1} \\ i_{c1} \\ i_{a2} \\ i_{b2} \\ i_{c2} \end{bmatrix} \quad (5.2)$$

The new variables are decoupled and can be controlled to achieve the desired performance, such as desired power transfer and power factor control for grid-tied applications or the torque-speed references for motor drives applications.

5.2.3. Mapping of the Current Components

The VSD method can help to map the output current vectors into the three-decoupled subspaces using all the possible switching states. Since the load is connected in the $2N$ configuration, the current components in the 0_+0_- subspace are all nullified. The current components are shown in Figure 5.2. These output currents components are the result of applying all possible switching states and can be determined by using Eq. (5.1) and (5.2). Each vector is referred to as I_p as $p \in \{1, 2, \dots, 81\}$.

The mapped components are classified in this context based on their magnitude in the $\alpha\beta$ subspace, shown in

Table 5.1. The group I_L has the largest $\alpha\beta$ components and the smallest xy components. The classified components as I_{M1} have equal magnitudes in both $\alpha\beta$ and the xy subspaces. It is worth noting that the two groups I_L and I_{M1} have components that are out of phase in the xy subspace,

which can be exploited in the modulation scheme. The vectors from the other groups have lower magnitudes compared to the others.

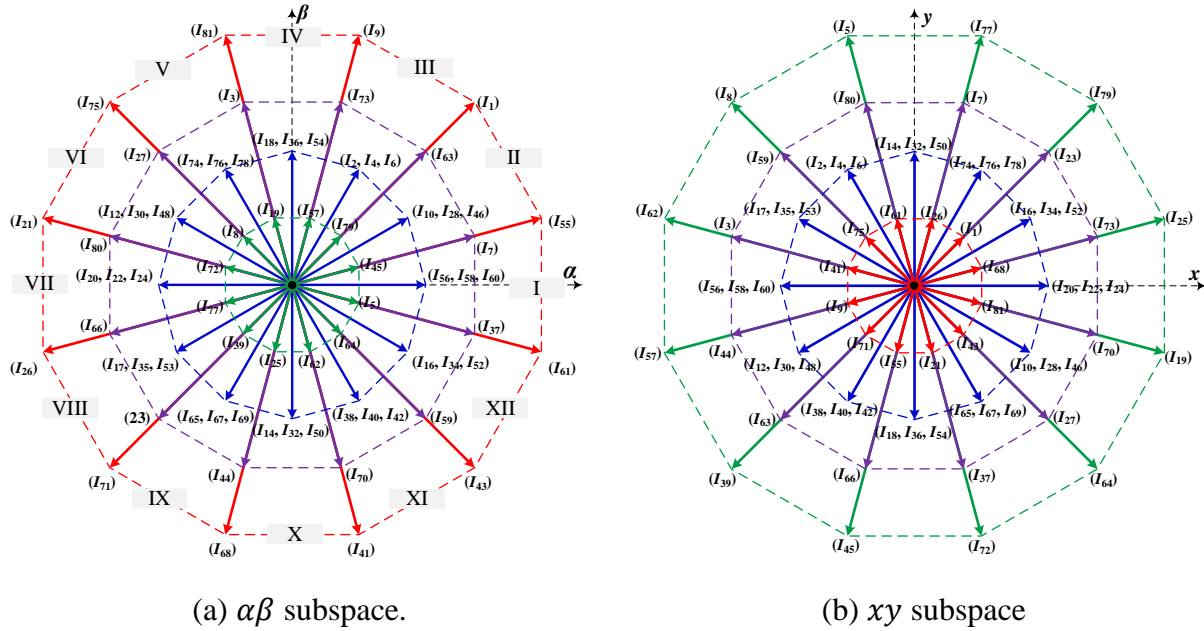


Figure 5.2 Projection of possible output states of the S-CSI structure using the VSD method.

Table 5.1 CATEGORIES OF CURRENT VECTORS
BASED ON THE STATES OF S-CSI

Group	Quantity	Color
I_L	$(\sqrt{3} + 1)I_{dc}/\sqrt{2}$	—
I_{M1}	$(\sqrt{2})I_{dc}$	—
I_{M2}	I_{dc}	—
I_S	$(\sqrt{3} - 1)I_{dc}/\sqrt{2}$	—

5.3. The Proposed Modulation Technique

In this section, the proposed approach introduces two regions for the modulation index. The first region (Region I) covers from zero to the highest modulation index. In this region, the VSD-based SVM technique is employed to diminish the unwanted xy harmonics and obtain sinusoidal output currents. The second region (Region II) is the extension region, in which the proposed method is applied to achieve the highest possible modulation index (1.08) while minimizing harmonic components.

5.3.1. Proposed VSD-based SVM technique for S-CSI

The $\alpha\beta$ subspace can be divided into twelve sectors. The numbering of the sectors is shown from I to XII in Figure 5.2(a). When a reference vector is located in each sector, the reference vector can be synthesized by selecting four active vectors and one null vector. In the proposed approach, a five-segment switching sequence cycle is also considered. The method is based on the analogy between VSI and CSI. Hence, two vectors are chosen from the large group (I_L), and the other two vectors are chosen from the (I_{M1}) group as in [146]. The large and medium vectors are selected such that each large vector is in the same direction as the medium vector in the $\alpha\beta$ subspace. Meanwhile, they are out of phase in the xy subspace. One example in Sector I is shown in Figure 5.3.

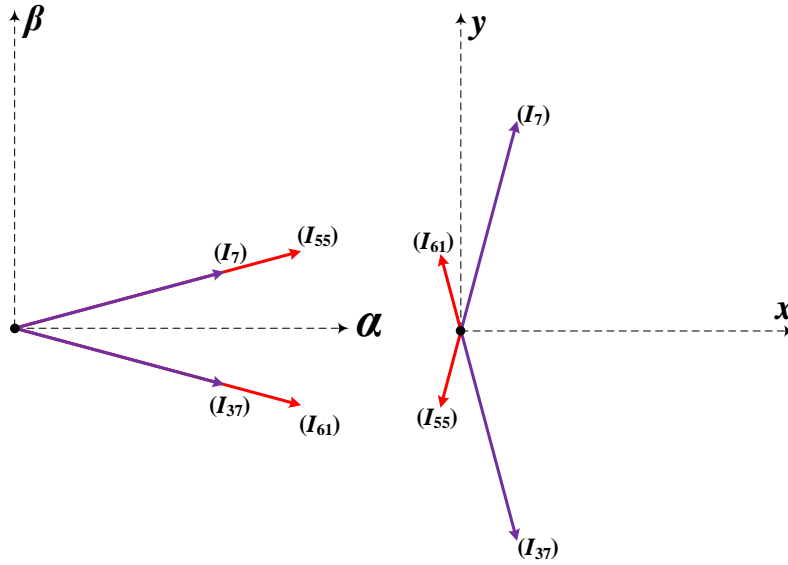


Figure 5.3 The selected vectors for sector I.

The calculation of the dwell times is given in (5.3) in the same manner as six-phase VSI [33]. The calculation method is based on synthesizing the selected vectors and the reference into their respective α, β, x, y components:

$$\begin{bmatrix} t_1 \\ t_2 \\ t_3 \\ t_4 \\ t_0 \end{bmatrix} = \underbrace{\begin{bmatrix} I_1^\alpha & I_2^\alpha & I_3^\alpha & I_4^\alpha & 0 \\ I_1^\beta & I_2^\beta & I_3^\beta & I_4^\beta & 0 \\ I_1^x & I_2^x & I_3^x & I_4^x & 0 \\ I_1^y & I_2^y & I_3^y & I_4^y & 0 \\ 1 & 1 & 1 & 1 & 1 \end{bmatrix}}_C^{-1} \begin{bmatrix} i_r^\alpha \\ i_r^\beta \\ i_r^x \\ i_r^y \\ 1 \end{bmatrix} T_s \quad (5.3)$$

where T_s is the switching period. t_1 to t_4 are the dwell times of the selected active vectors per sector I_1 to I_4 , respectively. In Eq. (5.3), the current components I_g^γ , $\gamma \in \{\alpha, \beta, x, y\}$ refers to the axis of synthetization of the component, and $g \in \{1, 2, 3, 4\}$ refers to the order of the selected vector to represent a sector of modulation. Meanwhile i_r^γ refers to the decoupled reference current components. Since the aim of this chapter is to apply VSD modeling to extend the maximum

modulation index in S-CSI, only vectors from the I_L and I_{M1} groups are considered in the following discussions.

5.3.2. Regions of Operation

Two regions of operation for the proposed scheme are defined and studied. This categorization is based on the designated level of harmonics allowed in the output currents of the S-CSI. The following subsections define the set limits of the output harmonics for each region, and it is explained how to modulate the scheme accordingly:

4.3.2.1. Region I (min. harmonics region)

Undoubtedly, the lower the harmonic content in the output current can lead to higher efficiency and better system thermal performance. However, the harmonics could contribute to the output power or torque production [7, 42]. In Region I, the goal is to linearly change the modulation range from zero to maximum with the low content of the xy subplane harmonics. This can be done by setting the references i_r^x, i_r^y to zero in the dwell times calculations in Eq. (5.3). The modulation index (m) is defined as the ratio between the amplitude of the fundamental component of the reference inverter currents $|i_{f_1, max}^{inv}|$ and the dc-link current I_{dc} . Hence, the six-phase reference currents vector, i_r^{inv} can be realized using Eq. (5.4):

$$[i_r^{inv}] = \begin{bmatrix} i_{a1} \\ i_{b1} \\ i_{c1} \\ i_{a2} \\ i_{b2} \\ i_{c2} \end{bmatrix} = m I_{dc} \begin{bmatrix} \cos(\theta) \\ \cos(\theta - 120^\circ) \\ \cos(\theta - 240^\circ) \\ \cos(\theta - 30^\circ) \\ \cos(\theta - 150^\circ) \\ \cos(\theta - 270^\circ) \end{bmatrix} \quad (5.4)$$

Based on the fundamentals of pulse width modulation, as the modulation index increases, the null time decreases. Hence, the maximum modulation index in Region I ($m_{max}^{Reg. I}$) can be

determined by determining the equation to calculate the null time (t_0). Since the dwell times of the inverter are periodically repeated in every sector, studying one sector of modulation is enough to calculate t_0 . For instance, the following procedure obtains the null time equation in sector I. To determine the t_0 first, all the components on the right-hand side in (5.3) must be defined. The components I_g^y of the selected active vectors ($I_{61}, I_{37}, I_7, I_{55}$) in sector I should be substituted in (5.3). Then, by using the VSD transformation given in (5.2), the reference currents can be mapped into the decoupled reference current components i_r^y shown in (5.5):

$$\begin{cases} i_r^\alpha = \sqrt{3} m I_{dc} \cos(\theta) \\ i_r^\beta = \sqrt{3} m I_{dc} \sin(\theta) \\ i_r^x = i_r^y = 0 \\ i_r^{0+} = i_r^{0-} = 0 \end{cases} \quad (5.5)$$

The 0_+0_- References are physically realized because of the neutral connection applied in the S-CSI. Consequently, there is no need to include the last branch of Eq. (5.5) in the following calculations. The reference output currents i_r^y given in (5.5) should be substituted in (5.3) to determine the null time equation in sector I, and it is described in (5.6).

$$t_{0,\text{sector I}} = T_s(1 - m \cos(\theta)) \quad (5.6)$$

To achieve $m_{max}^{Reg. I}$, two variables in Eq. (5.6) must be determined; the values of θ and $t_{0,\text{sector I}}$. The angle that represents the minimum null time value is $\theta = 0^\circ$ which makes the cosine term in Eq. (5.6) becomes maximum. By substituting for θ , Eq. (5.6) becomes as (5.7).

$$(t_{0,\text{sector I}})_{min}|_{\theta=0} = T_s \left(1 - (m_{max}^{Reg. I}) \right) \quad (5.7)$$

The null time $t_{0,\text{sector I}}$ at $m_{\text{max}}^{\text{Reg. I}}$ reaches zero, which is the minimum realizable null time. By equating (5.7) to zero, the $m_{\text{max}}^{\text{Reg. I}}$ deduced is equal to one. That means the ability of the six-phase S-CSI to realize the maximum fundamental output currents ($|i_{f_1}^{\text{inv}}|$) with zero-average xy harmonic currents. Figure 5.4 shows the null time over two sectors at the maximum modulation index inside Region I. It is worth mentioning that applying a zero-average Ampere balance does not guarantee the total elimination of the harmonic currents in the xy subplane. However, a minimized harmonic content can be achieved by using such a technique [47].

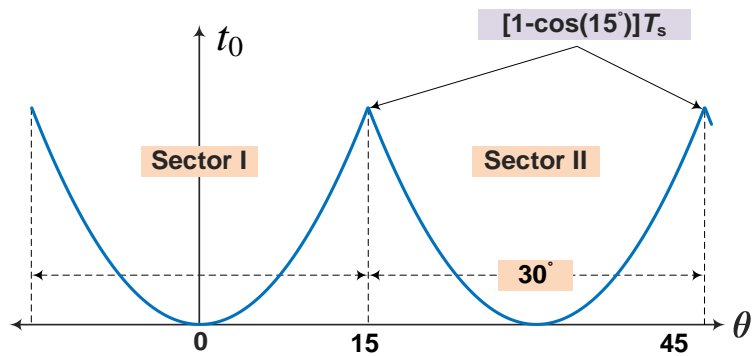


Figure 5.4 Null time at the maximum modulation index.

4.3.2.2. Region II (extension region)

In Region II, the target of the proposed SVM is to take advantage of the S-CSI system and achieve the full dc-link utilization linearly. The proposal is to calculate and inject appropriate harmonic content in the xy to produce a higher fundamental component than Region I. The dwell time calculations in (5.3) can be used without changes. Unlike the triplen harmonics, the xy harmonics can flow without any hardware reconfiguration [43].

The harmonics mapped to the xy subspace are of the order $l = 6h \pm 1$, $h = (1, 3, 5, \dots)$ as mentioned in the VSD section. The general formula of the output current waveform after injecting the xy harmonics is shown in (5.8):

$$i_o = I_{dc} \left[m \cos(\theta) + \left(\sum_{h=1,3,5,\dots}^{\infty} k_{6h-1} \cos((6h-1)\theta + \varphi_{6h-1}) + k_{6h+1} \cos((6h+1)\theta + \varphi_{6h+1}) \right) \right] \quad (5.8)$$

Where k is the per-unit (p.u.) value of the injected harmonics and φ is the phase-shifting angles of the waveforms.

To obtain the form of the xy current components in the reference, every reference phase current in the reference vector $[i_r^{inv}]$ stated in (5.4) should be modified to include the injected currents as in (5.8). Then, by applying VSD transformation and simplifying the formulas, the current references injected in the xy subspace are shown in (5.9):

$$\begin{aligned} \begin{bmatrix} i_r^x \\ i_r^y \end{bmatrix} &= \sqrt{3} I_{dc} \sum_{h=1,3,5,\dots}^{\infty} k_{6h-1} \begin{bmatrix} \cos((6h-1)\theta + \varphi_{6h-1}) \\ \sin((6h-1)\theta + \varphi_{6h-1}) \end{bmatrix} \\ &+ k_{6h+1} \begin{bmatrix} \cos((6h+1)\theta + \varphi_{6h+1}) \\ -\sin((6h+1)\theta + \varphi_{6h+1}) \end{bmatrix} \end{aligned} \quad (5.9)$$

The next step is to determine the optimum values of the coefficients k . An optimization process is developed here to find these coefficients. The optimization aims to find the minimum harmonic content to be injected to extend the modulation range into Region II. The objective function (obj) is defined in (5.10), and it consists of the summation of the squared values of the coefficients. The optimization problem is to find the minimum of obj for each modulation index in Region II. The constraint is also illustrated in (5.11), representing the feasibility of applying the dwell times. These times calculated by (5.3) must be greater than or equal to zero at the values of k selected by the optimization process. The optimization problem can be solved using MATLAB software by deploying the `fmincon()` function with the MultiStart option.

$$obj = \sqrt{\sum_{h=1,3,5,\dots}^{\infty} (k_{6h-1})^2 + (k_{6h+1})^2} \quad (5.10)$$

subjected to

$$[t_1 \ t_2 \ t_3 \ t_4 \ t_0] |_{\text{calculated at the selected } k_{rs}} \geq [0 \ 0 \ 0 \ 0 \ 0] \quad (5.11)$$

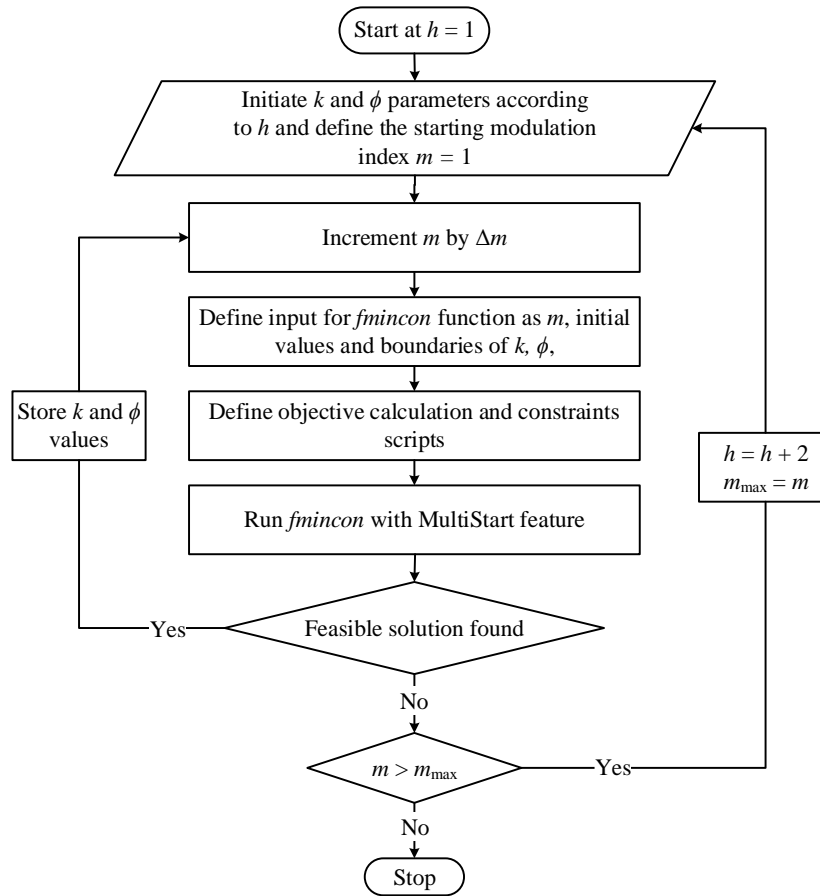


Figure 5.5 The flowchart of the optimization process to select the amplitudes and angles of the injected xy harmonics.

Since the formula in (5.9) is infinite, an algorithm is applied to determine a finite number of essential harmonics to get an applicable solution. The algorithm starts with $h = 1$ and attempts to

solve the optimization with the modulation indexes beyond the limit of Region I. The optimization algorithm increases the values of m until no feasible solution can be found. This approach determines the maximum modulation index in Region II ($m_{max}^{Reg. II}$) while applying a certain h . The algorithm stops at $h = 3$ and achieves $m_{max}^{Reg. II} = 1.0773$. The $h = 3$ means that the essential harmonics to be injected are the 5th, 7th, 17th, and 19th to ensure a feasible modulation. It is worth mentioning that considering cases with $h > 3$ would increase the accuracy of implementation and reduce the harmonic content. However, a trade-off is made to stop at $h = 3$ because of increased problems with higher harmonics regarding the implementation. The selection of the filtering capacitors and switching frequency are other motives to stop at $h = 3$. The optimum values of all coefficients are shown in Figure 5.6 when the modulation index changes from 1 to 1.0773 in Region II.

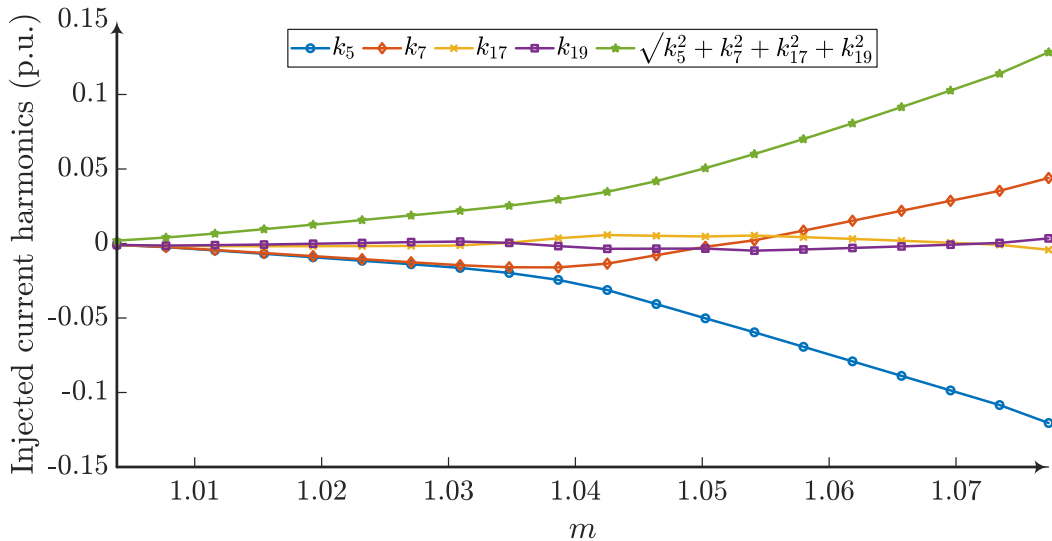


Figure 5.6 The results of the optimization process with unlimited injection.

As shown in Figure 5.6, the amplitudes of the optimal injected harmonics are not linearly increasing with the modulation index in Region II. The SVM method can be easily implemented

in Region II by storing the coefficients of the harmonics in the digital controller memory and recalling them when needed. Based on the deduced maximum modulation indexes in each region, the limits of the two regions can be illustrated geometrically in Figure 5.7. The two arcs in Figure 5.7 mark the end of the two regions. Region I realizes the references of magnitude up to $\sqrt{3}I_{dc}$. Region II ends at the outer circle with a perimeter equal to $1.0773\sqrt{3}I_{dc}$.

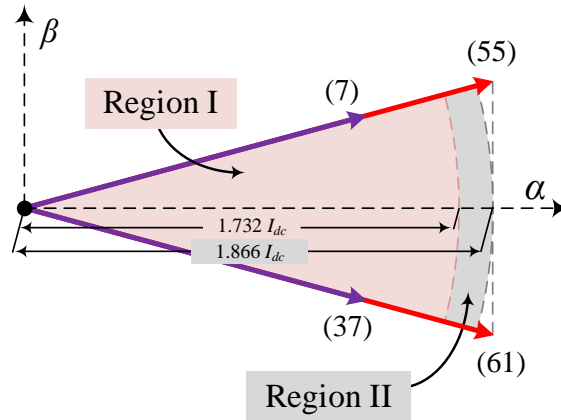


Figure 5.7 Linear modulation regions.

All the coefficients are calculated over the modulation range in Region II to check that the optimization problem results are feasible. Sector II is chosen to execute the check for feasibility since the dwell times are periodical, and one sector is enough for the check. The calculated dwell times are shown in Figure 5.8. Since all the times are positive, it can be concluded that the S-CSI can realize the selected harmonics for injection.

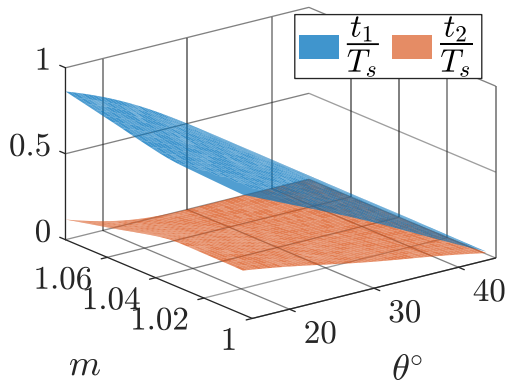
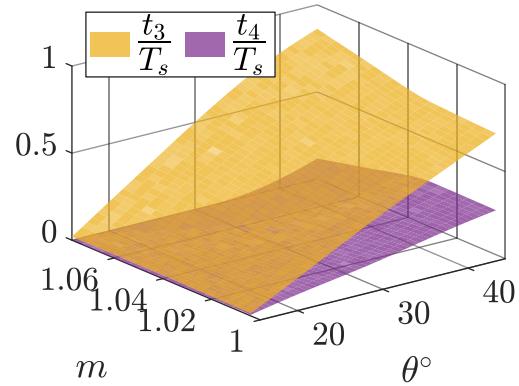
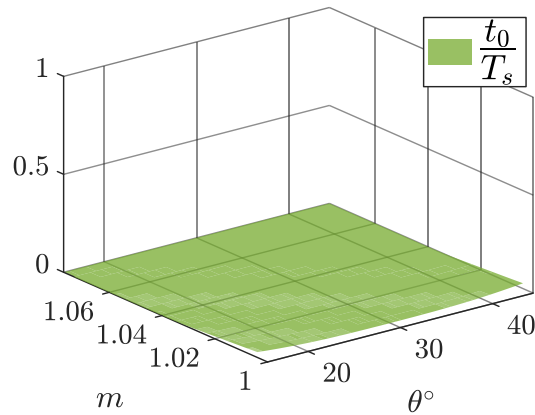
(a) Dwell times t_1, t_2 per T_s (b) Dwell times t_3, t_4 per T_s (c) Dwell times t_0 per T_s

Figure 5.8 Dwell times as ratios of the sampling time over section II based on the optimized coefficients for the injected harmonics.

5.3.3. Effect of Filtering Capacitors

A critical CSI output phenomenon is the resonance between the filtering capacitors and the load inductance. In this section, the per-phase equivalent circuit is studied to determine the relation between the output current of the inverter I_{inv} and the load current I_{load} after the filtering stage,

the main reason is to get a deeper understanding of the system to avoid the resonance effect. Another reason is to avoid amplifying or shifting the injected harmonics in the proposed extension method. The equivalent circuit of the filter capacitor and the load is shown in Figure 5.9. The transfer function between the inverter output and the load in the s -domain is described in (5.12) for the case of $R - L$ loads. For steady state analysis, one can substitute $s = j\omega$ to get the magnitude and angle of the transfer function G to analyze the filtering stage:

$$G(s) = \frac{I_{load}}{I_{inv}} = \frac{1}{1 + RC \cdot s + LC \cdot s^2} \quad (5.12)$$

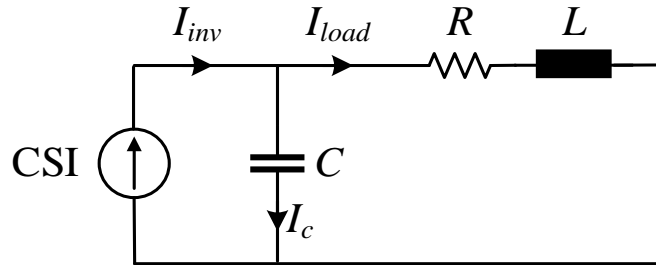


Figure 5.9 Per-phase equivalent circuit of the load and filtering stages.

For discussion and clarification, a system running at the parameters specified in Table 5.2 is illustrated as an example. Given that the system under study is a medium-power load, selecting the switching frequency of the CSI around the 5-10kHz range is suitable for such applications [148]. Using (5.13), three values of the filtering capacitor C_f are chosen such that the resonance frequency f_{res} would be at the (25th, 30th, 35th) harmonics.

$$C_f = \frac{1}{(2\pi f_{res})^2 L} \quad (5.13)$$

Table 5.2 parameters of the resistive-inductive load for filter selection study

Symbol	Parameter	Value
P_L	Rated power	250 kW
V	Rated voltage	210 V
f	Output frequency	60 Hz
f_s	Switching frequency	5 kHz
PF	Load power factor	0.9 lag
C_f	Filtering capacitor	30.7 μ F

The magnitude of G vs. a frequency range up to 50 kHz is presented in Figure 5.10 using bode plot. Meanwhile, the transfer function G angle is shown in Figure 5.11. It can be noticed from Figure 5.10 that the resonant frequency is at the selected harmonics, and the frequency span can be divided into three sections. The first one stretches from the beginning of the range of frequencies up to the resonance phenomenon. The second section is the resonance bandwidth, which is estimated at around the 70.7% of the maximum value of $|G|$. The third section is the filtering section, where the high frequencies get attenuated, such as the band around the switching frequency. From Figure 5.11, it can be deduced that the angles of the injected harmonics are barely changed, which makes the proposed SVM with harmonic injection method more powerful to be used for S-CSI topology.

Selecting the filtering capacitor must ensure the following point based on the previous discussion. The f_{res} must be placed between the significant harmonics and the switching frequency harmonics. In addition, the high the value of f_{res} , leads to selecting small filtering capacitors, as seen in (5.13). This approach can reduce the size of capacitors and thus improve the system's overall lifetime. A simple solution to compensate for the filter effect on the magnitude

and angle of the current is to employ an observer, which is introduced in [149] for motor drives applications.

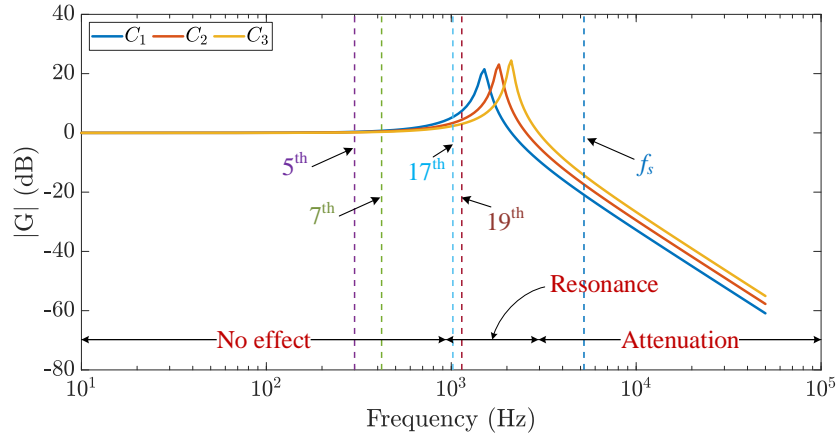


Figure 5.10 Bode plot of the magnitude of the transfer function G.

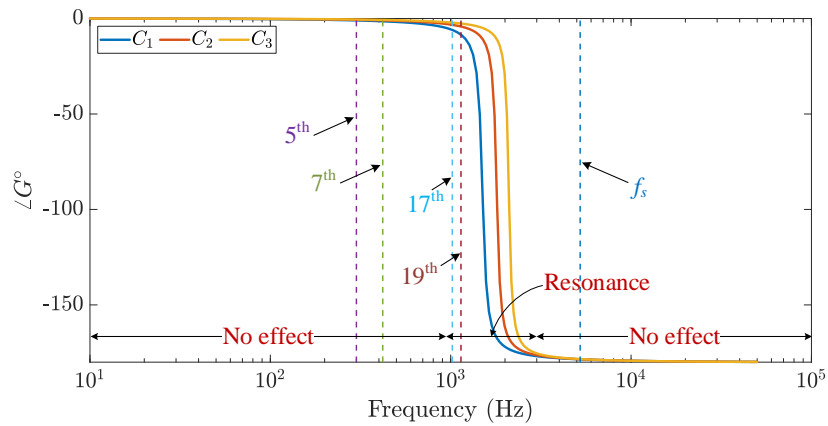


Figure 5.11 The angle of the transfer function G.

5.4. Simulation Studies

A simulation study is carried out in this section by developing a simulation model of an asymmetrical six-phase fed by a S-CSI and then demonstrating the results.

5.4.1. Simulation Model

The simulation model is based on the equations of six-phase IPMSM in the synchronous frame as described in (5.14) [150].

$$\begin{bmatrix} v_d \\ v_q \end{bmatrix} = \begin{bmatrix} R_s + L_d p & -\omega_e L_q \\ \omega_e L_d & R_s + L_q p \end{bmatrix} \begin{bmatrix} i_d \\ i_q \end{bmatrix} + \begin{bmatrix} 0 \\ \omega_e \psi_d \end{bmatrix} \quad (5.14)$$

$$\begin{bmatrix} v_x \\ v_y \end{bmatrix} = \begin{bmatrix} R_s + L_{xy} p & 0 \\ 0 & R_s + L_{xy} p \end{bmatrix} \begin{bmatrix} i_x \\ i_y \end{bmatrix}$$

where p is a differential operator, ω_e is the electrical angular speed. i_d , v_d , i_q , and v_q are the dq current and voltage components, respectively. i_x , i_y , v_x and v_y are currents and voltages in xy -subplane, respectively.

The developed torque T of the machine is described in (5.15).

$$T = \sqrt{3}P[\psi_d i_q + i_d i_q (L_d - L_q)] \quad (5.15)$$

The mechanical equation that governs the rotation of the machine is:

$$T - T_L = J\dot{\omega}_m + B\omega_m \quad (5.16)$$

where T_L is the load torque, J is the inertia and B is the friction coefficient and ω_m is the mechanical speed of the motor.

The control scheme is shown in Figure 5.12, including the implementation of the proposed scheme. The control scheme is built on the indirect field-oriented control (FOC) method d-axis current set to zero as the operation is in the below base speed region and filter capacitor compensation based on the equations in [151]. The index calculator in the block diagram is described in (5.17), and it is used to determine the operating point inside Region II of the inverter.

$$index = 1 - \frac{\sqrt{(i_r^\alpha)^2 + (i_r^\beta)^2}}{1.0773\sqrt{3} I_{dc}} \quad (5.17)$$

The output filtering capacitors are chosen to avoid resonance with the d -axis, q -axis, and xy inductances of the motor at one of the injected harmonics. In addition, the switching frequency is selected to be in the attenuation region of the filter effect. The parameters of an interior permanent magnet synchronous motor (IPMSM) are described in Table 5.3. The results of running the model to operate at base speed and 244 N.m. loading torque, then a step loading is executed to push the S-CSI into operating in Region II. The simulation results are shown in Figure 5.13, the motor speed and torque are demonstrated in Figure 5.13(a), which shows that the desired speed is achieved, and the motor counters the load torque developed torque. The results show that the transition is seamless between the two operation points, from Region I to Region II, of the inverter modulation. The motor phase currents are illustrated in Figure 5.13(b). The current peaks are below the dc-link current before the step loading; they saturate at the dc-link level after loading. The motor phase voltages are illustrated in Figure 5.13(c), and the effect of the harmonics takes place after loading as the S-CSI enters Region II of operation.

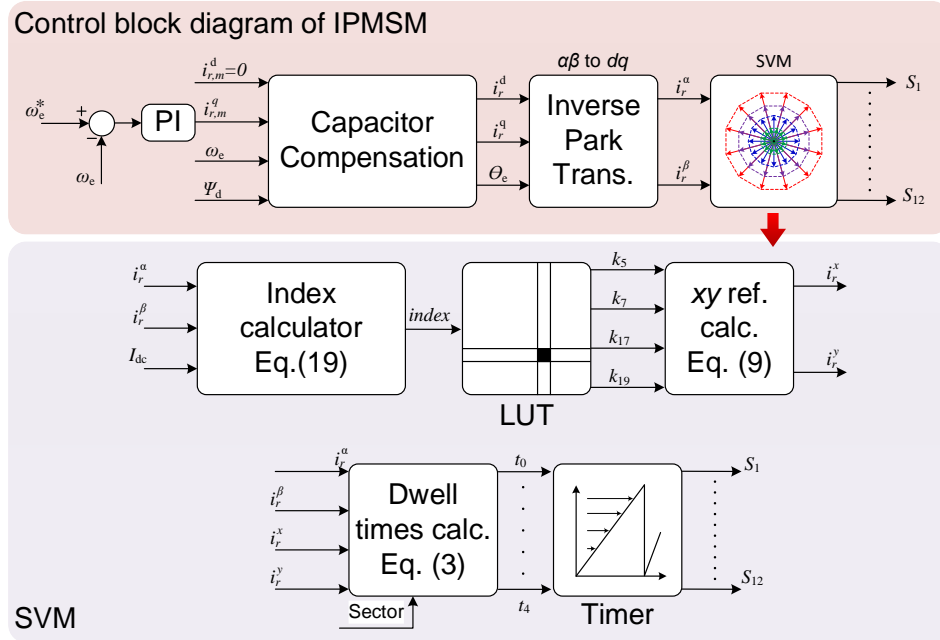
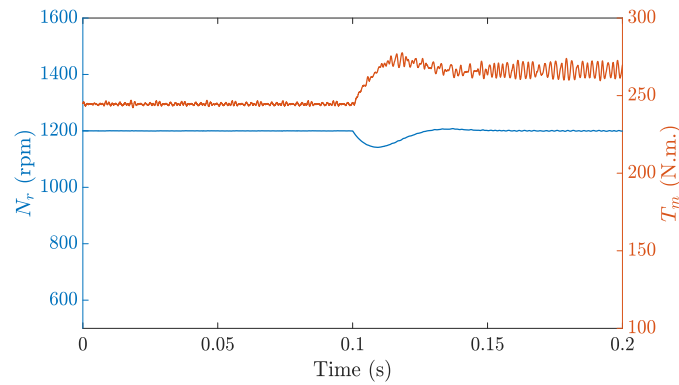


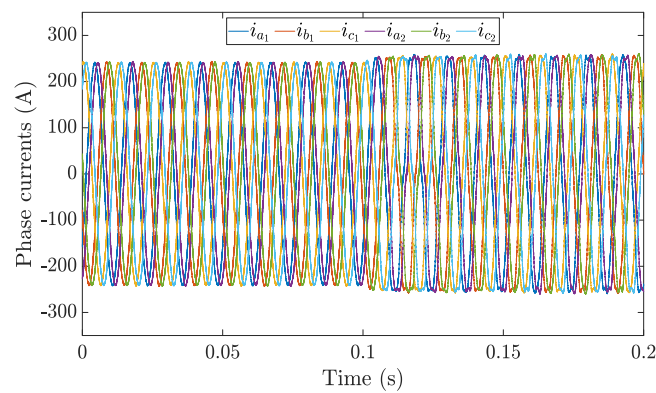
Figure 5.12 Control block diagram of the motor drive simulation to test the proposed scheme.

Table 5.3 parameters of the motor load under the simulation study

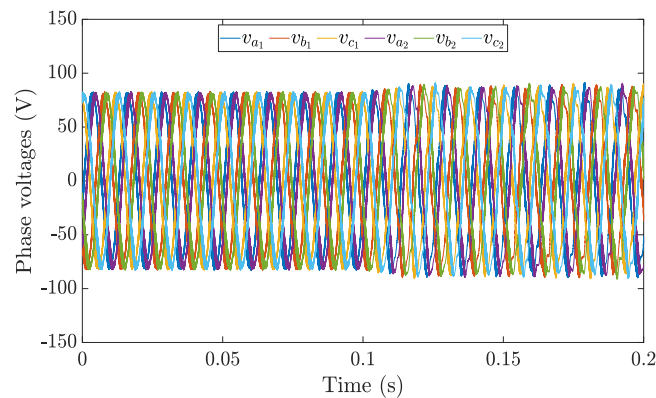
Symbol	Parameter	Value
$P_{L, rated}$	Rated power	150 kW
I_{dc}	dc-link current	250 A
T_{rated}	Rated torque	244 N.m.
ω_{rated}	Base speed	1200 rpm
P	Pair of poles	4
L_d	D-axis inductance	0.25 mH
L_q	Q-axis inductance	0.27 mH
Ψ_d	PM flux	0.0557 Wb
f_s	Switching frequency	10 kHz
C_f	Filtering capacitor	150 μ F



(a) Motor speed and developed torque.



(b) Motor phase currents



(c) Motor phase voltages

Figure 5.13 The results of the IPMSM simulation model under the proposed scheme and controlled by FOC. The motor runs at reference speed $N_r = 1200$ rpm and 244 N.m. loading torque. A step load of 22 N.m. is applied to run the S-CSI in Region II of the modulation.

5.5. Experimental Results

5.5.1. Experimental Setup

A scaled-down prototype is used for the experimental test, as illustrated in Figure 5.14 to verify the feasibility of the proposed modulation scheme. A six-phase S-CSI is implemented by six half-bridges SKM50GB12V IGBT modules connected to SKHI 22 A/B H4 gate drivers from Semikron. The reverse blocking is achieved by connecting each half-bridge to a DSEI2x31-06C diode module one diode to clamp each IGBT to the positive and negative rails. A LAUNCHXL-F28379D digital signal processor generates the firing signals. A six-phase IPMSM is used as the load in the experiment. The parameters of the motor are enlisted in Table 5.4. The motor in the experiments is operated at 350 rpm at different load torques to change the modulation index of the S-CSI. The loading is achieved by coupling the motor mechanically to a belt starter generator (BSG) from D&V Electronics (model: HT-250). The BSG also regulates the dc-supply by providing a battery emulator. The dc-link current is fixed at 4A, and the S-CSI controller determines the control of the output. Two cases are captured and compared in this context to validate the proposed scheme.

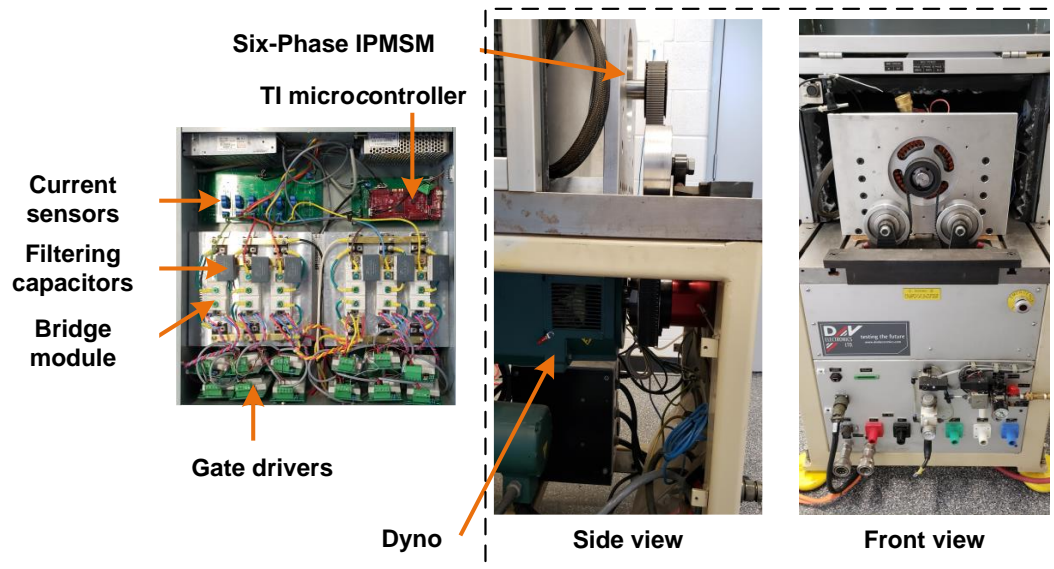


Figure 5.14 The experimental setup to test the proposed scheme.

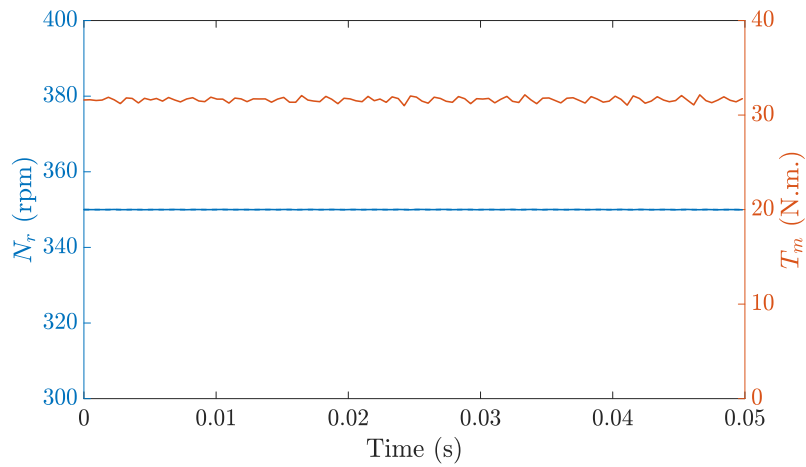
Table 5.4 Parameters of the motor load under the simulation study

Symbol	Parameter	Value
P_n	Rated power	3 kW
T_n	Rated torque	70 N.m.
ω_n	Rated speed	405 rpm
P	Pair of poles	17
R_s	Stator resistance	1.3 Ω
L_d	D-axis inductance	13.576 mH
L_q	Q-axis inductance	13.926 mH
L_{xy}	xy inductance	4.076 mH
ψ_d	PM flux	0.156 Wb
f_s	Switching frequency	10 kHz
C_f	Filtering capacitor	10 μ F

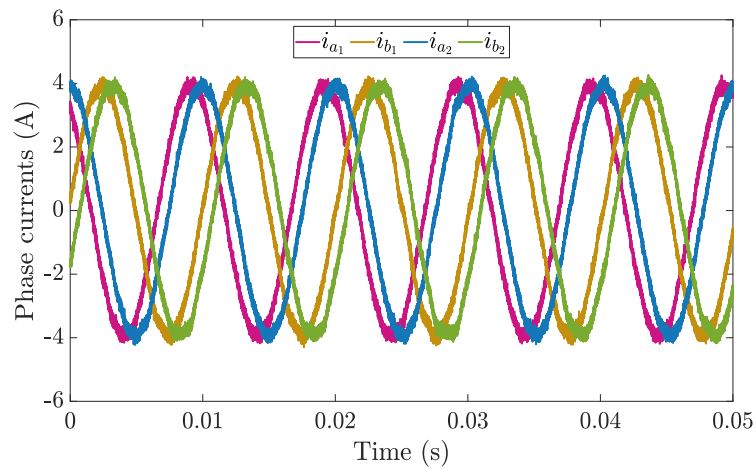
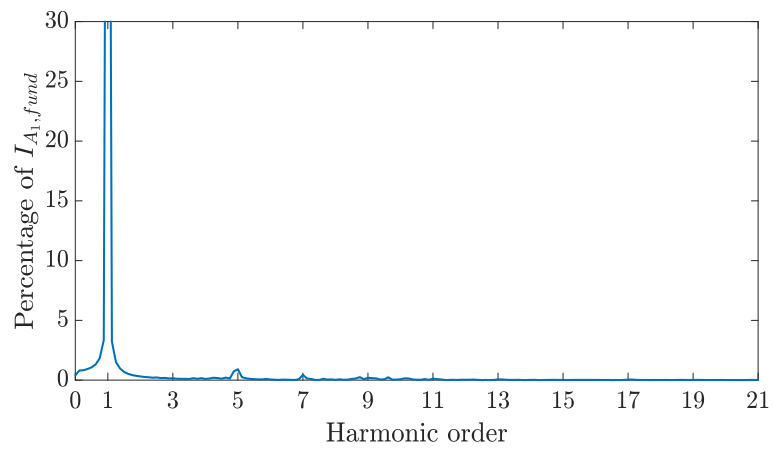
5.5.2. Experimental Results

The tests performed in this section include running the inverter at $m = 1$ and $m = 1.073$. The experimental results of running the setup at $m = 1$ are shown in Figure 5.15. This test shows the performance of the proposed scheme in Region I of the modulation. The waveforms shown are the load currents in Figure 5.15(a), where phase currents (a_1 , b_1 , a_2 , and b_2) appear on the 4-channel scope measured using hall-effect current sensors. The currents are sinusoidal, and the harmonic spectrum of i_{A_1} is shown in Figure 5.15(b) using the Fast Fourier Transform function in MATLAB. As expected, the spectrum shows low harmonic content as the operation is in Region I of the modulation. The load phase voltage is demonstrated in Figure 5.15(c) and its spectrum in Figure 5.15(d), which contains low harmonic content.

The results of the S-CSI running in Region II are illustrated in Figure 5.16. The waveforms of the output currents have a nearly flat-top shape because of the harmonic injection, as in Figure 5.16 (a). The cost of extending the modulation index appears in the harmonic spectrum of the load currents and voltages, as in Figure 5.16 (b). The 5th and 7th harmonics are higher than the injected values since the capacitor selected resonates with the load inductance in the xy subspace at the 8th harmonic ω , amplifying the 5th and 7th harmonics by a small factor as shown previously in Figure 5.16(c). However, the higher-order harmonics, such as the 17th and 19th harmonics, are diminished because of that capacitor selection. The load voltage is shown in Figure 5.16(d), and it can be noticed that the voltage harmonics are not significant to the fundamental voltage harmonic as in Figure 5.16(e).



(a) Machine speed and torque.

(b) Load phase currents (a_1 , b_1 , a_2 , and b_2)(c) Harmonic spectrum of the phase a_1 current.

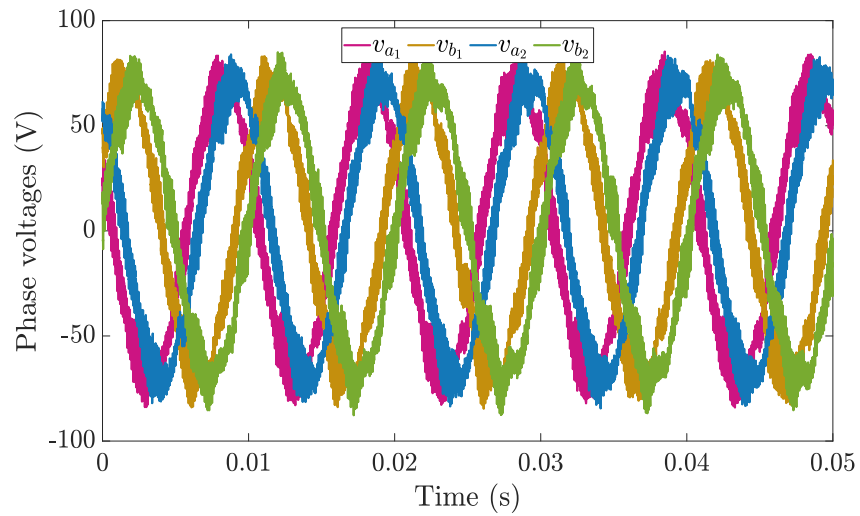
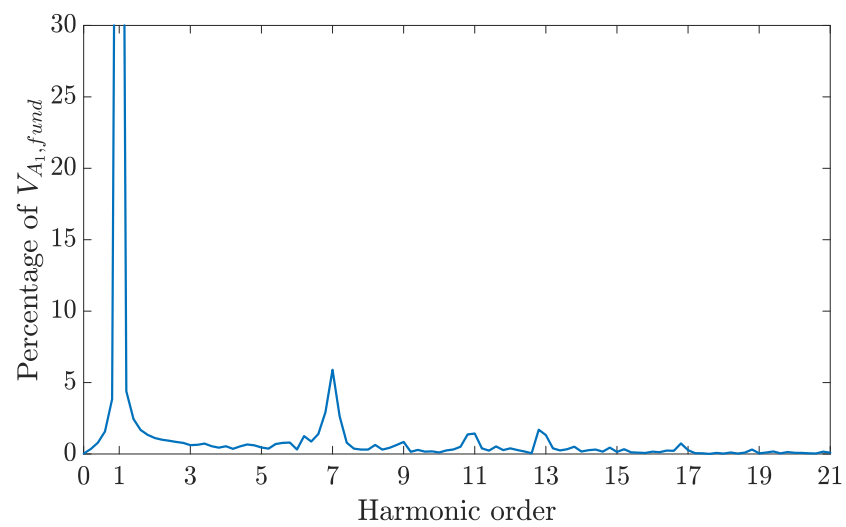
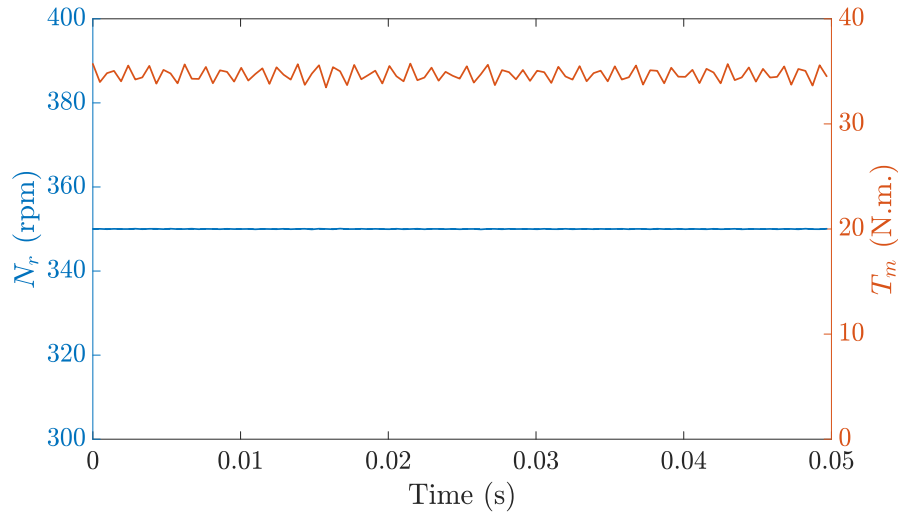
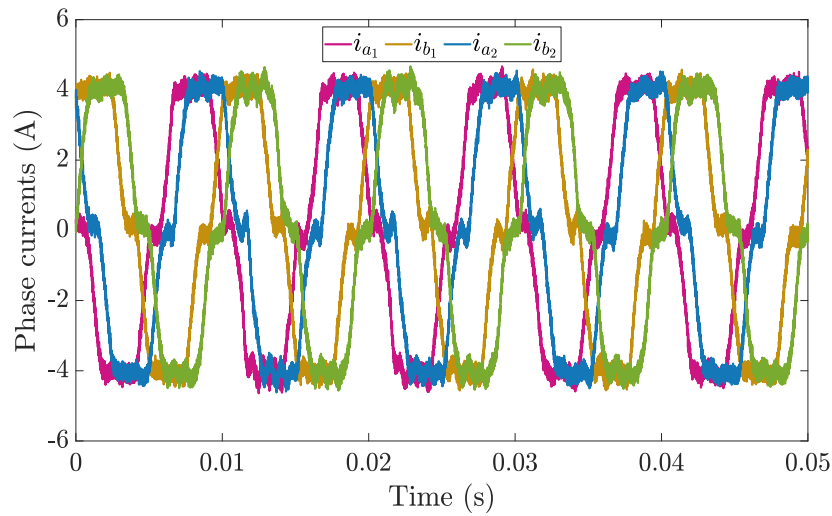
(d) Load phase voltages (a_1 , b_1 , a_2 , and b_2)(e) Harmonic spectrum of the phase a_1 voltage.

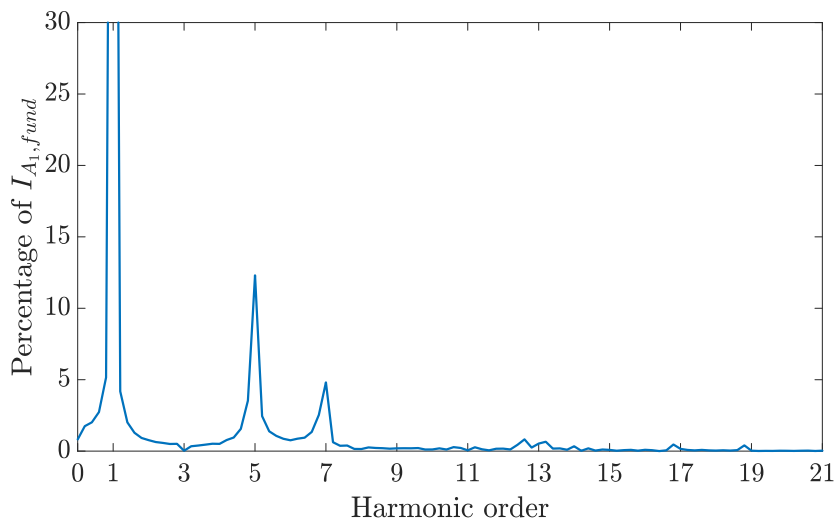
Figure 5.15 Experimental results of running the setup at $m = 1$ at $\omega = 350 \text{ rpm}$, $T = 31.6 \text{ N.m}$.



(a) Machine speed and torque.



(b) Load phase currents ($a_1, b_1, a_2,$ and b_2).



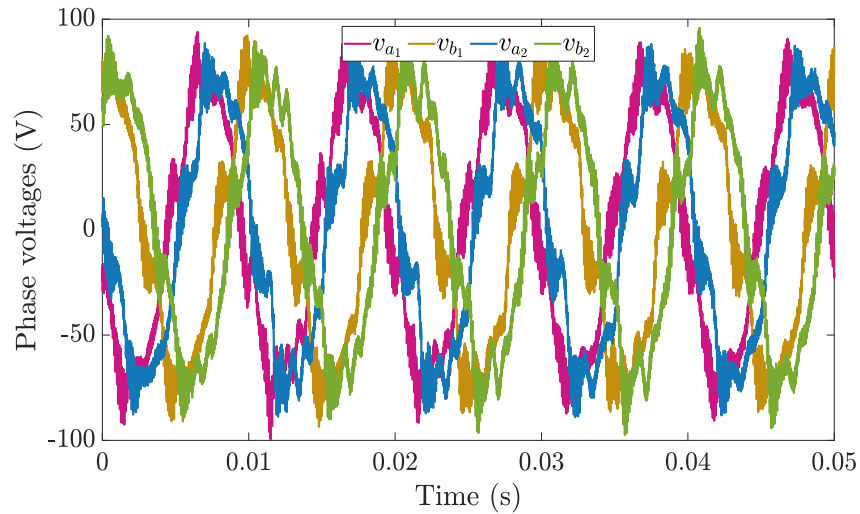
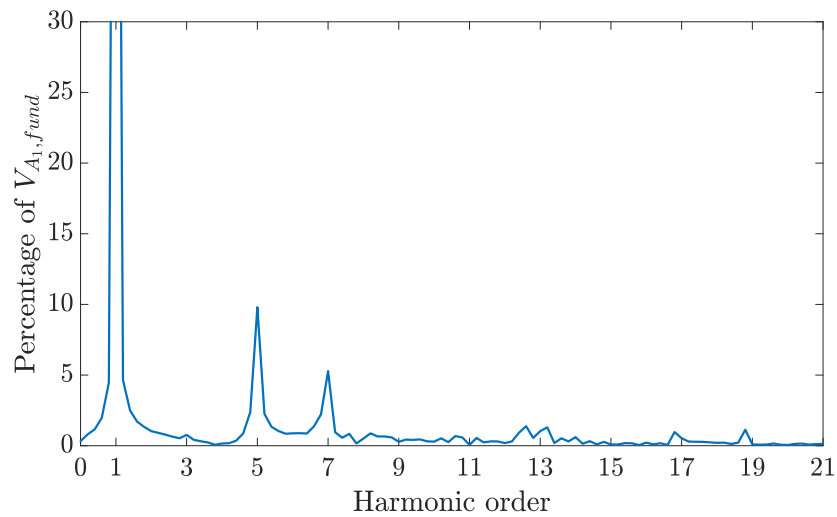
(c) Harmonic spectrum of the phase a_1 current.(d) Load phase voltages (a_1 , b_1 , a_2 , and b_2).(e) Harmonic spectrum of the phase a_1 voltage.

Figure 5.16 Experimental results of running the setup at $m = 1.0773$ at $\omega = 350 \text{ rpm}$, $T = 34.6 \text{ N.m}$.

MATLAB analyzes the harmonics of the currents and voltages to process the recorded data points of the waveforms. The formula for calculating the THD of the measured currents is defined in (5.18).

$$\text{THD} = \frac{1}{g_1} \sqrt{\sum_{l=2}^{25} (g_l)^2} \quad (5.18)$$

Where q_l is the harmonic of order l as $l \in \{2,3, \dots, 25\}$ and f_1 is the fundamental current component.

The THD of the currents and voltage waveforms are illustrated in Table 5.5. As it can be noticed, the $m = 1.073$ case has higher THD values compared to the $m = 1$ case due to the injected harmonics.

Table 5.5 THD Comparison between Region I and II

Modulation index	Variable	THD
$m = 1$	Load current	2.61 %
$m = 1.073$	Load current	16.2559 %

5.6. Summary

This chapter proposes an extension SVM technique of the dc-link utilization range. The SVM method is developed starting by studying the possible switching states of the S-CSI and then adopting the VSD method from VSI to CSI. The extension of the modulation range is achieved by pushing the inverter to work in the overmodulation region. Hence, a problem of extra harmonics in the xy subplane arises.

The chapter covers the optimization algorithm to minimize the injected harmonics while keeping them confined by the inverter working principles. The implementation employed LUT to accommodate for the computational burdens of current DSPs. The study covered the selection of

the filtering capacitors to avoid any resonance phenomenon in the system. Finally, the experimental results confirm the intended extension of modulation by approximately 8%, which reflects an increase in the motor torque production capability keeping the voltage and current THDs minimized.

Chapter 6

Proposed Modulation for Common-Mode-Voltage (CMV) Reduction of Standalone-CSI (S-CSI)

6.1. Introduction

Common-mode voltage is one of the hazardous issues accompanying ac drives operated by pulse-width-modulated (PWM) inverters. CMV is a serious design issue that, if not appropriately addressed, can lead to electromagnetic interference (EMI) [152]. Besides, inducing voltages across machine shaft and leakage currents in motor bearing result in damaging effects over time [153]. Another leakage current type is the grounding-type through the parasitic capacitances [154]. CMV could also damage the insulation of the motor windings risking the safety and stability of the entire drive [155]. Hence, several solutions have been introduced to eliminate or even reduce CMV. Reportedly, the peak of the CMV is associated with the shoot through-state in space vector modulation (SVM) of three-phase CSI [156, 157]. The two main approaches for mitigating the

CMV are adding extra circuitry or modifying the modulation scheme [158]. The compromise between the two approaches is to choose either the additional cost, packaging and thermal management of extra hardware versus the limited dc-link utilization or worse harmonic profile of the modified modulation schemes.

In the literature, the methods based on altering the modulation scheme are referred to as the nonzero-vector modulation (NZS) schemes [156] and zero-state vector selection methods [157]. One of the NZS schemes is the active zero-vector modulation (AZM), which replaces the traditional null states of the CSI with two active states in opposition. Another NZS method is called the near state modulation (NSM), which utilizes the nearest three active states to the reference vector to deploy the SVM scheme. The NZS methods suffer from limited modulation index and high harmonics content. The approaches introduced in [157] are based on the online selection of the zero-state with the minimum instantaneous CMV. The CMV is mitigated by adding extra hardware in [158]. The additions are power semiconductors and a snubber capacitor to provide a new method of implementing the null switching state. In five-phase CSI-based drives, the online selection method of the zero-state is applied [17] after analyzing the CMV associated with the possible switching states. However, to the authors' best knowledge, a solution for the six-phase S-CSI has not been addressed yet. Proposed SVM schemes are introduced in this context to reduce the CMV content for the S-CSI topology significantly. The key features that differentiate this work from previous proposals are:

- All the presented techniques are based on the vector space decomposition method, which considers the current harmonics in the subspaces that do not contribute to torque production, unlike in [13].

- The selection of the switching states is based on the analysis of the associated CMV with each state.
- There is no need for extra hardware or phase voltage measurements since all the states are preselected offline, unlike [17].
- All the presented methods are compared to the previously used ones regarding the dc-link utilization and load power factor variation.

6.2. Analysis of CMV Associated with the S-CSI Switching States

CMV is defined in VSI systems as the voltage between the load neutral point and the dc-link midpoint in $1N$ -configurations. It can be modified to another definition to suit the case of CSI-fed loads as in [17]. The CMV calculation becomes half the summation of the voltages between the dc rails and the load neutral point. The CMVs calculations for CSI_1 and CSI_2 are shown in (6.1):

$$\begin{cases} v_{cm_1} = \frac{1}{2}(v_{P_1n_1} + v_{N_1n_1}) \\ v_{cm_2} = \frac{1}{2}(v_{P_2n_2} + v_{N_2n_2}) \end{cases} \quad (6.1)$$

where $v_{P_1n_1}$, $v_{N_1n_1}$, $v_{P_2n_2}$, $v_{N_2n_2}$ are the voltages between the dc rails of each three-phase CSI and the neutral point of its load, as shown in Table 6.1. The total CMV calculation for the $2N$ -configuration case can be described as the average of v_{cm_1} and v_{cm_2} as in (6.2) to include both their effects [159].

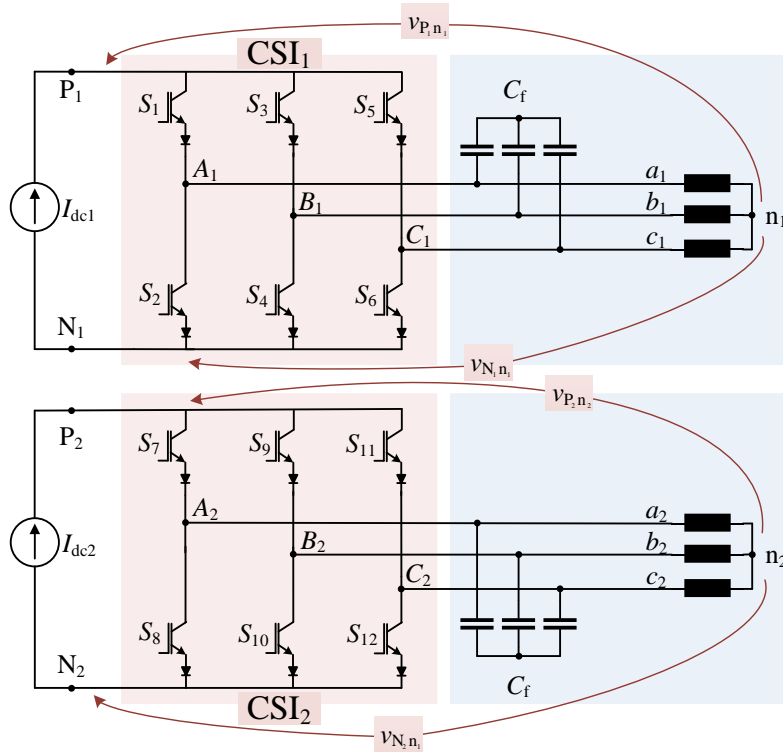


Figure 6.1 S-CSI configuration of asymmetrical six-phase motors.

$$v_{cm} = \frac{1}{2}(v_{cm_1} + v_{cm_2}) \quad (6.2)$$

Defining the voltages $v_{P_1n_1}$, $v_{N_1n_1}$, $v_{P_2n_2}$, $v_{N_2n_2}$ as functions of the switching states S_j is a step to calculate the CMV. For instance, in CSI1, the voltages $v_{P_1n_1}$, $v_{N_1n_1}$ are equal to the voltages of the phases activated by the selected switching state (6.3).

$$\begin{cases} v_{P_1n_1} = S_1v_{a_1n_1} + S_3v_{b_1n_1} + S_5v_{c_1n_1} \\ v_{N_1n_1} = S_2v_{a_1n_1} + S_4v_{b_1n_1} + S_6v_{c_1n_1} \end{cases} \quad (6.3)$$

where S_k denotes the state of a semiconductor switch and k is a counter which is equal to odd numbers $\{1,3,5\}$ for upper switches and even numbers $\{2,4,6\}$ for lower switches, $v_{a_1n_1}, v_{b_1n_1}, v_{c_1n_1}$ are the output phase voltages of CSI₁ with respect to the neutral point n_1 .

The set of voltages $v_{P_2n_2}, v_{N_2n_2}$ for CSI₂ can be easily deduced in the same manner by relying on the switches of CSI₂. The deduced CMV relation of S-CSI based on the previous discussion can be found by substituting all the voltages from (6.3) in (6.2) to get (6.4):

$$v_{cm} = \frac{1}{4} \begin{bmatrix} v_{a_1n_1} \\ v_{b_1n_1} \\ v_{c_1n_1} \\ v_{a_2n_2} \\ v_{b_2n_2} \\ v_{c_2n_2} \end{bmatrix}^T \begin{bmatrix} S_1 + S_2 \\ S_3 + S_4 \\ S_5 + S_6 \\ S_7 + S_8 \\ S_9 + S_{10} \\ S_{11} + S_{12} \end{bmatrix} \quad (6.4)$$

It is assumed in this context that the output phase voltages are sinusoidal, as shown in (6.5):

$$[v_{ph}] = \begin{bmatrix} v_{a_1n_1} \\ v_{b_1n_1} \\ v_{c_1n_1} \\ v_{a_2n_2} \\ v_{b_2n_2} \\ v_{c_2n_2} \end{bmatrix} = |v_{ph}| \begin{bmatrix} \cos(\theta + \phi) \\ \cos(\theta - 120^\circ + \phi) \\ \cos(\theta - 240^\circ + \phi) \\ \cos(\theta - 30^\circ + \phi) \\ \cos(\theta - 150^\circ + \phi) \\ \cos(\theta - 270^\circ + \phi) \end{bmatrix} \quad (6.5)$$

where $[v_{ph}]$ is the phase voltage vector, $|v_{ph}|$ is the magnitude of the phase voltages, $\theta = \omega t$ is the angle of rotation of electrical references, ω is the electrical angular velocity, and ϕ is the load power factor angle.

Consequently, the selection of the switching states is substantial to determine which combination of voltages appears in the CMV. The portion that appears from the resultant waveform as the actual CMV is dependent on the angle ϕ . Thus, a subsection is dedicated to

studying that effect in detail later in the chapter. The analysis of all the possible switching states results in various voltage magnitudes of the CMV that can be summarized as shown in Table 6.1. For clarification, the following example demonstrates the variable outcomes of the CMV. The cases chosen are based on selecting different null vectors, such as I_{11} or I_{15} . The comparison between both states is based on the expected waveforms of the combined voltages based on (6.4) that appear as the CMV if either state is selected. By assuming two sets of three-phase voltages shifted by 30° , The resultant total CMV of the S-CSI in case of applying I_{11} , and I_{15} states are illustrated in Figure 6.2.

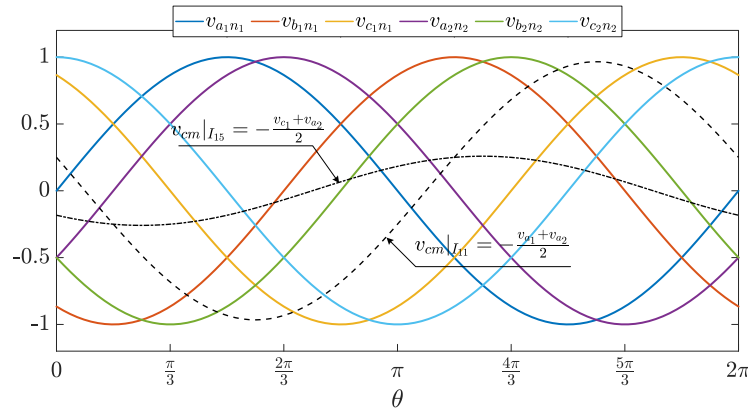


Figure 6.2 Phasor diagram showing the possible outcomes of the resultant CMV of the selected group of switching states in the example.

The switching state I_{15} results in the summation of phases a_1 and c_2 to appear as the resultant CMV ($v_{cm}|_{I_{15}}$) which has a lower magnitude compared to the CMV ($v_{cm}|_{I_{11}}$) associated with state I_{11} . Even though S-CSI has no switching states that would eliminate the CMV, several possible selections can be made based on Table 6.1 to reduce the total CMV, as shown in the next section.

Table 6.1 Classification of the states of S-CSI based on the resultant magnitude of CMV

Categories of $ v_{cm} $ (Sorted ascendingly)			Switching states	
	$ v_{cm} / v_{ph} $		State	Group
	Expression	value		
V_1	$0.25\sqrt{(2-\sqrt{3})}$	0.1294	(9-26-43-68-55-75)	I_L
			(5-19-39-62-72-79)	I_S
V_2	$0.5\sqrt{(2-\sqrt{3})}$	0.2588	(15-29-49)	I_0
V_3	$0.5\sqrt{\left(\frac{5}{4}-\frac{\sqrt{3}}{2}\right)}$	0.3098	(4-14-18-24-28-35-38-48-52-60-67-74)	I_{M2}
V_4	$0.25\sqrt{2}$	0.3536	(3-7-23-27-37-44-59-63-66-70-73-80)	I_{M1}
V_5	$0.25\sqrt{(2+\sqrt{3})}$	0.483	(1-21-41-61-71-81)	I_L
			(8-25-45-57-64-77)	I_S
V_6	$0.25\sqrt{5}$	0.559	(6-10-17-20-30-34-40-50-54-56-69-76)	I_{M2}
V_7	$1/\sqrt{2}$	0.707	(13-33-47)	I_0
V_8	$0.5\sqrt{\left(\frac{5}{4}+\frac{\sqrt{3}}{2}\right)}$	0.7273	(2-12-16-22-32-36-42-46-53-58-65-78)	I_{M2}
V_9	$0.5\sqrt{(2+\sqrt{3})}$	0.9659	(11-31-51)	I_0

6.3. Proposed SVM Schemes for Common-Mode Reduction (CMR)

The SVM schemes proposed in this context are based on the VSD method to achieve two goals. Firstly, the reduction of the CMV regardless of the load power factor. Secondly, to linearly control the S-CSI and mitigate the losses harmonics in the xy subspace. One of the main benefits of the proposal is the offline selection of the switching states, unlike the method in [17] for the CMV reduction of five-phase systems. The previous method needs to measure the output voltages to determine online which zero-vector to be applied to make the lowest line voltage in magnitude appear as the CMV. Based on the CMV analysis of S-CSI, there is a possibility to devise SVM schemes depending on states with low CMV peaks associated regardless of the load power factor. Three proposed common-mode reduction (CMR) SVM-based schemes are discussed in the following subsections. Firstly, the application of the VSD method to the SVM schemes is presented. Then, the selection of the switching states in each proposed scheme is illustrated, accompanied by the optimum switching patterns.

6.3.1. VSD-Based SVM

In a six-phase S-CSI, there are four reference components of the output current $(i_r^\alpha, i_r^\beta, i_r^x, i_r^y)$ to be realized. The selected modulation of the S-CSI in this context is based on a five-segment discontinuous SVM. In each time sample T_s , four active switching states are selected based on the position of the current reference in the $\alpha\beta$ subspace. Selecting four active states per sector is necessary to control the available four degrees of freedom in six-phase loads connected in a $2N$ -configuration. Besides, one null switching state is selected to achieve the Ampere-second balance between the realizable inverter output and the desired references per T_s . The discontinuous

SVM is often used to minimize the switching transitions between states, hence minimizing the switching losses of the S-CSI.

The Ampere-second balance in six-phase inverters must be achieved for all the decoupling axes for proper operation of S-CSI. Since there are four degrees of freedom, the four selected current vectors must be synthesized to the $\alpha\beta$ and xy subspaces. The synthesized components are named as I_g^γ where $\gamma \in \alpha, \beta, x, y$ denotes the different decoupled axes, and subscript g refers to the order of the selected active switching state per sector. The dwell times related to the selected active states are defined in this context as t_g , meanwhile, the null time is named t_0 . Equation (5.3) describes the calculation of the dwell times of the S-CSI, which depends on the components of the selected states per sector as in matrix C . To derive the references in (5.3), the phase current references $[i_r^{inv}]$ in the original six-phase frame are assumed as in (6.6).

$$[i_r^{inv}] = M I_{dc} \begin{bmatrix} \cos(\theta) \\ \cos(\theta - 120^\circ) \\ \cos(\theta - 240^\circ) \\ \cos(\theta - 30^\circ) \\ \cos(\theta - 150^\circ) \\ \cos(\theta - 270^\circ) \end{bmatrix} \quad (6.6)$$

where M is the modulation index which is the ratio between the maximum of the fundamental harmonic of the output inverter currents $|i_{f_1, max}^{inv}|$ and the dc-link current I_{dc} .

The calculation of the reference currents in the decoupled subspaces is shown in (6.7):

$$\begin{bmatrix} i_r^\alpha \\ i_r^\beta \\ i_r^x \\ i_r^y \end{bmatrix} = [T_{VSD}] \cdot [i_r^{inv}] = \sqrt{3} M I_{dc} \begin{bmatrix} \cos(\theta) \\ \sin(\theta) \\ 0 \\ 0 \end{bmatrix} \quad (6.7)$$

The xy have no contribution to the torque production process, as mentioned in previous sections. Henceforth, for the sake of minimizing the system losses, the values of components i_r^x, i_r^y are controlled to be zero, as shown in (6.7), to achieve sinusoidal output currents.

6.3.2. Proposed and Adopted CMR-SVM Methods

The selection of the switching states to execute the SVM scheme is the main difference between all the schemes. The four active states are selected based on the following criteria in the proposed schemes. The first criterion is to choose states from categories that minimize the CMV content. Secondly, the selected states should be selected to maximize the utilization of the dc-link current. Hence the vectors with the largest magnitude possible in the $\alpha\beta$ subspace are prioritized. Lastly, the selected vectors should achieve zero-average current components in the xy subspace for harmonic-free phase currents. From Table 6.1, the states from the I_L group with the largest current magnitude in the $\alpha\beta$ subspace that result in the lowest magnitude of CMV is in the category V_1 . As for the null states, the category V_2 contains the null state that results in the lowest CMV magnitude compared to the other allowable null states. The available vectors from I_L group in V_1 category and V_2 null vectors are not sufficient to implement a five-segment SVM scheme. Thus, the proposed schemes utilize V_1 and V_2 vectors plus vectors from the other groups considering minimizing CMV peak and RMS values while maximizing dc-link current utilization. The three schemes presented in this work are named CMR-SVM 1, 2, and 3, where the first one introduces a novel combination of the selected vectors per sector. Meanwhile, the second and third schemes represent the adoption of the discussed methods for VSIs.

5.3.2.1. CMR-SVM 1

Following the criteria for modulation, the switching states in CMR-SVM 1 are selected from the CMV categories V_1 and V_2 . The two categories contain states that result in the current components of groups I_L , I_S and I_0 . A complete cycle of modulating the reference currents in the $\alpha\beta$ subspace is represented by twelve sectors in this scheme. In each sector, two active vectors are chosen from I_L group and the other two from I_S as in Figure 6.3. The two large vectors are selected so that the sector would lie between them. Meanwhile, the two small vectors are selected so that the first is inside the sector and the other one is the nearest small vector to the sector. The nearest vector is the lagging one in odd sectors and the leading one in even sectors.

This selection is based on studying the several possible combinations of the selected vectors and testing them using the dwell time calculation in (5.3) so that the inverse of the components-matrix C would exist. This SVM scheme produces the low CMV content in the S-CSI topology while mitigating the xy harmonic currents by setting the reference currents in (5.3) equal to zero. The utilization of the dc-link is expected to have limitations since some of the states are from the I_S group.

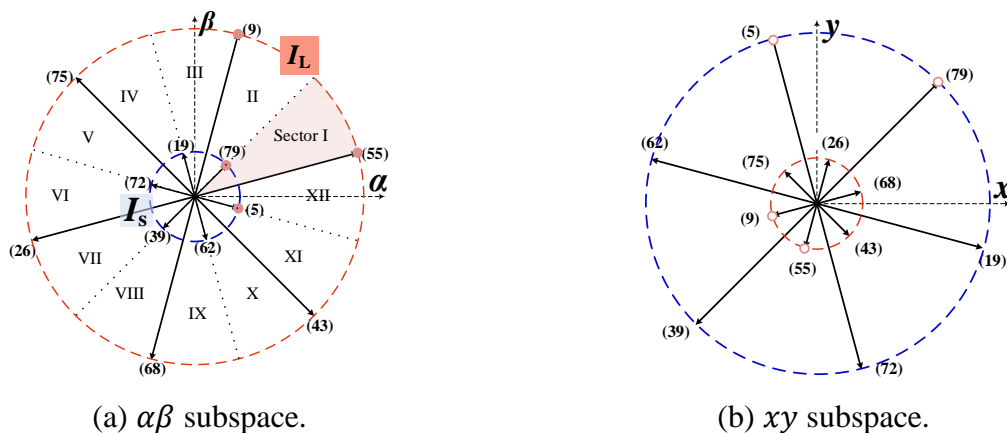


Figure 6.3 The selected vectors for CMR-SVM 1.

5.3.2.2. CMR-SVM 2

In this scheme, two states per sector are selected from the group I_{M1} in V_4 category in addition to the states from I_L group in V_1 category and null states from V_2 category to achieve higher dc-link utilization. The cost of such selection is the higher expected CMV compared to CMR-SVM 1. The CMR-SVM 2 is based on dividing the complete modulation cycle into six sectors, as shown in Figure 6.4. The beginning of the sector is marked by two vectors, one from the I_L group and the other one is from the I_{M1} group. The two other vectors, one from each group, mark the end of the sector. The mitigation of the xy is ensured since the vectors from the large and medium groups result in opposing vectors in the xy subspace as in Figure 6.4(b).

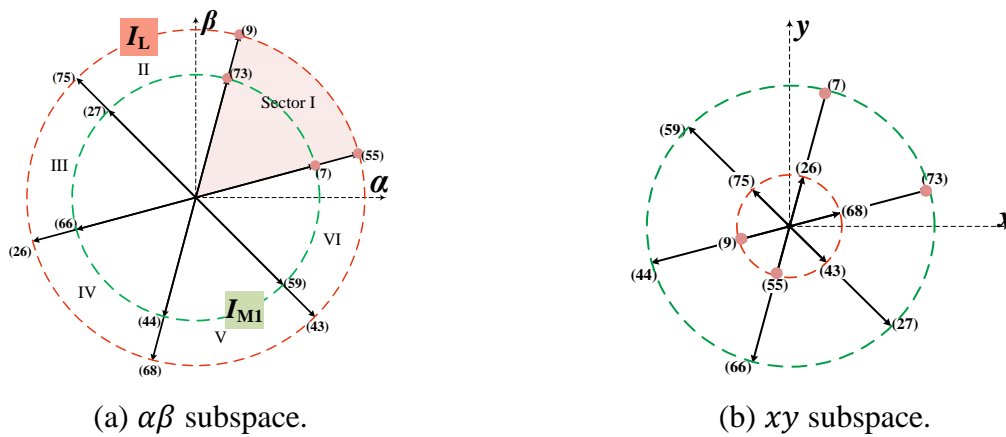


Figure 6.4 The selected vectors for CMR-SVM 2.

5.3.2.3. CMR-SVM 3

This scheme aims to maximize the modulation index of the S-CSI furthermore. It is clear that the vectors from the group I_L are the best candidates to achieve the highest realizable modulation index. In terms of CMV magnitude, the I_L group vectors distributed as six vectors in V_1 category, and the rest are in the V_5 category. However, selecting states from the V_5 category results in higher CMV magnitudes compared to the previous two SVM schemes. The mapping of all the vectors used in this scheme in both the $\alpha\beta$ and xy subspaces is shown in Figure 6.5. There

are twelve sectors in this scheme, like CMR-SVM 1. The selected vectors per sector are identified as follows. The sector starts and ends with one vector, and the other two are adjacent vectors from both sides.

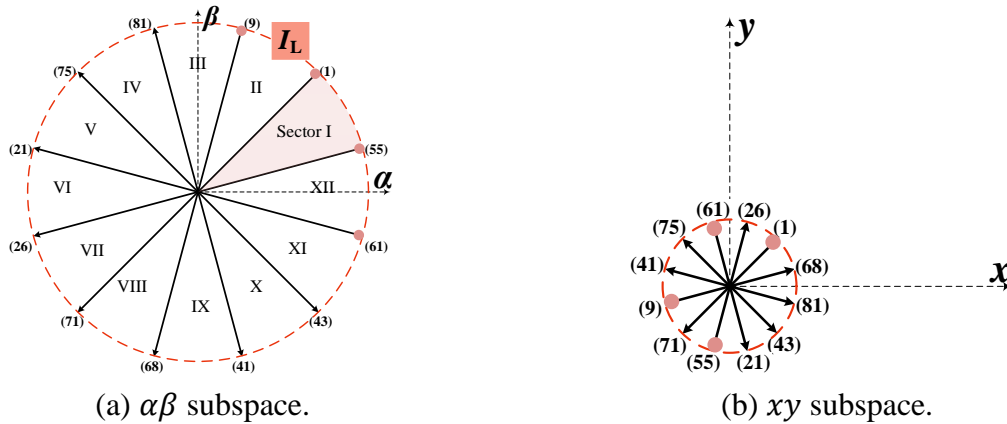


Figure 6.5 The selected vectors for CMR-SVM 3.

6.3.3. Optimum Switching Patterns

The losses of the converter operation can be classified based on their cause of conduction and switching losses. The calculations of the switching losses have been mentioned in many works [13, 17, 22]. All the references use a simplified approach using the energy dissipated at the ON transition E_{ON} and at the OFF transition E_{OFF} , which can be obtained from the datasheet of the power semiconductor used in the converter. Undoubtedly, the higher the switching transition events, the higher the switching losses. Hence, it is vital to reduce the number of these events to reduce the switching losses and improve the converter efficiency. The selected vectors per sector can be applied in many sequences that result in patterns with different numbers of switching transitions. The order in which the vectors should be applied is the key to minimizing the transition events. A method for calculating the number of transitions has been used in [160]. A function

called space vector distance function SVDF calculates the number of transitions by subtracting the switching state of one vector and the following one regarding the ON state as $S = 1$ and the OFF state as $S = 0$. Only the absolute value of the subtraction process is considered because the target is registering the transition regardless of the sign. The transition calculation is described in (6.8), and the algorithm for choosing the optimum pattern for a specific sector of an SVM scheme is shown in Figure 6.6.

$$\text{SVDF} = \sum_{k=1}^{12} |S_k^{pre} - S_k^{next}| \quad (6.8)$$

Where the superscript *pre* and *next* refer to the previous and following switching states to be applied in the pattern.

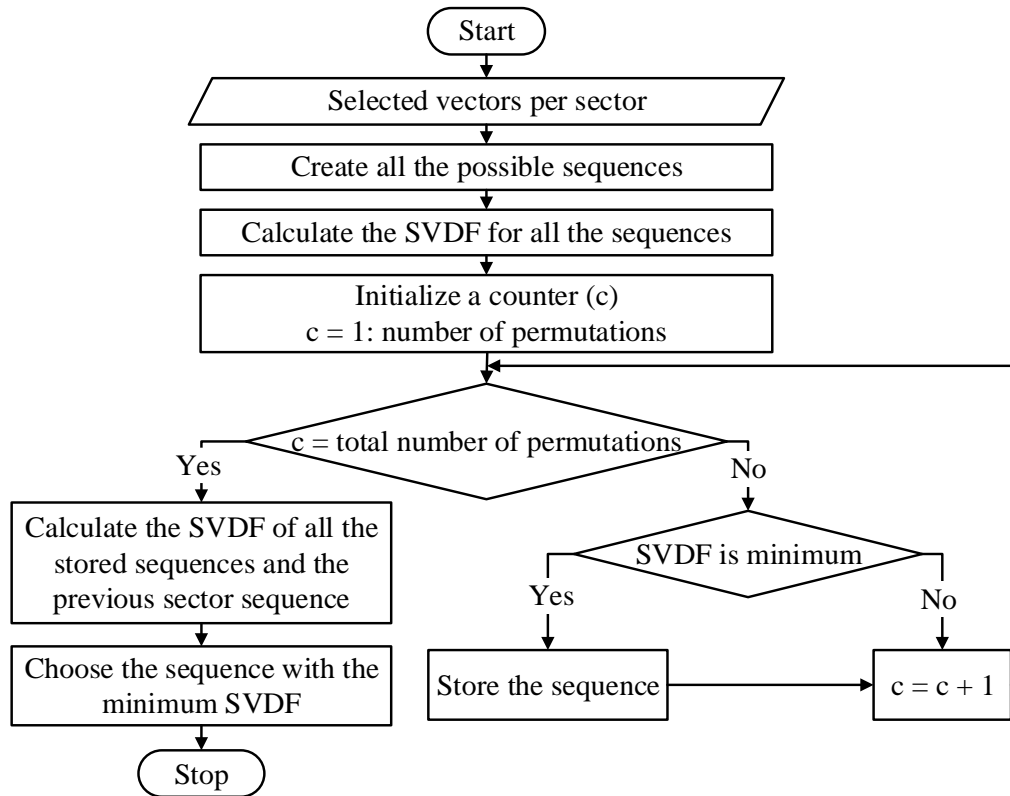


Figure 6.6 Flowchart of the optimum sequence selection algorithm.

The algorithm is built on finding the permutation leading to minimum SVDF calculation. The algorithm's results in each proposed scheme are shown in Table 6.2, Table 6.3, and Table 6.4 for CMR-SVM 1, CMR-SVM 2, and CMR-SVM 3, respectively. The tables show the selected sequence of switching states in all the sectors with the number of transitions. The CMR SVM 1 has the minimum number among the three proposed schemes with ten transitions compared to 16 in the other cases. An example of the transitions per switch of the S-CSI is shown in Figure 6.7, presenting sector I of all the proposed schemes. As can be seen, the patterns are of the five-segment type, and the transitions happen at the calculated dwell times compared with a saw tooth carrier.

Table 6.2 The Sequence of Switching States of The CMR-SVM 1 Scheme

Sector	Switching State					Number of transitions
I	15	55	9	5	79	16
II	15	9	55	19	79	
III	15	9	75	79	19	
IV	15	19	72	9	75	
V	15	72	19	26	75	
VI	15	26	75	39	72	
VII	15	26	68	72	39	
VIII	15	68	26	62	39	
IX	15	68	43	39	62	
X	15	62	5	68	43	
XI	15	5	62	55	43	
XII	15	55	43	79	5	

Table 6.3 The Sequence of Switching States of the CMR-SVM 2 Scheme

Sector	Switching State					Number of transitions
I	15	55	9	7	73	16
II	15	9	75	73	27	
III	15	26	75	27	66	
IV	15	26	68	66	44	
V	15	68	43	44	59	
VI	15	55	43	59	7	

Table 6.4 The Sequence of Switching States of the CMR-SVM 3 Scheme

Sector	Switching State					Number of transitions
I	15	9	1	55	61	10
II	15	55	1	9	81	
III	15	1	9	18	75	
IV	15	9	81	75	21	
V	15	26	21	75	81	
VI	15	71	26	21	75	
VII	15	68	71	26	21	
VIII	15	26	71	68	41	
IX	15	71	68	41	43	
X	15	68	41	43	61	
XI	15	55	61	43	41	
XII	15	1	55	61	43	

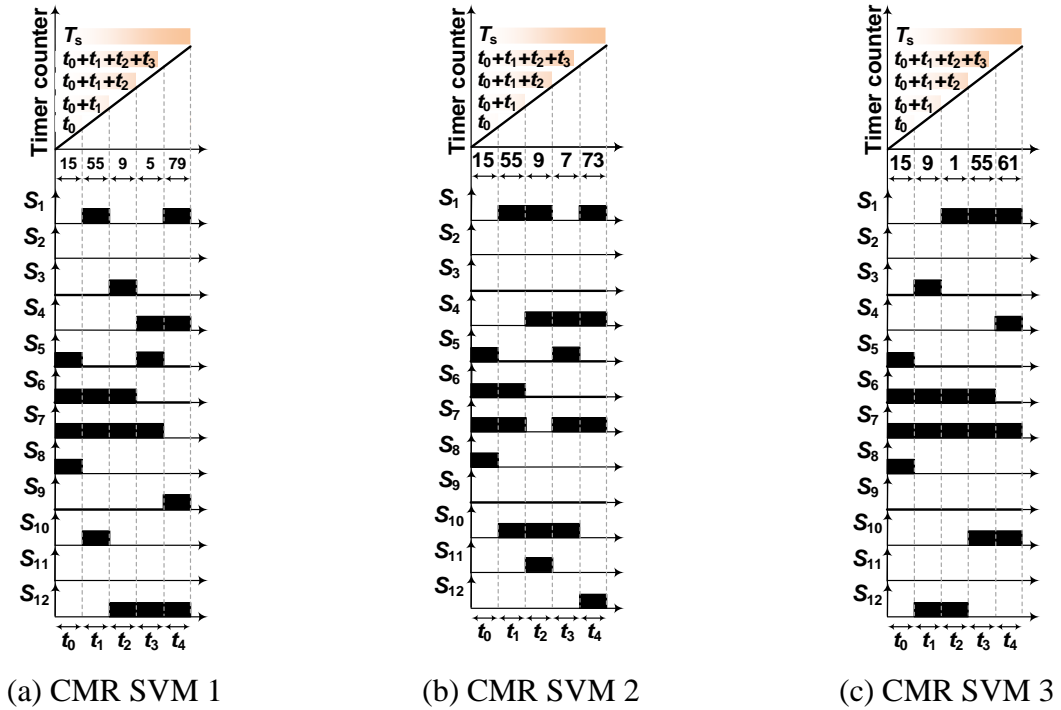


Figure 6.7 Optimum sequence for the switching states of the proposed schemes in sector I.

6.4. Evaluation of the Proposed SVM Schemes

The discussion in this section includes the utilization of the dc-link current calculated and compared among the proposed schemes. Besides, the RMS calculation of the CMV versus the modulation index and load power factor is performed to assess the schemes and estimate the reduction.

6.4.1. Maximum Modulation Index

The maximum modulation index M_{max} of all the schemes can be calculated as follows. The null zero vector is applied in pulse width modulation to follow the references and balance the Ampere-second equations. The null time t_0 decreases to the minimum possible value at the realizable M_{max} . In each scheme, the equation $t_0(\theta, M)$ can be derived as a step to get M_{max} . The value of M_{max} can be calculated from the t_0 equation at the angle θ that minimizes t_0 to be as minimum as possible, which is zero. By evaluating the matrix C in (5.3) using the components of the selected vectors in each SVM scheme in sector I, the t_0 equation can be derived. The null time calculations are described in (6.9) for CMR-SVM 1, (6.10) for CMR-SVM 2, and (6.11) for CMR-SVM 3.

$$t_{0,Sec I}^{SVM1} = (-0.93M \cos(\theta) - 0.75M \sin(\theta) + 1)T_s \quad (6.9)$$

$$t_{0,Sec I}^{SVM2} = (-0.789M \cos(\theta) - 0.789M \sin(\theta) + 1)T_s \quad (6.10)$$

$$t_{0,Sec I}^{SVM3} = (-0.866M \cos(\theta) - 0.5M \sin(\theta) + 1)T_s \quad (6.11)$$

The angle θ that minimizes $t_{0,sec I}$ can be obtained by partial differentiation of each equation of $t_{0,sec I}$ with respect to the angle θ . Then, $t_{0,sec I}$ is minimum (i.e., equal to zero) at the angle θ when the differential term of $t_{0,sec I}$ with respect to θ is equal to zero. Therefore, the modulation index is at its maximum value at that angle. The calculated angles to get $t_{0,sec I} = 0$ and $M = M_{max}$ are enlisted in Table 6.5 along with the maximum modulation indexes of the proposed SVM. As it can be noticed, the modulation index limits increase with using vectors from the larger magnitudes. For CMR-SVM 1 and 2, the dc-link current must be adjusted to higher values to obtain

the full power of the S-CSI as in CMR-SVM 3. The percentage increase of I_{dc} to achieve the full power using CMR-SVM 1 is 19.72%; meanwhile, it is 11.52% using CMR-SVM 2.

Table 6.5 Summary of the calculations of the maximum modulation index associated with the proposed SVM schemes

SVM Scheme	$\theta _{m_{max}}$	M_{max}
CMR-SVM 1	38.8°	0.8353
CMR-SVM 2	45°	0.8967
CMR-SVM 3	30°	1

This increase in I_{dc} certainly increases the losses of the S-CSI at the cost of reducing the CMV magnitude. This point is discussed in more detail in the comparison at the end of this section. Besides, power semiconductors with higher ratings must be selected with CMR-SVM 1 and 2 to withstand the current stresses.

6.4.2. Estimated CMV RMS versus Modulation Index m and Load Power Factor

As mentioned earlier in the CMV analysis, the load power factor affects the peak value of the total CMV. The voltage combinations that appear as the CMV are chosen to be as minimum as possible. However, the proposed schemes are based on the selection in an offline fashion. Hence, the portion of the sinusoidal waveform of those voltage combinations is not guaranteed to be minimal since it can vary from zero to the peak value. The load power factor is responsible in that case for the appearing peak and RMS values of the CMV. Equation (6.12) describes the calculation of the RMS value of the CMV.

$$v_{cm,rms} = \sqrt{\frac{1}{2\pi} \int_{\theta_o}^{2\pi+\theta_o} (v_{cm}(\theta))^2 d\theta} \quad (6.12)$$

The comparison between the proposed scheme is conducted by varying the power factor from one to 0.5, a typical range for motor drives, and the modulation index. The assumption is that the output phase voltages are sinusoids as in (6.5), and the modulation indexes are normalized by adjusting the dc-link currents, accordingly, as calculated in the previous subsection. The results of the CMV calculation are shown in Figure 6.8.

The CMV values are normalized to the phase voltage, and the proposed schemes are compared to the traditional vector classification technique used in [17]. The proposed schemes achieve low levels of the CMV across the full range of the modulation index and the load power factor. The minimum RMS values of the CMV can be achieved in the CMR SVM 1 scheme, while the highest CMV is associated with the VCT scheme adopted in [13] since the zero-states in this scheme are not selected based on the CMV analysis illustrated in this context. It is worth mentioning that the CMR-SVM 2 produces high CMV content compared to the other proposed techniques at high power factors ($PF = \cos(\phi)$) close to 1 over all the range of the modulation index. This remark is highlighted more in the experimental results section.

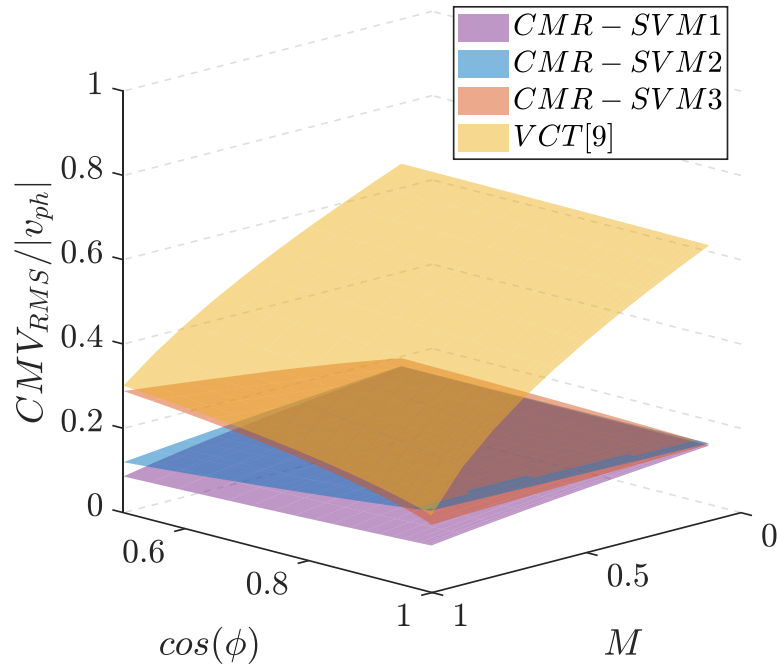


Figure 6.8 The normalized CMV_{RMS} vs. the modulation index and the load power factor using different modulation schemes for S-CSI.

6.5. Experimental Results

6.5.1. Experimental Setup

A scaled-down prototype is used for the experimental test, as illustrated in Figure 6.9, to verify the feasibility of the proposed modulation scheme. A six-phase S-CSI is implemented by six half-bridges SKM50GB12V IGBT modules connected to SKHI 22 A/B H4 gate drivers from Semikron. The reverse blocking is achieved by connecting each half-bridge to a DSEI2x31-06C diode module one diode to clamp each IGBT to the positive and negative rails. A LAUNCHXL-F28379D digital signal processor generates the firing signals. A six-phase IPMSM is used as the load in the experiment. The parameters of the motor are enlisted in Table 6.6. The motor in the

experiments is operated at 350 rpm at different load torques to change the modulation index of the S-CSI. The loading is achieved by coupling the motor mechanically to a belt starter generator (BSG) from D&V Electronics (model: HT-250). The BSG also regulates the dc-supply by utilizing the battery emulator feature. The dc-link current is fixed at 4A, 4.79A, 4.461, and 4A using VCT, CMR-SVM1, CMR-SVM2, and CMR-SVM3, respectively. The current values are selected to compensate for the limitations of the dc-link utilization under the different SVM schemes. Hence, the same output power is achieved to make an impartial comparison between all the schemes. The motor is loaded to work at the maximum modulation index under the modulation schemes.

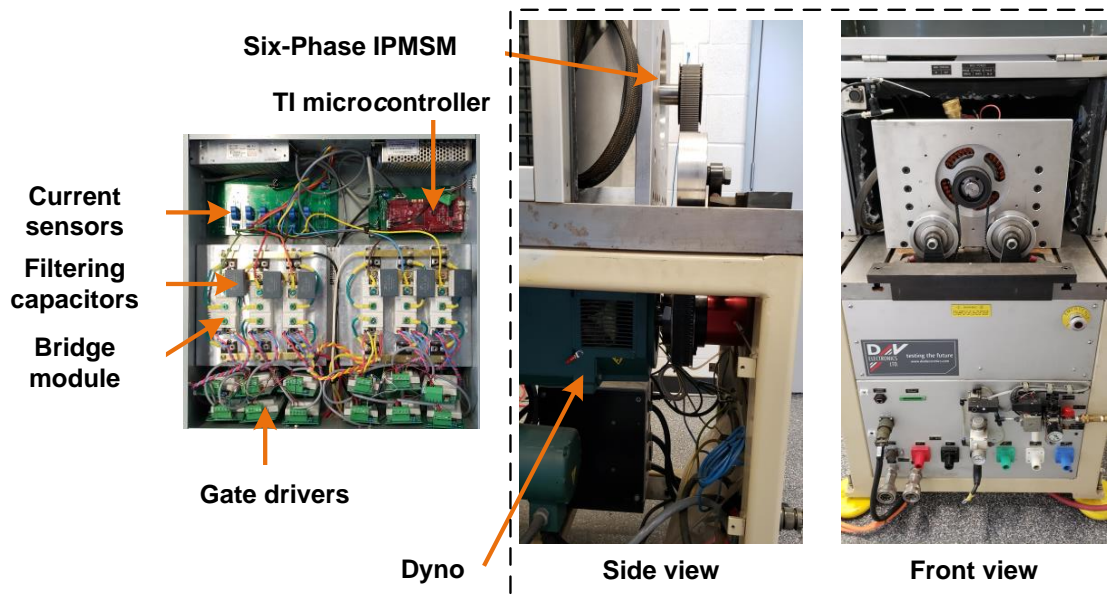


Figure 6.9 The experimental setup to test the proposed scheme.

Table 6.6 Parameters of the motor load under the simulation study

Symbol	Parameter	Value
P_n	Rated power	3 kW
T_n	Rated torque	70 N.m.
ω_n	Rated speed	405 rpm
P	Pair of poles	17
R_s	Stator resistance	1.3 Ω
L_d	D-axis inductance	13.576 mH
L_q	Q-axis inductance	13.926 mH
L_{xy}	xy inductance	4.076 mH
ψ_d	PM flux	0.156 Wb
f_s	Switching frequency	10 kHz
C_f	Filtering capacitor	10 μ F

6.5.2. Experimental Results

The results are recorded using an oscilloscope with current and voltage sensors and plotted using MATLAB. The mechanical outputs (speed and torque) are shown in Figure 6.10, running under the four schemes. The figures show that the same speed and torque (350 rpm, 31.6 N.m.) are achieved under all the schemes. Regarding the torque ripples, the CMR-SVM3 achieves the best performance since the ripples, in this case, are the lowest compared to the other schemes. Motor phase currents (A_1 , B_1 , A_2 , C_2) are illustrated in Figure 6.11, showing the correct phase shift between the phases. The RMS value of phase currents in all the cases is 2.83A. It can be noticed that the currents in (a), (b), and (d) are not pure sinusoids, unlike the ones in case (c), which is associated with the CMR-SVM3. The harmonic analysis of the motor phase currents is given in Figure 6.12. The analysis shows that xy harmonics, like the fifth and seventh harmonics, have noticeable magnitudes in the case of CMR-SVM 1 and 2 despite applying the zero-average xy currents strategy. The main reason is that the applied vectors from the small and medium groups

have large components in the xy subspace. Besides, dividing the cycle into six sectors of modulation degrades the reference tracking quality even more.

The current harmonics are reflected in the voltage waveforms in Figure 6.13. The best voltage waveforms are associated with the CMR-SVM3. The harmonic analysis confirms that the least harmonic content is achieved in the CMR-SVM3 case, as illustrated in Figure 6.14. The voltage waveforms are crucial in the CMV analysis since an assumption introduced in the earlier section is based on the phase and line voltages to be purely sinusoidal. The existence of harmonics in the voltage waveforms manipulates the CMV content because the peaks of the waveform change accordingly. The total harmonic distortion (THD) is calculated as described in (6.13), starting from the 2nd harmonic to the 40th one. The calculated THD values for the voltages are shown in Table 6.7.

$$\text{THD} = \frac{1}{I_{f1}} \sqrt{\sum_{l=2}^{40} (I_{fl})^2} \quad (6.13)$$

Table 6.7 Voltage THD evaluation of the SVM schemes

Scheme	THD
VCT	8.14%
CMR-SVM 1	13.8%
CMR-SVM 2	14.9%
CMR-SVM 3	2.8%

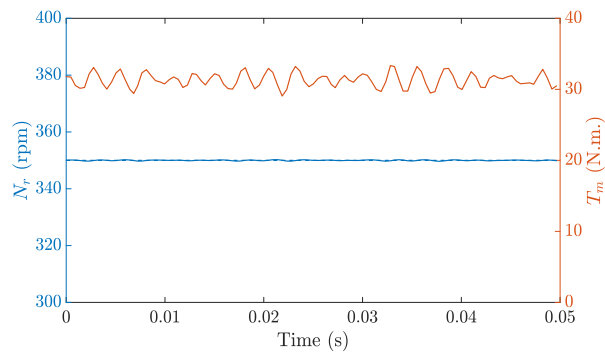
The CMV is then calculated by substituting the measured voltages $v_{P_1n_1}$, $v_{N_1n_1}$, $v_{P_2n_2}$, $v_{N_2n_2}$ in (6.2). The results are shown in Figure 6.15, which indicates that the lowest peak-to-peak

voltage is achieved in the case of CMR-SVM3. The methods CMR-SVM1 and CMR-SVM2 achieve lower peak-to-peak CMV compared to the one in the VCT case. The harmonic spectrums of the CMV waveforms are shown in Figure 6.16.

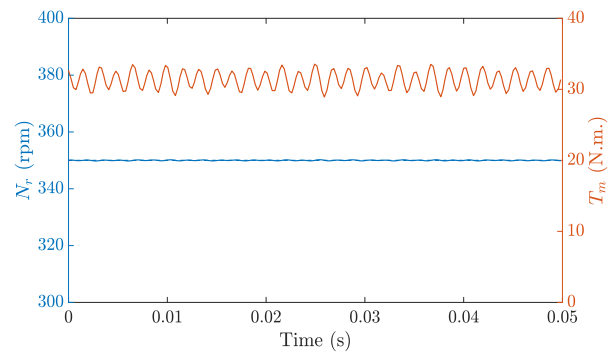
A summary of all the quantitative results is given in Table 6.8 to compare all the schemes regarding CMV. The results include the harmonic content of the CMV at $h = 1$ and $h = 3$, as well as the peak-to-peak values CMV_{P-P} and RMS values CMV_{RMS} of the CMV waveform. The CMR-SVM3 excels in both the peak-to-peak and RMS values. The percentage reductions in CMV_{P-P} achieved by the proposed methods are 30 %, 32 %, and 45 % in the cases of CMR-SVM1, CMR-SVM2, and CMR-SVM3, respectively, compared to the VCT case. Meanwhile, the reductions in CMV_{RMS} are around 35 %, 34%, and 44 % in all cases.

Table 6.8 CMV Evaluation of The SVM Schemes

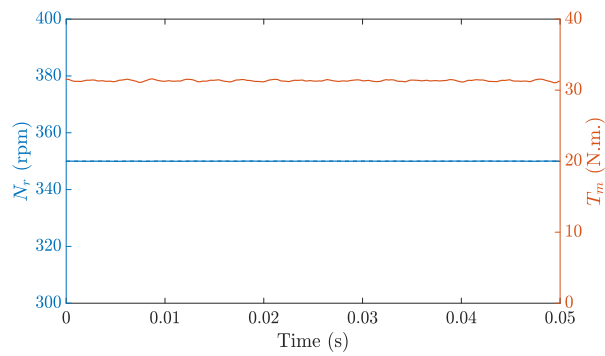
Scheme	VCT	CMR-SVM 1	CMR-SVM 2	CMR-SVM 3
CMV_{P-P}	144 V	101 V	99 V	79 V
$\frac{CMV_{P-P}}{CMV_{P-P,VCT}} * 100\%$	100 %	70.14 %	68.75 %	54.86 %
CMV_{RMS}	105 V	67.9 V	68.8 V	58.9 V
$\frac{CMV_{RMS}}{CMV_{RMS,VCT}} * 100\%$	100 %	64.67 %	65.52 %	56.1 %



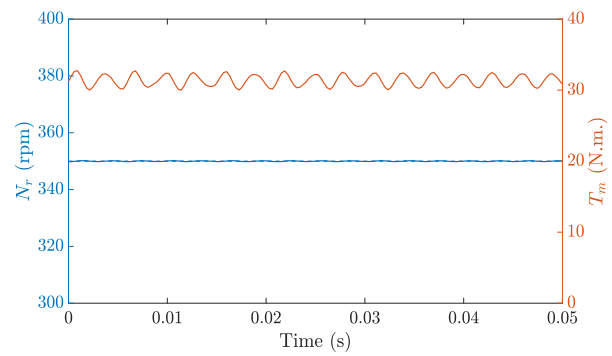
(a) CMR-SVM1



(b) CMR-SVM2



(c) CMR-SVM3



(d) VCT

Figure 6.10 Motor speed and torque for the VCT and the proposed CMR-SVM schemes under the same point of operation.

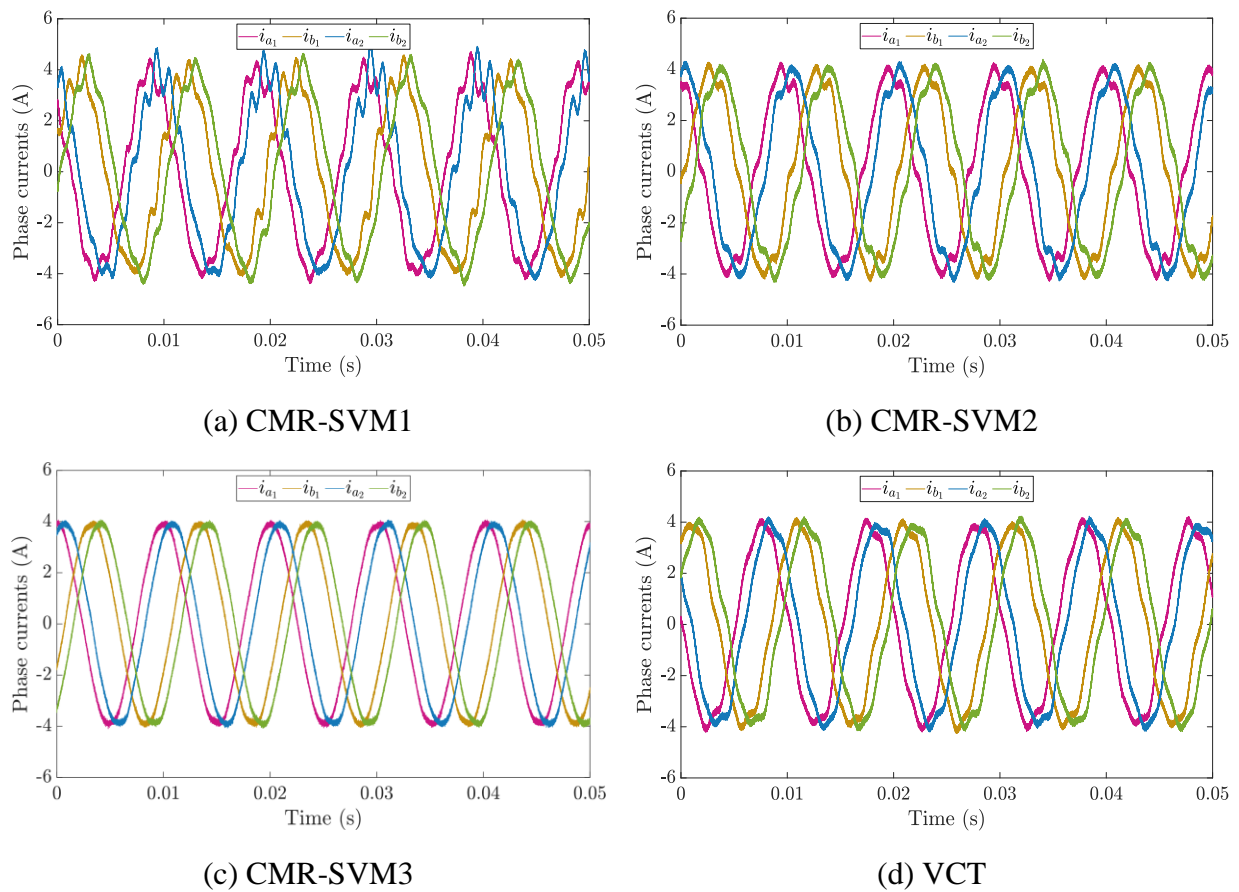
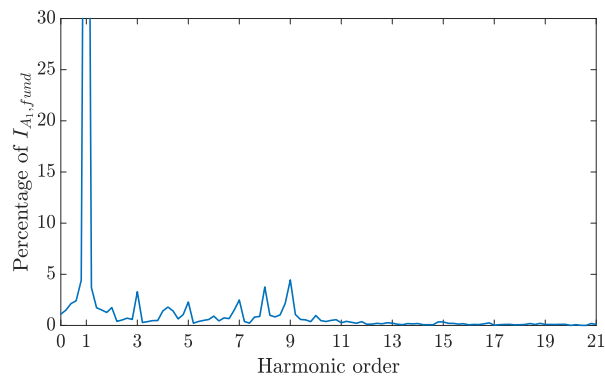
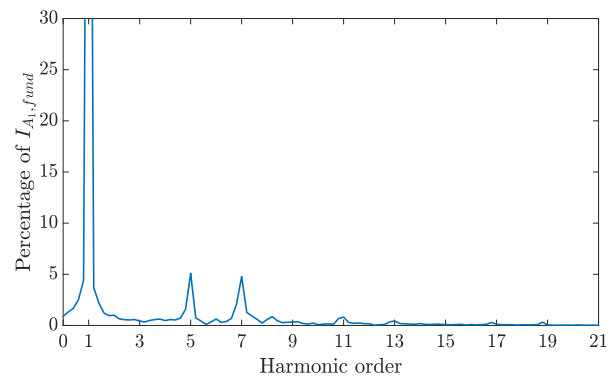


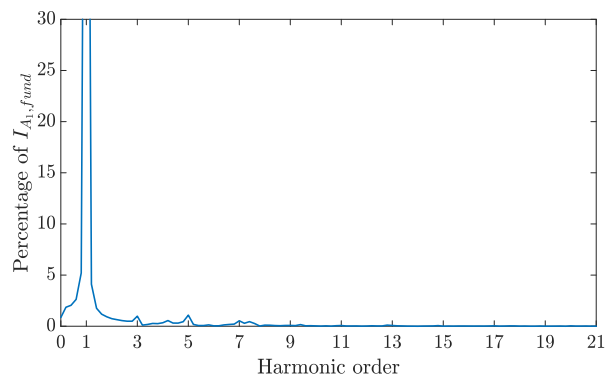
Figure 6.11 Motor phase currents for the VCT and the proposed CMR-SVM schemes under the same point of operation.



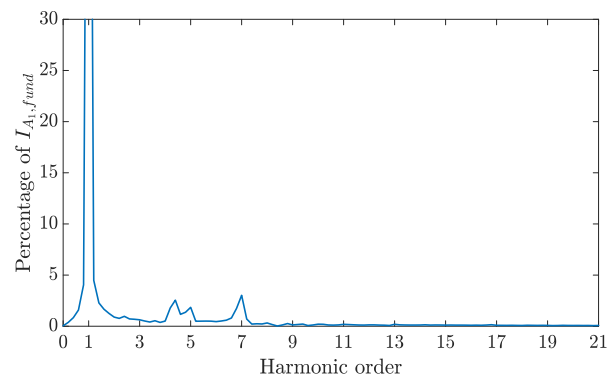
(a) CMR-SVM1



(b) CMR-SVM2

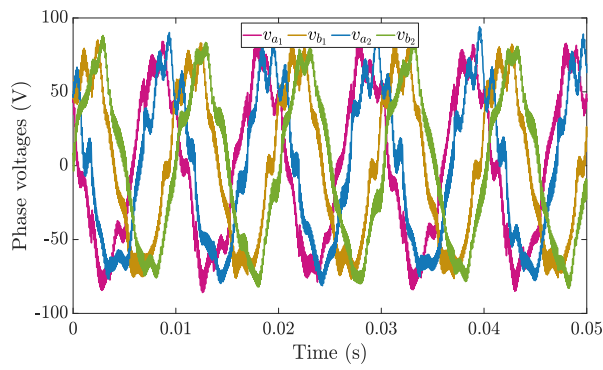


(c) CMR-SVM3

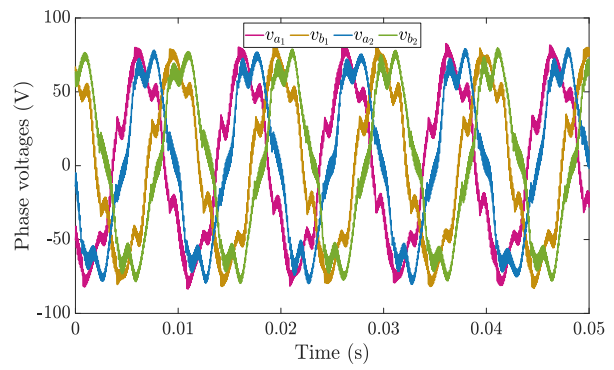


(d) VCT

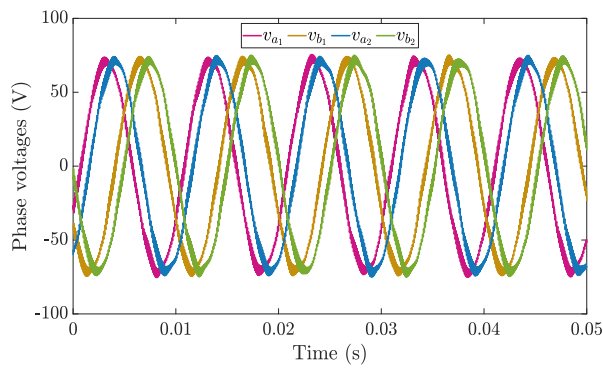
Figure 6.12 Harmonic spectrum of the motor phase currents for the VCT and the proposed CMR-SVM schemes under the same point of operation.



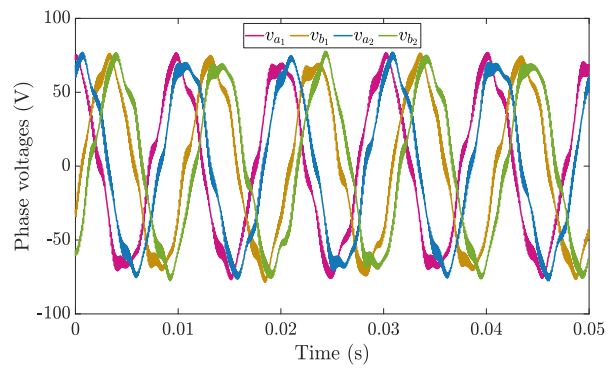
(a) CMR-SVM1



(b) CMR-SVM2

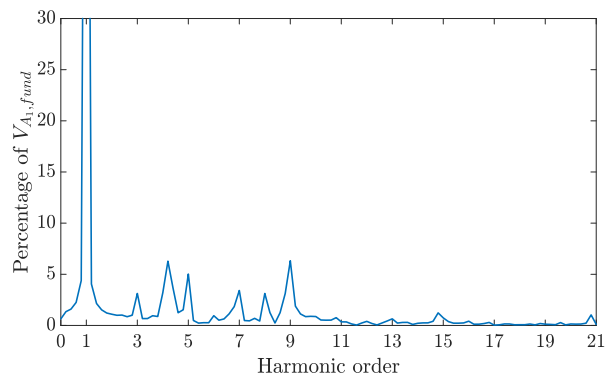


(c) CMR-SVM3

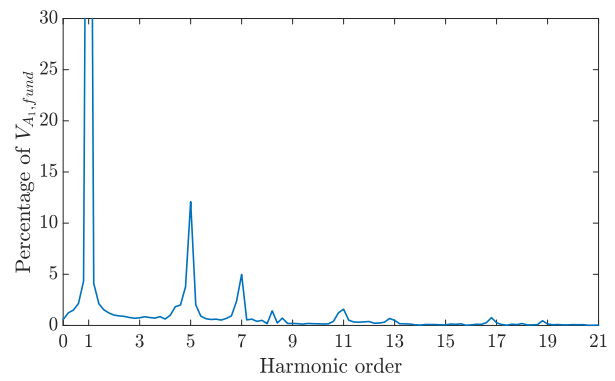


(d) VCT

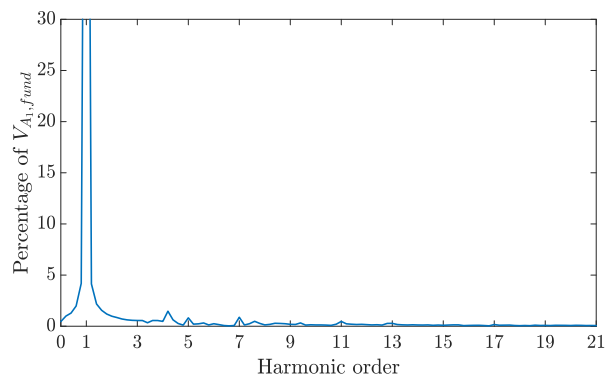
Figure 6.13 Motor phase voltages for the VCT and the proposed CMR-SVM schemes under the same point of operation.



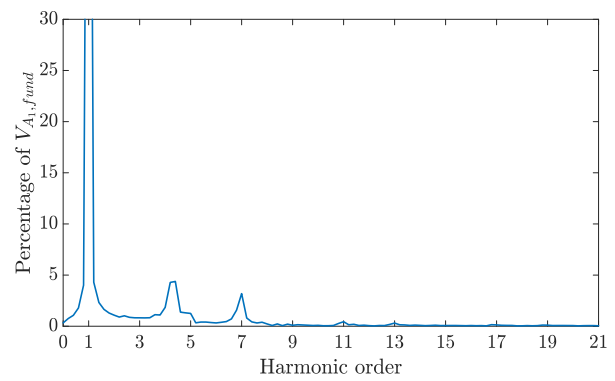
(a) CMR-SVM1



(b) CMR-SVM2

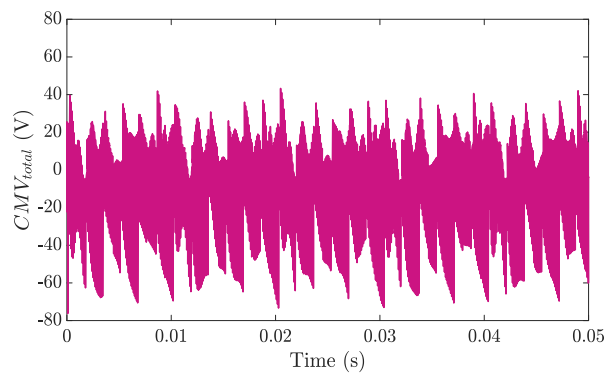


(c) CMR-SVM3

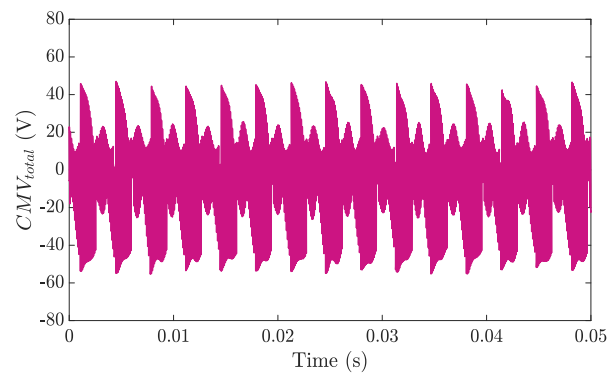


(d) VCT

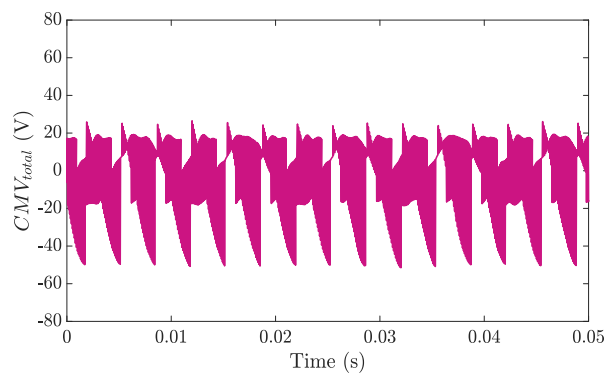
Figure 6.14 Harmonic spectrum of the motor phase voltages for the VCT and the proposed CMR-SVM schemes under the same point of operation.



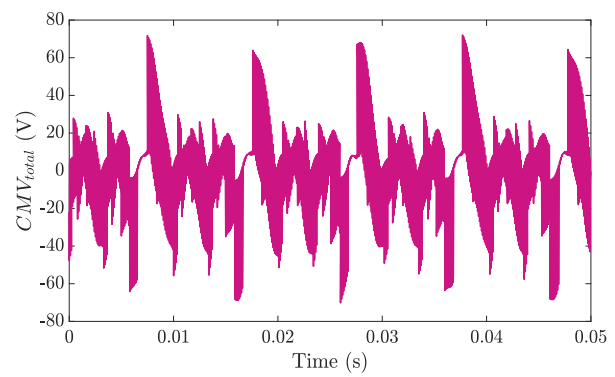
(a) CMR-SVM1



(b) CMR-SVM2



(c) CMR-SVM3



(d) VCT

Figure 6.15 CMV of the VCT and the proposed CMR-SVM schemes under the same point of operation.

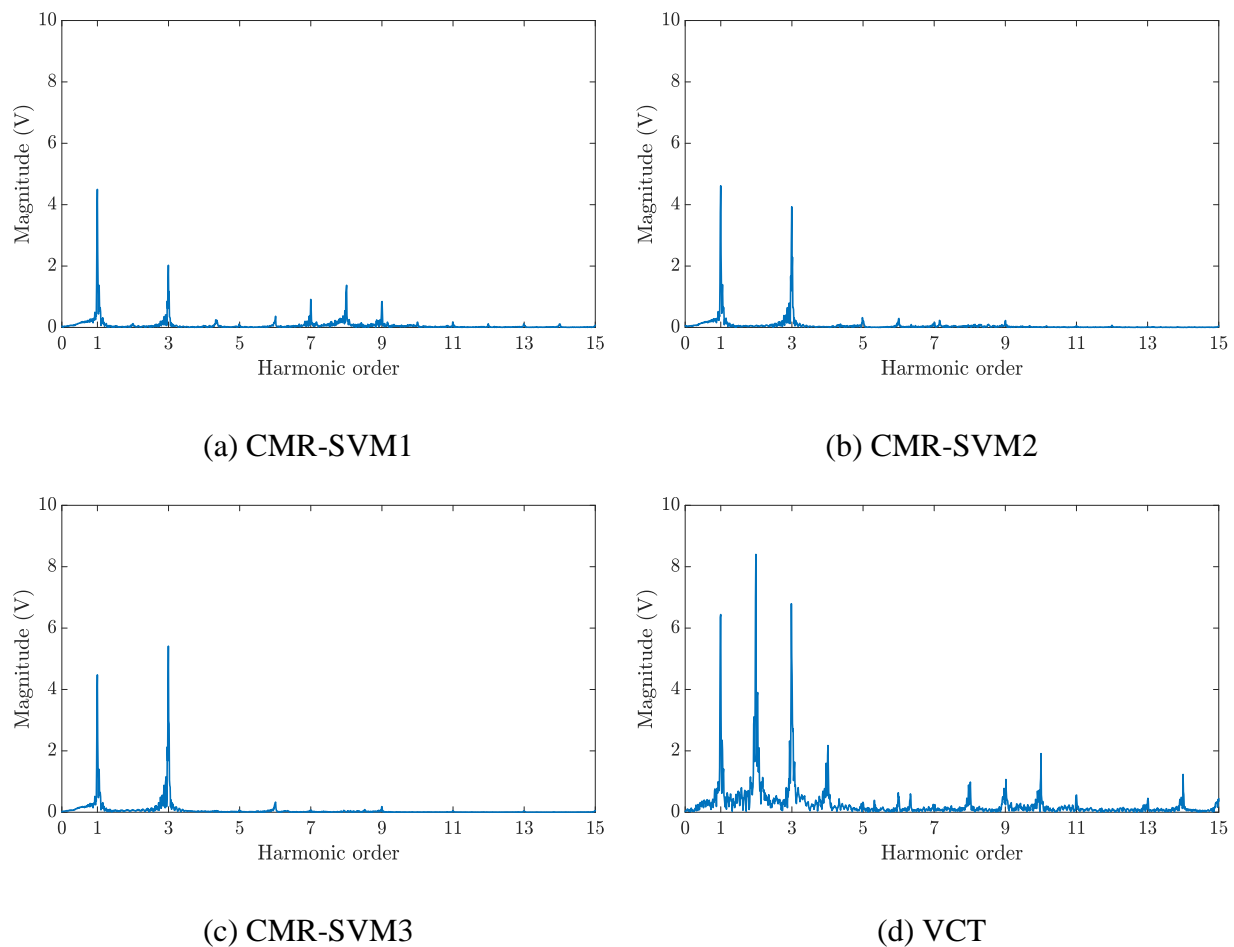


Figure 6.16 Harmonic spectrum of the CMV of the VCT and the proposed CMR-SVM schemes under the same point of operation.

6.6. Summary

This chapter proposed an SVM method to minimize the CMV associated with the inverter operation to increase the reliability aspect of the proposed drive. The method is based on the inherent feature of six-phase drives to reduce the CMV content by selecting the appropriate switching states. Three proposals are discussed as one of them is novel (CMR-SVM1) and two adopted schemes from VSI topology. One of the benefits of applying the proposed methods is

utilizing a preselected set of switching states per sector with a guarantee of CMV reduction without measuring the motor phase voltages.

The comparison between the proposed methods shows that the CMR-SVM 1 and 2 suffer from a limited dc-link current utilization while they are promising in the CMV reduction, given that the output voltages are sinusoidal. The CMR-SVM method fully utilizes the dc-link current; however, the expected CMV reduction is less than the two former methods. The experimental results show that all the proposed methods achieve lower CMV than the conventional VCT method, while the CMR-SVM 3 achieved superior overall performance. The results reflect both the anticipated CMR reduction from applying the selected switching states in each method and the quality of the motor voltages. Since the CMR-SVM 1 and 2 lack in the department of motor voltage quality, the CMR-SVM 3 achieves the best motor voltages accompanied by the reduction of the CMV. Better results of CMR-SVM 1 and 2 can be obtained by using high filtering capacitors.

Chapter 7

Conclusions and Future Work

7.1. Summary

This dissertation researches the feasibility of the powertrains based on six-phase CSI for future HDEVs in terms of increasing reliability. The following subsections summarize all the conclusions of the Thesis's contributions.

7.1.1. Powertrain configuration

Three proposed configurations for powertrains based on six-phase CSI are studied from the perspective of the HDEV applications. The case study followed by the experimental results of a scaled-down prototype shows that the most suitable configuration is the S-CSI-based configuration. This configuration best utilizes the semiconductors for the dc-dc converters and the CSI. P-CSI configuration requires double the dc-link current compared to C-CSI and S-CSI ones.

Meanwhile, the C-CSI configuration requires doubling the battery voltage compared to the P-CSI and S-CSI ones.

Consequently, neither raising the battery voltage nor the dc-link current is necessary in the case of the S-CSI configuration. The S-CSI configuration has the same number of semiconductors with the same rating as the other configurations, which alleviates the need for extra components. Furthermore, the S-CSI is based on modularity, accounting for more reliability and a more straightforward manufacturing process.

7.1.2. Extension of DC-Link current utilization

A new modulation scheme is presented to control a six-phase S-CSI with minimized harmonic contents. The proposed method can also increase the modulation index range by about 8%, which is very attractive for motor drive applications that can improve the torque density. The modulation index range is classified into two regions and the calculation of the dwell times is the same for the full range, which can help for simple implementation. The experimental results show that the method effectively eliminates the low-order harmonic in Region I, where the degrees of freedom allow this feature. The extension of the modulation range is verified experimentally at the cost of an increase in the asymmetries harmonic content. The S-CSI topology combined with the proposed method produces the output currents with unavoidable yet minimized harmonic content in the extension region with a near flat-top waveform. This feature is also required in motor drives applications to avoid iron saturation and exceeding designed current stresses for the converter semiconductors. The simplicity of the method promotes it for application to other multiphase systems quickly based on their respective asymmetry subspaces.

7.1.3. CMV reduction

In this work, three proposed approaches have been introduced to mitigate the severe issue of CMV in six-phase S-CSIs. The analytical study of the CMV associated with such a converter shows that a low level of peak and RMS CMV can be achieved by selecting the appropriate vectors per each sector of modulation. The details of each SVM scheme are illustrated and followed by an evaluation for comparison. The comparisons show a compromise to be made by the user to select between the proposed schemes according to the application status. The evaluation study shows that all the proposed techniques reduce the CMV content. However, the cost of applying schemes 1 and 2 is the higher design constraints and increased conduction and switching losses of the converter.

On the other hand, a reduced CMV content can also be achieved by applying CMR-SVM 3 while maintaining the utilization of the dc-link current. Furthermore, The CMR-SVM 3 achieves the lowest CMV content as proven experimentally. The experimental results show that the CMV content's significant factors are the active and null vectors selection, load power factor, and phase voltage harmonic contents. The CMR-SVM 3 achieved the best results since it is an all-around scheme with respect to all the factors mentioned above. Significant reductions in the CMV_{RMS} have been achieved compared to the VCT method by 35 %, 34%, and 44 % in CMR-SVM 1, 2, and 3, respectively. The studies show that different loading conditions can achieve an even higher reduction. The comparisons presented in the experimental section show that the CMR-SVM 3 is the best compromise between CMV content, conduction, switching losses, and output current quality of the four SVM schemes.

7.2. Future Work

There is future work to be done exploring the powertrains based on CSI and six-phase PMSM drives in terms of lower cost, higher performance, and better reliability. The research represented in this dissertation has addressed some of the fundamental problems, which gives direction for future work. This section provides an overview of some areas of future interest.

- Study the relation between the different subspaces and the filter capacitors for more accurate filter selection.
- One of the important aspects of realizing the proposed powertrains industrially is the sizing and design of the dc-link inductor. The minimum inductance required can be further investigated. Another interesting point is utilizing switching patterns and control techniques to decrease the needed inductance value to meet the standards of operation. Furthermore, the selection of materials and characteristics of the choke is crucial like the core material, core shape, the conductor material, cross sectional size of the conductor, and number of turns.
- One of the recent trends of control methods is model predictive control (MPC) because of its simplicity and discarding need for tuning PID controllers. The MPC method is also known for its high dynamic response which can be utilized to improve the dynamic performance of the CSI topology. A proper observer can also be a building block to develop robust SVM and MPC techniques for the CSI.
- Drive dynamics are dependant on the quality of the observers used in the control process like to compensate for the capacitor filter stage current. The investigation of improving the currently used observer against parameters mismatch and different loading conditions.

- Fault-tolerant operation is one of the outstanding features of Multiphase systems. Since CSI topology is inherently immune to short-circuit faults, future work about fault-tolerant operation against open-circuit faults is an interesting topic that can push the fault-tolerance of the topology furthermore.

References

- [1] U. S. D. o. Energy, "U.S. DRIVE Electrical and Electronics Technical Team Roadmap," ed, October 2017.
- [2] TM4 SUMO MD [Online]. Available: <https://www.tm4.com/products/direct-drive-electric-powertrain/sumo-md/>
- [3] A. Salem and M. Narimani, "A Review on Multiphase Drives for Automotive Traction Applications," *IEEE Transactions on Transportation Electrification*, vol. 5, no. 4, pp. 1329-1348, 2019.
- [4] R. J. Ramm, D. Sasaridis, C. Campbell, W. Liu, "Busbar locating component," U.S. Patent US14557398, 2014.
- [5] W. N. W. A. Munim, M. J. Duran, H. S. Che, M. Bermúdez, I. González-Prieto, and N. A. Rahim, "A Unified Analysis of the Fault Tolerance Capability in Six-Phase Induction Motor Drives," *IEEE Transactions on Power Electronics*, vol. 32, no. 10, pp. 7824-7836, 2017.
- [6] H. M. Eldeeb, A. S. Abdel-Khalik, and C. M. Hackl, "Postfault Full Torque–Speed Exploitation of Dual Three-Phase IPMSM Drives," *IEEE Transactions on Industrial Electronics*, vol. 66, no. 9, pp. 6746-6756, 2019.
- [7] G. Feng, C. Lai, M. Kelly, and N. C. Kar, "Dual Three-Phase PMSM Torque Modeling and Maximum Torque per Peak Current Control Through Optimized Harmonic Current Injection," *IEEE Transactions on Industrial Electronics*, vol. 66, no. 5, pp. 3356-3368, 2019.
- [8] A. Cervone, M. Slunjski, E. Levi, and G. Brando, "Optimal Third-Harmonic Current Injection for Asymmetrical Multiphase Permanent Magnet Synchronous Machines," *IEEE Transactions on Industrial Electronics*, vol. 68, no. 4, pp. 2772-2783, 2021.
- [9] J. Paredes, B. Prieto, M. Satrústegui, I. Elósegui, and P. González, "Improving the Performance of a 1-MW Induction Machine by Optimally Shifting From a Three-Phase to a Six-Phase Machine Design by Rearranging the Coil Connections," *IEEE Transactions on Industrial Electronics*, vol. 68, no. 2, pp. 1035-1045, 2021.
- [10] K. S. Khan, W. M. Arshad, and S. Kanerva, "On performance figures of multiphase machines," in *2008 18th International Conference on Electrical Machines*, 2008, pp. 1-5.
- [11] TM4. Available: <https://www.tm4.com/products/direct-drive-electric-powertrain/sumo-md/>
- [12] E. Jung, H. Yoo, S. Sul, H. Choi, and Y. Choi, "A Nine-Phase Permanent-Magnet Motor Drive System for an Ultrahigh-Speed Elevator," *IEEE Transactions on Industry Applications*, vol. 48, no. 3, pp. 987-995, 2012.

- [13] P. Liu, Z. Wang, Q. Song, Y. Xu, and M. Cheng, "Optimized SVM and Remedial Control Strategy for Cascaded Current-Source-Converters-Based Dual Three-Phase PMSM Drives System," *IEEE Transactions on Power Electronics*, vol. 35, no. 6, pp. 6153-6164, 2020.
- [14] R. Automation. Powerflex 7000 medium voltage ac drives [Online]. Available: <https://www.rockwellautomation.com/en-za/products/hardware/allen-bradley/drives-and-motors/medium-voltage-ac-drives/powerflex-7000-ac-drive.html>
- [15] Z. Wu and G. Su, "High-performance permanent magnet machine drive for electric vehicle applications using a current source inverter," in *2008 34th Annual Conference of IEEE Industrial Electronics*, 2008, pp. 2812-2817.
- [16] L. Tang and G. Su, "Boost mode test of a current-source-inverter-fed permanent magnet synchronous motor drive for automotive applications," in *2010 IEEE 12th Workshop on Control and Modeling for Power Electronics (COMPEL)*, 2010, pp. 1-8.
- [17] J. He, Y. Lyu, J. Han, and C. Wang, "An SVM Approach for Five-Phase Current Source Converters Output Current Harmonics and Common-Mode Voltage Mitigation," *IEEE Transactions on Industrial Electronics*, vol. 67, no. 7, pp. 5232-5245, 2020.
- [18] E. Giraldo and A. Garces, "An Adaptive Control Strategy for a Wind Energy Conversion System Based on PWM-CSC and PMSG," *IEEE Transactions on Power Systems*, vol. 29, no. 3, pp. 1446-1453, 2014.
- [19] H. Chen and H. Huang, "Design of buck-type current source inverter fed brushless DC motor drive and its application to position sensorless control with square-wave current," *IET Electric Power Applications*, vol. 7, no. 5, pp. 416-426, 2013.
- [20] P. Liu, Z. Wang, Y. Xu, Z. Zou, F. Deng, and Y. R. G. Li, "Improved Harmonic Profile for High-Power PWM Current-Source Converters with Modified Space Vector Modulation Schemes," *IEEE Transactions on Power Electronics*, pp. 1-1, 2021.
- [21] B. Wu and M. Narimani, *High-power converters and AC drives*. John Wiley & Sons, 2017.
- [22] M. A. Elgenedy, A. A. Elserougi, A. S. Abdel-Khalik, A. M. Massoud, and S. Ahmed, "A Space Vector PWM Scheme for Five-Phase Current-Source Converters," *IEEE Transactions on Industrial Electronics*, vol. 63, no. 1, pp. 562-573, 2016.
- [23] E. E. Ward and H. Härer, "Preliminary investigation of an inverter-fed 5-phase induction motor," *Proceedings of the Institution of Electrical Engineers*, vol. 116, no. 6, pp. 980-984, 1969.
- [24] M. A. Abbas, R. Christen, and T. M. Jahns, "Six-Phase Voltage Source Inverter Driven Induction Motor," *IEEE Transactions on Industry Applications*, vol. IA-20, no. 5, pp. 1251-1259, 1984.
- [25] N. Bodo, E. Levi, I. Subotic, J. Espina, L. Empringham, and C. M. Johnson, "Efficiency Evaluation of Fully Integrated On-Board EV Battery Chargers With Nine-Phase Machines," *IEEE Transactions on Energy Conversion*, vol. 32, no. 1, pp. 257-266, 2017.
- [26] M. S. Diab, A. A. Elserougi, A. S. Abdel-Khalik, A. M. Massoud, and S. Ahmed, "A Nine-Switch-Converter-Based Integrated Motor Drive and Battery Charger System for EVs

- Using Symmetrical Six-Phase Machines," *IEEE Transactions on Industrial Electronics*, vol. 63, no. 9, pp. 5326-5335, 2016.
- [27] I. Subotic, N. Bodo, E. Levi, M. Jones, and V. Levi, "Isolated Chargers for EVs Incorporating Six-Phase Machines," *IEEE Transactions on Industrial Electronics*, vol. 63, no. 1, pp. 653-664, 2016.
- [28] V. F. Pires, A. Cordeiro, D. Foito, and J. F. Silva, "A Three-Phase On-Board Integrated Battery Charger for EVs with Six-Phase Machine and Nine Switch Converter," in *2019 IEEE 13th International Conference on Compatibility, Power Electronics and Power Engineering (CPE-POWERENG)*, 2019, pp. 1-6.
- [29] H. Zahr, F. Sculler, and E. Semail, "Five-phase SPM machine with electronic pole changing effect for marine propulsion," in *2016 International Conference on Electrical Systems for Aircraft, Railway, Ship Propulsion and Road Vehicles & International Transportation Electrification Conference (ESARS-ITEC)*, 2016, pp. 1-6.
- [30] M. Qiao, C. Jiang, Y. Zhu, and G. Li, "Research on Design Method and Electromagnetic Vibration of Six-Phase Fractional-Slot Concentrated-Winding PM Motor Suitable for Ship Propulsion," *IEEE Access*, vol. 4, pp. 8535-8543, 2016.
- [31] E. Levi, "Multiphase Electric Machines for Variable-Speed Applications," *IEEE Transactions on Industrial Electronics*, vol. 55, no. 5, pp. 1893-1909, 2008.
- [32] Z. Liu, Y. Li, and Z. Zheng, "A review of drive techniques for multiphase machines," *CES Transactions on Electrical Machines and Systems*, vol. 2, no. 2, pp. 243-251, 2018.
- [33] E. Levi, N. Bodo, O. Dordevic, and M. Jones, "Recent advances in power electronic converter control for multiphase drive systems," in *2013 IEEE Workshop on Electrical Machines Design, Control and Diagnosis (WEMDCD)*, 2013, pp. 158-167.
- [34] M. J. Duran and F. Barrero, "Recent Advances in the Design, Modeling, and Control of Multiphase Machines—Part II," *IEEE Transactions on Industrial Electronics*, vol. 63, no. 1, pp. 459-468, 2016.
- [35] F. Barrero and M. J. Duran, "Recent Advances in the Design, Modeling, and Control of Multiphase Machines—Part I," *IEEE Transactions on Industrial Electronics*, vol. 63, no. 1, pp. 449-458, 2016.
- [36] F. Baneira, J. Doval-Gandoy, A. G. Yepes, L. Ó, and D. Pérez-Estévez, "Control strategy for dual three-phase PMSMs with minimum losses in the full torque operation range under single open-phase fault," in *2016 IEEE Energy Conversion Congress and Exposition (ECCE)*, 2016, pp. 1-8.
- [37] X. Wang, Z. Wang, Z. Xu, M. Cheng, W. Wang, and Y. Hu, "Comprehensive Diagnosis and Tolerance Strategies for Electrical Faults and Sensor Faults in Dual Three-Phase PMSM Drives," *IEEE Transactions on Power Electronics*, pp. 1-1, 2018.
- [38] H. S. Che, M. J. Duran, E. Levi, M. Jones, W. Hew, and N. A. Rahim, "Postfault Operation of an Asymmetrical Six-Phase Induction Machine With Single and Two Isolated Neutral Points," *IEEE Transactions on Power Electronics*, vol. 29, no. 10, pp. 5406-5416, 2014.

- [39] A. G. Yepes, J. Doval-Gandoy, F. Baneira, and H. Toliyat, "Postfault Strategy for Dual Three-Phase Machines With Minimum Loss in the Full Torque Operation Range Under Two Open Phases," in *2018 IEEE Energy Conversion Congress and Exposition (ECCE)*, 2018, pp. 3380-3385.
- [40] J. Fu and T. A. Lipo, "Disturbance free operation of a multiphase current regulated motor drive with an opened phase," in *Conference Record of the 1993 IEEE Industry Applications Conference Twenty-Eighth IAS Annual Meeting*, 1993, pp. 637-644 vol.1.
- [41] R. O. C. Lyra and T. A. Lipo, "Torque density improvement in a six-phase induction motor with third harmonic current injection," in *Conference Record of the 2001 IEEE Industry Applications Conference. 36th IAS Annual Meeting (Cat. No.01CH37248)*, 2001, vol. 3, pp. 1779-1786 vol.3.
- [42] K. Wang, Z. Q. Zhu, Y. Ren, and G. Ombach, "Torque Improvement of Dual Three-Phase Permanent-Magnet Machine With Third-Harmonic Current Injection," *IEEE Transactions on Industrial Electronics*, vol. 62, no. 11, pp. 6833-6844, 2015.
- [43] Y. Hu, Z. Q. Zhu, and M. Odavic, "Torque Capability Enhancement of Dual Three-Phase PMSM Drive With Fifth and Seventh Current Harmonics Injection," *IEEE Transactions on Industry Applications*, vol. 53, no. 5, pp. 4526-4535, 2017.
- [44] F. B. Bendixen, F. Blaabjerg, P. O. Rasmussen, P. Vadstrup, and K. Krabbe, "Controlling the DC-link midpoint potential in a six-phase motor-drive," in *2004 IEEE 35th Annual Power Electronics Specialists Conference (IEEE Cat. No.04CH37551)*, 2004, vol. 3, pp. 2128-2132 Vol.3.
- [45] A. S. Abdel-Khalik, A. M. Massoud, and S. Ahmed, "Effect of DC-Link Voltage Limitation on Postfault Steady-State Performance of Asymmetrical Six-Phase Induction Machine," *IEEE Transactions on Industrial Electronics*, vol. 65, no. 9, pp. 6890 - 6900, 2018.
- [46] A. S. Abdel-Khalik, M. I. Masoud, and B. W. Williams, "Improved Flux Pattern With Third Harmonic Injection for Multiphase Induction Machines," *IEEE Transactions on Power Electronics*, vol. 27, no. 3, pp. 1563-1578, 2012.
- [47] Z. Yifan and T. A. Lipo, "Space vector PWM control of dual three-phase induction machine using vector space decomposition," *IEEE Transactions on Industry Applications*, vol. 31, no. 5, pp. 1100-1109, 1995.
- [48] Y. Zhao and T. A. Lipo, "Modeling and control of a multi-phase induction machine with structural unbalance," *IEEE Transactions on Energy Conversion*, vol. 11, no. 3, pp. 570-577, 1996.
- [49] H. S. Che, E. Levi, M. Jones, W. P. Hew, and N. A. Rahim, "Current Control Methods for an Asymmetrical Six-Phase Induction Motor Drive," *IEEE Transactions on Power Electronics*, vol. 29, no. 1, pp. 407-417, 2014.
- [50] J. Reimers, L. Dorn-Gomba, C. Mak, and A. Emadi, "Automotive Traction Inverters: Current Status and Future Trends," *IEEE Transactions on Vehicular Technology*, pp. 1-1, 2019.

- [51] M. J. Duran, I. Gonzalez-Prieto, N. Rios-Garcia, and F. Barrero, "A Simple, Fast, and Robust Open-Phase Fault Detection Technique for Six-Phase Induction Motor Drives," *IEEE Transactions on Power Electronics*, vol. 33, no. 1, pp. 547-557, 2018.
- [52] F. Baneira, J. Doval-Gandoy, A. G. Yepes, L. Ó, and D. Pérez-Estévez, "Control Strategy for Multiphase Drives With Minimum Losses in the Full Torque Operation Range Under Single Open-Phase Fault," *IEEE Transactions on Power Electronics*, vol. 32, no. 8, pp. 6275-6285, 2017.
- [53] F. Baneira, J. Doval-Gandoy, A. G. Yepes, L. Ó, and D. Pérez-Estévez, "Comparison of Postfault Strategies for Current Reference Generation for Dual Three-Phase Machines in Terms of Converter Losses," *IEEE Transactions on Power Electronics*, vol. 32, no. 11, pp. 8243-8246, 2017.
- [54] A. S. Abdel-Khalik, S. M. Gadoue, M. I. Masoud, and B. W. Williams, "Optimum Flux Distribution With Harmonic Injection for a Multiphase Induction Machine Using Genetic Algorithms," *IEEE Transactions on Energy Conversion*, vol. 26, no. 2, pp. 501-512, 2011.
- [55] A. S. Abdel-Khalik and S. M. Gadoue, "Improved flux pattern by third harmonic injection for multiphase induction machines using neural network," *Alexandria Engineering Journal*, vol. 50, no. 2, pp. 163-169, 2011/06/01/ 2011.
- [56] Z. Nie, "Multiphase Power Electronic Converters for Electric Vehicle Machine Drive Systems," PhD, ECE, McMaster University, 2018.
- [57] I. Zoric, M. Jones, and E. Levi, "Vector space decomposition algorithm for asymmetrical multiphase machines," in *2017 International Symposium on Power Electronics (Ee)*, 2017, pp. 1-6.
- [58] Z. Wang, Y. Wang, J. Chen, and Y. Hu, "Decoupled Vector Space Decomposition Based Space Vector Modulation for Dual Three-Phase Three-Level Motor Drives," *IEEE Transactions on Power Electronics*, vol. 33, no. 12, pp. 10683-10697, 2018.
- [59] H. Kouki, M. B. Fredj, and H. Rehaoulia, "Vector space decomposition for double star induction machine modeling," in *2014 15th International Conference on Sciences and Techniques of Automatic Control and Computer Engineering (STA)*, 2014, pp. 581-586.
- [60] V. Reber. (2016) E-power: New Possibilities with 800-Volt Charging. *Porsche Engineering Magazine*. pp 10-15. Available: <https://www.porscheengineering.com/peg/en/about/magazine/>
- [61] A. Boglietti, R. Bojoi, A. Cavagnino, and A. Tenconi, "Efficiency Analysis of PWM Inverter Fed Three-Phase and Dual Three-Phase Induction Machines," in *Conference Record of the 2006 IEEE Industry Applications Conference Forty-First IAS Annual Meeting*, 2006, vol. 1, pp. 434-440.
- [62] A. Boglietti, R. Bojoi, A. Cavagnino, and A. Tenconi, "Efficiency Analysis of PWM Inverter Fed Three-Phase and Dual Three-Phase High Frequency Induction Machines for Low/Medium Power Applications," *IEEE Transactions on Industrial Electronics*, vol. 55, no. 5, pp. 2015-2023, 2008.

- [63] P. R. Rakesh and G. Narayanan, "Investigation on Zero-Sequence Signal Injection for Improved Harmonic Performance in Split-Phase Induction Motor Drives," *IEEE Transactions on Industrial Electronics*, vol. 64, no. 4, pp. 2732-2741, 2017.
- [64] J. Prieto, E. Levi, F. Barrero, and S. Toral, "Output current ripple analysis for asymmetrical six-phase drives using double zero-sequence injection PWM," in *IECON 2011 - 37th Annual Conference of the IEEE Industrial Electronics Society*, 2011, pp. 3692-3697.
- [65] P. R. Rakesh and G. Narayanan, "Analysis of sine-triangle and zero-sequence injection modulation schemes for split-phase induction motor drive," *IET Power Electronics*, vol. 9, no. 2, pp. 344-355, 2016.
- [66] T. Zhao, Y. Zhang, H. Xu, X. Gui, and D. Xu, "DTP-PMSM Drive with Proportional Resonant Regulator and Dual Zero Injection PWM Control Method," in *2018 21st International Conference on Electrical Machines and Systems (ICEMS)*, 2018, pp. 1628-1633.
- [67] C. Wang, K. Wang, and X. You, "Research on Synchronized SVPWM Strategies Under Low Switching Frequency for Six-Phase VSI-Fed Asymmetrical Dual Stator Induction Machine," *IEEE Transactions on Industrial Electronics*, vol. 63, no. 11, pp. 6767-6776, 2016.
- [68] Y. Yu, L. Gao, Y. Liu, and F. Chai, "24-Sector space vector decomposition for a dual three-phase PMSM," in *2014 17th International Conference on Electrical Machines and Systems (ICEMS)*, 2014, pp. 1601-1606.
- [69] K. Marouani, L. Baghli, D. Hadiouche, A. Kheloui, and A. Rezzoug, "A New PWM Strategy Based on a 24-Sector Vector Space Decomposition for a Six-Phase VSI-Fed Dual Stator Induction Motor," *IEEE Transactions on Industrial Electronics*, vol. 55, no. 5, pp. 1910-1920, 2008.
- [70] K. Marouani, L. Baghli, D. Hadiouche, A. Kheloui, and A. Rezzoug, "Discontinuous SVPWM Techniques for Double Star Induction Motor Drive Control," in *IECON 2006 - 32nd Annual Conference on IEEE Industrial Electronics*, 2006, pp. 902-907.
- [71] A. R. Bakhshai, G. Joos, and H. Jin, "Space vector PWM control of a split-phase induction machine using the vector classification technique," in *APEC '98 Thirteenth Annual Applied Power Electronics Conference and Exposition*, 1998, vol. 2, pp. 802-808 vol.2.
- [72] D. Yazdani, S. A. Khajehoddin, A. Bakhshai, and G. Joos, "A Generalized Space Vector Classification Technique for Six-Phase Inverters," in *2007 IEEE Power Electronics Specialists Conference*, 2007, pp. 2050-2054.
- [73] D. Yazdani, S. A. Khajehoddin, A. Bakhshai, and G. Joos, "Full Utilization of the Inverter in Split-Phase Drives by Means of a Dual Three-Phase Space Vector Classification Algorithm," *IEEE Transactions on Industrial Electronics*, vol. 56, no. 1, pp. 120-129, 2009.
- [74] Y. He, Y. Wang, J. Wu, Y. Feng, and J. Liu, "A comparative study of space vector PWM strategy for dual three-phase permanent-magnet synchronous motor drives," in *2010 Twenty-Fifth Annual IEEE Applied Power Electronics Conference and Exposition (APEC)*, 2010, pp. 915-919.

- [75] G. Grandi, G. Serra, and A. Tani, "Space Vector Modulation of a Six-Phase VSI based on three-phase decomposition," in *2008 International Symposium on Power Electronics, Electrical Drives, Automation and Motion*, 2008, pp. 674-679.
- [76] K. Koiwa and J. Itoh, "A Maximum Power Density Design Method for Nine Switches Matrix Converter Using SiC-MOSFET," *IEEE Transactions on Power Electronics*, vol. 31, no. 2, pp. 1189-1202, 2016.
- [77] A. S. Salem, R. A. Hamdy, A. S. Abdel-Khalik, I. F. El-Arabawy, and M. S. Hamad, "Performance of nine-switch inverter-fed asymmetrical six-phase induction machine under machine and converter faults," in *2016 Eighteenth International Middle East Power Systems Conference (MEPCON)*, 2016, pp. 711-716.
- [78] E. C. d. Santos, C. B. Jacobina, and O. I. d. Silva, "Six-phase machine drive system with nine-switch converter," in *IECON 2011 - 37th Annual Conference of the IEEE Industrial Electronics Society*, 2011, pp. 4204-4209.
- [79] L. Pan *et al.*, "A Novel Space-Vector Modulation Method for Nine-Switch Converter," *IEEE Transactions on Power Electronics*, pp. 1-1, 2019.
- [80] N. Jarutus and Y. Kumsuwan, "Discontinuous and continuous space vector modulations for a nine-switch inverter," in *2016 IEEE 8th International Power Electronics and Motion Control Conference (IPEMC-ECCE Asia)*, 2016, pp. 581-588.
- [81] N. Jarutus and Y. Kumsuwan, "Novel modulation strategy based on generalized two-level PWM theory for nine-switch inverter with reduction of switching commutation," in *IECON 2016 - 42nd Annual Conference of the IEEE Industrial Electronics Society*, 2016, pp. 3529-3534.
- [82] X. Li, L. Qu, B. Zhang, G. Zhang, and H. Liao, "A Simplified Modulation Strategy of Nine-Switch Inverter to Cut Off Half of Switching Modes," *IEEE Access*, vol. 6, pp. 7254-7261, 2018.
- [83] N. Jarutus and Y. Kumsuwan, "A Carrier-Based Phase-Shift Space Vector Modulation Strategy for a Nine-Switch Inverter," *IEEE Transactions on Power Electronics*, vol. 32, no. 5, pp. 3425-3441, 2017.
- [84] N. Jarutus and Y. Kumsuwan, "A comparison between level- and phase-shift space vector duty-cycle modulations using a nine-switch inverter for an ASD," in *2015 18th International Conference on Electrical Machines and Systems (ICEMS)*, 2015, pp. 1877-1883.
- [85] F. Gao, L. Zhang, D. Li, P. C. Loh, Y. Tang, and H. Gao, "Optimal Pulsewidth Modulation of Nine-Switch Converter," *IEEE Transactions on Power Electronics*, vol. 25, no. 9, pp. 2331-2343, 2010.
- [86] S. M. Dehghan, M. Mohamadian, and M. A. E. Andersen, "Full space vectors modulation for nine-switch converters including CF & DF modes," in *2010 4th International Power Engineering and Optimization Conference (PEOCO)*, 2010, pp. 89-94.

- [87] P. R. U. Guazzelli *et al.*, "Dual Predictive Current Control of Grid Connected Nine-Switch Converter Applied to Induction Generator," in *2018 13th IEEE International Conference on Industry Applications (INDUSCON)*, 2018, pp. 1038-1044.
- [88] S. Sharma, M. Aware, and A. Bhowate, "Direct torque control of symmetrical six-phase induction machine using nine switch inverter," in *2017 IEEE Transportation Electrification Conference (ITEC-India)*, 2017, pp. 1-6.
- [89] O. Gulbudak and M. Gokdag, "Predictive dual-induction machine control using nine-switch inverter for multi-drive systems," in *2018 IEEE 12th International Conference on Compatibility, Power Electronics and Power Engineering (CPE-POWERENG 2018)*, 2018, pp. 1-6.
- [90] S. M. Dehghan, M. Mohamadian, A. H. Rajaei, and A. Yazdian, "Full modeling a series HEV based on BZS-NSI," in *2011 2nd Power Electronics, Drive Systems and Technologies Conference*, 2011, pp. 439-444.
- [91] S. M. Dehghan, M. Mohamadian, and A. Yazdian, "Hybrid Electric Vehicle Based on Bidirectional Z-Source Nine-Switch Inverter," *IEEE Transactions on Vehicular Technology*, vol. 59, no. 6, pp. 2641-2653, 2010.
- [92] K. Oka, Y. Nozawa, R. Omata, K. Suzuki, A. Furuya, and K. Matsuse, "Characteristic Comparison between Five-Leg Inverter and Nine-Switch Inverter," in *2007 Power Conversion Conference - Nagoya*, 2007, pp. 279-283.
- [93] C. B. Jacobina, I. S. d. Freitas, C. R. d. Silva, M. B. d. R. Correa, and E. R. C. d. Silva, "Reduced Switch-Count Six-Phase AC Motor Drive Systems Without Input Reactor," *IEEE Transactions on Industrial Electronics*, vol. 55, no. 5, pp. 2024-2032, 2008.
- [94] N. Bodo, M. Jones, and E. Levi, "A Space Vector PWM With Common-Mode Voltage Elimination for Open-End Winding Five-Phase Drives With a Single DC Supply," *IEEE Transactions on Industrial Electronics*, vol. 61, no. 5, pp. 2197-2207, 2014.
- [95] N. A. Azeez, J. Mathew, K. Gopakumar, and C. Cecati, "A 5th and 7th order harmonic suppression scheme for open-end winding asymmetrical six-phase IM drive using capacitor-fed inverter," in *IECON 2013 - 39th Annual Conference of the IEEE Industrial Electronics Society*, 2013, pp. 5118-5123.
- [96] J. Loncarski, M. Leijon, C. Rossi, M. Srdovic, and G. Grandi, "Current ripple evaluation in dual three-phase inverters for open-end winding EV drives," in *2014 International Conference on Connected Vehicles and Expo (ICCVE)*, 2014, pp. 507-513.
- [97] M. Jones, F. Patkar, and E. Levi, "Carrier-based pulse-width modulation techniques for asymmetrical six-phase open-end winding drives," *IET Electric Power Applications*, vol. 7, no. 6, pp. 441-452, 2013.
- [98] F. Patkar, A. Jidin, E. Levi, and M. Jones, "Performance comparison of symmetrical and asymmetrical six-phase open-end winding drives with carrier-based PWM," in *2017 6th International Conference on Electrical Engineering and Informatics (ICEEI)*, 2017, pp. 1-6.

- [99] V. F. M. B. Melo, C. B. Jacobina, N. Rocha, R. P. R. de Sousa, and E. R. J. I. T. o. P. E. Braga-Filho, "Hybrid dual and NPC six-phase drive systems," vol. 32, no. 11, pp. 8606-8617, 2016.
- [100] Z. Wang, J. Chen, and M. Cheng, "Modeling and control of neutral-point-clamping (NPC) three-level inverters fed dual-three phase PMSM drives," in *2015 IEEE Energy Conversion Congress and Exposition (ECCE)*, 2015, pp. 6565-6572.
- [101] Z. Wang, J. Chen, M. Cheng, and R. Na, "Vector space decomposition based control of neutral-point-clamping (NPC) three-level inverters fed dual three-phase PMSM drives," in *IECON 2016 - 42nd Annual Conference of the IEEE Industrial Electronics Society*, 2016, pp. 2988-2993.
- [102] S. Bhattacharya, D. Mascarella, G. Joós, J. Cyr, and J. Xu, "A Dual Three-Level T-NPC Inverter for High-Power Traction Applications," *IEEE Journal of Emerging and Selected Topics in Power Electronics*, vol. 4, no. 2, pp. 668-678, 2016.
- [103] Z. Wang, X. Wang, M. Cheng, and W. Hua, "Direct torque control of T-NPC three-level inverter fed dual three-phase PMSM drives based on double SVM strategy," in *2016 19th International Conference on Electrical Machines and Systems (ICEMS)*, 2016, pp. 1-7.
- [104] J. Wen and K. M. Smedley, "Hexagram Inverter for Medium-Voltage Six-Phase Variable-Speed Drives," *IEEE Transactions on Industrial Electronics*, vol. 55, no. 6, pp. 2473-2481, 2008.
- [105] V. Oleschuk, R. Gregor, J. Rodas, and A. Giangreco, "Dual three-phase system based on four neutral-point-clamped inverters with synchronized space-vector modulation," in *2013 15th European Conference on Power Electronics and Applications (EPE)*, 2013, pp. 1-10.
- [106] V. F. M. B. Melo, C. B. Jacobina, and N. Rocha, "Hybrid open-end and NPC AC six-phase machine drive systems," in *2014 IEEE Energy Conversion Congress and Exposition (ECCE)*, 2014, pp. 3872-3879.
- [107] V. N. R., K. Gopakumar, and L. G. Franquelo, "A Very High Resolution Stacked Multilevel Inverter Topology for Adjustable Speed Drives," *IEEE Transactions on Industrial Electronics*, vol. 65, no. 3, pp. 2049-2056, 2018.
- [108] R. V. Nair, R. Chattopadhyay, S. Parashar, S. Bhattacharya, and K. Gopakumar, "Cascaded Active Neutral Point Clamped and Flying Capacitor Inverter Topology for Induction Motor Drives Applications," in *2018 IEEE Energy Conversion Congress and Exposition (ECCE)*, 2018, pp. 6696-6702.
- [109] R. V. N., S. A. R., S. Pramanick, K. Gopakumar, and L. G. Franquelo, "Novel Symmetric Six-Phase Induction Motor Drive Using Stacked Multilevel Inverters With a Single DC Link and Neutral Point Voltage Balancing," *IEEE Transactions on Industrial Electronics*, vol. 64, no. 4, pp. 2663-2670, 2017.
- [110] M. Jones, S. N. Vukosavic, D. Dujic, and E. Levi, "A Synchronous Current Control Scheme for Multiphase Induction Motor Drives," *IEEE Transactions on Energy Conversion*, vol. 24, no. 4, pp. 860-868, 2009.

- [111] R. Bojoi, F. Farina, A. Tenconi, F. Profumi, and E. Levi, "Dual three-phase induction motor drive with digital current control in the stationary reference frame," *Power Engineer*, vol. 20, no. 3, pp. 40-43, 2006.
- [112] A. G. Yepes, J. Malvar, A. Vidal, O. López, and J. Doval-Gandoy, "Current Harmonics Compensation Based on Multiresonant Control in Synchronous Frames for Symmetrical n -Phase Machines," *IEEE Transactions on Industrial Electronics*, vol. 62, no. 5, pp. 2708-2720, 2015.
- [113] J. Karttunen, S. Kallio, P. Peltoniemi, and P. Silventoinen, "Current Harmonic Compensation in Dual Three-Phase PMSMs Using a Disturbance Observer," *IEEE Transactions on Industrial Electronics*, vol. 63, no. 1, pp. 583-594, 2016.
- [114] Y. Hu, Z. Zhu, and K. Liu, "Current Control for Dual Three-Phase Permanent Magnet Synchronous Motors Accounting for Current Unbalance and Harmonics," *IEEE Journal of Emerging and Selected Topics in Power Electronics*, vol. 2, no. 2, pp. 272-284, 2014.
- [115] A. Negahdari, A. G. Yepes, J. Doval-Gandoy, and H. A. Toliyat, "Efficiency Enhancement of Multiphase Electric Drives at Light-Load Operation Considering Both Converter and Stator Copper Losses," *IEEE Transactions on Power Electronics*, vol. 34, no. 2, pp. 1518-1525, 2019.
- [116] D. Semenov, B. Tian, Q. An, and L. Sun, "Position estimation for sensorless FOC of five-phase PMSM in electric vehicles," in *2016 Australasian Universities Power Engineering Conference (AUPEC)*, 2016, pp. 1-5.
- [117] S. Rhaili, A. Abbou, A. Ziouh, and R. Elidrissi, "Comparative study between PI and FUZZY logic controller in vector controlled five-phase PMSG based variable-speed wind turbine," in *2018 IEEE 12th International Conference on Compatibility, Power Electronics and Power Engineering (CPE-POWERENG 2018)*, 2018, pp. 1-6.
- [118] S. Kouro, P. Cortes, R. Vargas, U. Ammann, and J. Rodriguez, "Model Predictive Control—A Simple and Powerful Method to Control Power Converters," *IEEE Transactions on Industrial Electronics*, vol. 56, no. 6, pp. 1826-1838, 2009.
- [119] F. Barrero, M. R. Arahall, R. Gregor, S. Toral, and M. J. Duran, "A Proof of Concept Study of Predictive Current Control for VSI-Driven Asymmetrical Dual Three-Phase AC Machines," *IEEE Transactions on Industrial Electronics*, vol. 56, no. 6, pp. 1937-1954, 2009.
- [120] H. Lu, J. Li, R. Qu, D. Ye, and Y. Lu, "Fault-Tolerant Predictive Control of Six-Phase PMSM Drives Based on Pulse-Width-Modulation," *IEEE Transactions on Industrial Electronics*, pp. 1-1, 2018.
- [121] D. Ye, J. Li, R. Qu, H. Lu, and Y. Lu, "Finite set model predictive MTPA control with VSD method for asymmetric six-phase PMSM," in *2017 IEEE International Electric Machines and Drives Conference (IEMDC)*, 2017, pp. 1-7.
- [122] H. Lu, J. Li, R. Qu, D. Ye, Y. Lu, and R. Zhang, "Post-fault model predictive control of asymmetrical six-phase permanent magnet machine with improved mathematical model,"

- in *2017 IEEE International Electric Machines and Drives Conference (IEMDC)*, 2017, pp. 1-7.
- [123] I. Gonzalez-Prieto, M. J. Duran, J. J. Aciego, C. Martin, and F. Barrero, "Model Predictive Control of Six-Phase Induction Motor Drives Using Virtual Voltage Vectors," *IEEE Transactions on Industrial Electronics*, vol. 65, no. 1, pp. 27-37, 2018.
- [124] Y. Luo and C. Liu, "A Simplified Model Predictive Control for a Dual Three-Phase PMSM With Reduced Harmonic Currents," *IEEE Transactions on Industrial Electronics*, vol. 65, no. 11, pp. 9079-9089, 2018.
- [125] P. Brockerhoff, W. Schön, P. Blaha, P. Václavek, and Y. Burkhardt, "Disc inverter in highly integrated 9-phase drivetrain for E-mobility," in *2015 17th European Conference on Power Electronics and Applications (EPE'15 ECCE-Europe)*, 2015, pp. 1-9.
- [126] L. Verkroost, J. V. Damme, H. Vansompel, F. D. Belie, and P. Sergeant, "Module Connection Topologies and Interleaving Strategies for Integrated Modular Motor Drives," in *2019 IEEE International Electric Machines & Drives Conference (IEMDC)*, 2019, pp. 559-564.
- [127] J. V. Damme, L. Verkroost, H. Vansompel, F. D. Belie, and P. Sergeant, "A holistic DC link architecture design method for multiphase integrated modular motor drives," in *2019 IEEE International Electric Machines & Drives Conference (IEMDC)*, 2019, pp. 1593-1598.
- [128] I. Subotic, E. Levi, M. Jones, and D. Graovac, "An integrated battery charger for EVs based on an asymmetrical six-phase machine," in *IECON 2013 - 39th Annual Conference of the IEEE Industrial Electronics Society*, 2013, pp. 7244-7249.
- [129] I. Subotic, E. Levi, and N. Bodo, "A Fast On-Board Integrated Battery Charger for EVs Using an Asymmetrical Six-Phase Machine," in *2014 IEEE Vehicle Power and Propulsion Conference (VPPC)*, 2014, pp. 1-6.
- [130] I. Subotic, N. Bodo, and E. Levi, "Single-Phase On-Board Integrated Battery Chargers for EVs Based on Multiphase Machines," *IEEE Transactions on Power Electronics*, vol. 31, no. 9, pp. 6511-6523, 2016.
- [131] A. Bindra, "Wide-Bandgap-Based Power Devices: Reshaping the power electronics landscape," *IEEE Power Electronics Magazine*, vol. 2, no. 1, pp. 42-47, 2015.
- [132] S. Hazra, S. Madhusoodhanan, G. K. Moghaddam, K. Hatua, and S. Bhattacharya, "Design Considerations and Performance Evaluation of 1200-V 100-A SiC MOSFET-Based Two-Level Voltage Source Converter," *IEEE Transactions on Industry Applications*, vol. 52, no. 5, pp. 4257-4268, 2016.
- [133] J. Liu, W. Su, X. Tai, W. Sun, L. Gu, and X. Wen, "Development of an inverter using hybrid SiC power module for EV/HEV applications," in *2016 19th International Conference on Electrical Machines and Systems (ICEMS)*, 2016, pp. 1-5.
- [134] H. Zheng, X. Wang, X. Wang, L. Ran, and B. Zhang, "Using SiC MOSFETs to improve reliability of EV inverters," in *2015 IEEE 3rd Workshop on Wide Bandgap Power Devices and Applications (WiPDA)*, 2015, pp. 359-364.

- [135] H. Wang and D. Jiang, "Design of high temperature gate driver for SiC MOSFET for EV motor drives," in *2017 IEEE Transportation Electrification Conference and Expo, Asia-Pacific (ITEC Asia-Pacific)*, 2017, pp. 1-6.
- [136] T. Shimomura, K. Numakura, D. Sato, and T. Hayashi, "High Speed dV/dt Control Technology for a SiC Power Module for EV/HEV Inverters Using a Multistage Drive Circuit," in *2018 IEEE Energy Conversion Congress and Exposition (ECCE)*, 2018, pp. 3542-3546.
- [137] Q. Wei, B. Wu, D. Xu, and N. R. Zargari, "A Natural-Sampling-Based SVM Scheme for Current Source Converter With Superior Low-Order Harmonics Performance," *IEEE Transactions on Power Electronics*, vol. 31, no. 9, pp. 6144-6154, 2016.
- [138] Q. Wei, B. Wu, D. Xu, and N. R. Zargari, "Minimization of Filter Capacitor for Medium-Voltage Current-Source Converters Based on Natural Sampling SVM," *IEEE Transactions on Power Electronics*, vol. 33, no. 1, pp. 473-481, 2018.
- [139] F. Filsecker, R. Álvarez, and S. Bernet, "Design and losses of PWM current source converters," in *2010 IEEE International Conference on Industrial Technology*, 2010, pp. 737-744.
- [140] W. Kun, Y. Xiaojie, W. Chenchen, and Z. Minglei, "An equivalent dual three-phase SVPWM realization of the modified 24-sector SVPWM strategy for asymmetrical dual stator induction machine," in *2016 IEEE Energy Conversion Congress and Exposition (ECCE)*, 2016, pp. 1-7.
- [141] E. Levi, "Advances in Converter Control and Innovative Exploitation of Additional Degrees of Freedom for Multiphase Machines," *IEEE Transactions on Industrial Electronics*, vol. 63, no. 1, pp. 433-448, 2016.
- [142] J. Prieto, F. Barrero, M. J. Durán, S. T. Marín, and M. A. Perales, "SVM Procedure for n -Phase VSI With Low Harmonic Distortion in the Overmodulation Region," *IEEE Transactions on Industrial Electronics*, vol. 61, no. 1, pp. 92-97, 2014.
- [143] G. Carrasco and C. A. Silva, "Space Vector PWM Method for Five-Phase Two-Level VSI With Minimum Harmonic Injection in the Overmodulation Region," *IEEE Transactions on Industrial Electronics*, vol. 60, no. 5, pp. 2042-2053, 2013.
- [144] S. Paul and K. Basu, "Overmodulation Techniques of Asymmetrical Six-phase Machine With Optimum Harmonic Voltage Injection," *IEEE Transactions on Industrial Electronics*, pp. 1-1, 2020.
- [145] N. A. Azeez, K. Gopakumar, J. Mathew, and C. Cecati, "A Harmonic Suppression Scheme for Open-End Winding Split-Phase IM Drive Using Capacitive Filters for the Full Speed Range," *IEEE Transactions on Industrial Electronics*, vol. 61, no. 10, pp. 5213-5221, 2014.
- [146] C. Zhou, G. Yang, and J. Su, "PWM Strategy With Minimum Harmonic Distortion for Dual Three-Phase Permanent-Magnet Synchronous Motor Drives Operating in the Overmodulation Region," *IEEE Transactions on Power Electronics*, vol. 31, no. 2, pp. 1367-1380, 2016.

- [147] Y. Geng, R. Deng, W. Dong, K. Wang, H. Liu, and X. Wu, "An Overlap-Time Compensation Method for Current-Source Space-Vector PWM Inverters," *IEEE Transactions on Power Electronics*, vol. 33, no. 4, pp. 3192-3203, 2018.
- [148] G. Su and L. Tang, "Current source inverter based traction drive for EV battery charging applications," in *2011 IEEE Vehicle Power and Propulsion Conference*, 2011, pp. 1-6.
- [149] F. Liu, B. Wu, M. Pande, and N. R. Zargari, "Zero-Speed Operation of High-Power PWM Current-Source-Inverter-Fed Induction Motor Drive," *IEEE Transactions on Power Electronics*, vol. 27, no. 6, pp. 3020-3027, 2012.
- [150] Y. Luo and C. Liu, "Model Predictive Control for a Six-Phase PMSM With High Robustness Against Weighting Factor Variation," *IEEE Transactions on Industry Applications*, vol. 55, no. 3, pp. 2781-2791, 2019.
- [151] E. Al-Nabi, B. Wu, N. R. Zargari, and V. Sood, "Input Power Factor Compensation for High-Power CSC Fed PMSM Drive Using d -Axis Stator Current Control," *IEEE Transactions on Industrial Electronics*, vol. 59, no. 2, pp. 752-761, 2012.
- [152] Z. Shen, D. Jiang, T. Zou, and R. Qu, "Dual-Segment Three-Phase PMSM With Dual Inverters for Leakage Current and Common-Mode EMI Reduction," *IEEE Transactions on Power Electronics*, vol. 34, no. 6, pp. 5606-5619, 2019.
- [153] J. Kalaiselvi and S. Srinivas, "Bearing Currents and Shaft Voltage Reduction in Dual-Inverter-Fed Open-End Winding Induction Motor With Reduced CMV PWM Methods," *IEEE Transactions on Industrial Electronics*, vol. 62, no. 1, pp. 144-152, 2015.
- [154] A. Muetze and C. R. Sullivan, "Simplified Design of Common-Mode Chokes for Reduction of Motor Ground Currents in Inverter Drives," *IEEE Transactions on Industry Applications*, vol. 47, no. 6, pp. 2570-2577, 2011.
- [155] Y. Fan, C. Li, W. Zhu, X. Zhang, L. Zhang, and M. Cheng, "Stator Winding Interturn Short-Circuit Faults Severity Detection Controlled by OW-SVPWM Without CMV of a Five-Phase FTFSCW-IPM," *IEEE Transactions on Industry Applications*, vol. 53, no. 1, pp. 194-202, 2017.
- [156] N. Zhu, D. Xu, B. Wu, N. R. Zargari, M. Kazerani, and F. Liu, "Common-Mode Voltage Reduction Methods for Current-Source Converters in Medium-Voltage Drives," *IEEE Transactions on Power Electronics*, vol. 28, no. 2, pp. 995-1006, 2013.
- [157] J. Shang, Y. W. Li, N. R. Zargari, and Z. Cheng, "PWM Strategies for Common-Mode Voltage Reduction in Current Source Drives," *IEEE Transactions on Power Electronics*, vol. 29, no. 10, pp. 5431-5445, 2014.
- [158] Y. Xu, Z. Wang, P. Liu, and J. He, "A Soft-Switching Current-Source-Inverter-Fed Motor Drive With Reduced Common-Mode Voltage," *IEEE Transactions on Industrial Electronics*, vol. 68, no. 4, pp. 3012-3021, 2021.
- [159] Z. Shen, D. Jiang, Z. Liu, D. Ye, and J. Li, "Common-Mode Voltage Elimination for Dual Two-Level Inverter-Fed Asymmetrical Six-Phase PMSM," *IEEE Transactions on Power Electronics*, vol. 35, no. 4, pp. 3828-3840, 2020.

- [160] J. Zhang, Y. Pang, K. Wang, D. Xu, and L. Pan, "Modulation Method for Nine-Switch Converter based on Equivalent Mechanism between Nine-Switch Converter and Dual Six-Switch Converters," *IEEE Transactions on Industrial Electronics*, pp. 1-1, 2020.